EFFECTIVE ADSORPTIVE REMOVAL OF HEAVY METAL IONS BY AGGREGATED MoS_2 NANOFLAKES WITH EDGE SITE EXPOSURE

CHAN KWAN SHING

MPhil

The Hong Kong Polytechnic University

2020

The Hong Kong Polytechnic University

Department of Applied Biology and Chemical Technology

Effective Adsorptive Removal of Heavy Metal Ions by Aggregated MoS_2 Nanoflakes with Edge Site Exposure

Chan Kwan Shing

A thesis submitted in partial fulfilment of the requirements for the degree of Master of Philosophy

Aug 2018

CERTIFICATE OF ORIGINALITY

I hereby declare that this thesis is my own work and that, to the best of my knowledge and belief, it reproduces no material previously published or written, nor material that has been accepted for the award of any other degree or diploma, except where due acknowledgement has been made in the text.

Chan Kwan Shing

Abstract

Recently, metal-sulfide-based adsorbents have garnered a lot of attention with regard to heavy metal recovery due to their intrinsic selectivity to soft metal ions. Molybdenum sulfide (MoS_2), a novel two-dimensional material, was identified as a suitable metal sulfide adsorbent with good acid and air stability. In this study, different MoS_2 materials were prepared by a facile hydrothermal method with different optimization approaches: the doping of metal, adjustment of precursor concentration and incorporation of mesocellular siliceous foams (MCF). The MoS_2 formation was confirmed by Raman spectroscopy and elemental analysis.

Metal screening studies revealed that the MoS_2 materials could effectively immobilize Cu^{2+}, Hg^{2+}, Ag^{+} and Pb^{2+}. Cu^{2+} was chosen for further investigation because Cu^{2+} received less interference from potential side reactions and the formation of metal molybdate. All the MoS_2 materials were investigated for Cu^{2+} adsorption performance. Based on the screening data on Cu^{2+} adsorption, MoS_2-1:4 and MoS_2-1:7 were selected for further adsorption studies, including kinetics, isotherm, effect on pH, effect on salt and regeneration and reuse of the material. A kinetic study reveals that the Cu^{2+} adsorption on MoS_2-1:4 and MoS_2-1:7 was completed in a 180-240 minute contact time frame with ~99% removal. The Elovich model is the best model to describe the Cu^{2+} adsorption kinetics of MoS_2-1:4 and MoS_2-1:7. The isotherm study demonstrates that the maximum Cu^{2+} adsorption capacities of MoS_2-1:7 and MoS_2-1:4 calculated from Sips isotherm are 201.35 and 226.20 mg/g respectively. Isotherm modelling reveals that both non-linear Dubinin-Radushkevitch and Sips isotherms can best simulate the equilibrium data of Cu^{2+}

adsorption on MoS_2-1:4, while the Sips isotherm is the best model for simulating the data of Cu^{2+} adsorption on MoS_2-1:7. In addition, the optimal pH range for the Cu^{2+} adsorption on MoS_2-1:4 and MoS_2-1:7 was between 4 and 6. The zeta potential study suggests that coulombic interaction between the positively-charged Cu^{2+} and the negatively-charged MoS_2 is one of the driving forces for the Cu^{2+} adsorption. In the desorption study, 86% of the adsorption capacity of MoS_2-1:7 remained after three adsorption/desorption cycles using 1.0 M HCl as a desorbing agent.

A combination of scanning electron microscopy with energy-dispersive X-ray spectroscopy (SEM-EDX), X-ray photoelectron spectroscopy (XPS), X-ray diffractometry (XRD), N_2-adsorption/desorption isotherm measurement and zeta potential measurement, was used to evaluate and characterize the Cu^{2+} adsorption mechanism. The SEM images reveal that MoS_2-1:4 and MoS_2-1:7 are wire-brush like and are composed of aggregated MoS_2 nanoflakes with edge site exposure. The formation of nanosheets in MoS_2-1:4 and MoS_2-1:7 are also confirmed by the XRD analysis of the MoS_2 materials. The XPS studies have discovered that the S_2^{2-} species located at the edge sites of MoS_2 nanosheets contributes significantly to the binding of Cu^{2+}.

This study shows that aggregated MoS_2 nanoflakes with edge site exposure have been successfully synthesized by a facile hydrothermal method. The MoS_2 nanoflakes have demonstrated great potential as a highly effective adsorbent for the removal of Cu^{2+} from wastewater and contaminated water. The role of S_2^{2-} species in the adsorption of Cu^{2+} on the MoS_2 nanosheets was first reported in this study. This can offer an alternative strategy to the precise engineering of MoS_2 adsorbent in the future

Acknowledgements

I offer my sincere gratitude to my supervisor Prof. Lo Chun Lap for his help on Mphil oral defense.

I offer my gratitude to my previous supervisor, Dr. Lo Wai Hung, for his patience, knowledge, and advice on my research work.

I am grateful to Dr. Lam Yan Yan, Mr. Ho Kwok Pan, Miss Wang Qian, Mr. Chung Sai Fung, and Mr. Kim Chi Fai for their suggestions and review of my work.

I would also like to thank Dr. Tsang Yuen Hong for his suggestions and help, Mr. Ho Chi Man for conducting elemental analysis, and Miss Long Hui for her assistance in the XRD and SEM studies.

Finally, I would like to acknowledge the funding support from the Hong Kong Research Grants Council (grant no. PolyU 153055/17P) and the Hong Kong Polytechnic University Central Research Grant.

Table of Contents

List of Figures

List of Tables

Chapter 1 Introduction

1.1 Background

Heavy metal contamination in water has attracted worldwide attention because it is harmful to both humans and aquatic organisms. Copper is widely used in various industries such as electroplating, mining and metal refining. An excessive intake of Cu^{2+} by the human body may cause lethargy, anorexia and liver cirrhosis.[1] The direct discharge of effluents into the environment has adverse effects on the aquatic ecosystem, especially that of aquatic plants.[2] As a result, the World Health Organization (WHO) has recommended 2 mg/L as the maximum acceptable concentration of Cu^{2+} in drinking water.[3] The effluent guidelines from the U.S Environmental Protection Agency (EPA) regulate the concentrations of copper in effluents from different industries. For example, the four-day average maximum copper concentration in effluents from the electroplating industry is set at 2.7 mg/L.[4]

Excessive copper should be removed from drinking water before consumption and from wastewater before discharging. There are several conventional treatment methods such as adsorption, ion-exchange, membrane filtration and precipitation. Adsorption is considered a simple and effective method which provides a flexible treatment design and operation.[5]

According to Hard Soft Acid Base (HSAB) theory, Cu^{2+} is classified as a borderline Lewis acid.[6] The oxygen-containing, amino and sulfur-containing groups, on the surface

of adsorbents, are able to capture Cu^{2+} in aqueous solutions. However, there is limited research on Cu^{2+} adsorption using adsorbents with sulfur-containing groups or metal sulfide, most likely due to their limited stability in the air and acid.[7-8]

Several metal-sulfide-based adsorbents such as MoS_2 nanosheet, KMS ($K_{2X}M_XSn_{3-X}S_6$) materials, tetrathiomolybdate- (MoS_4^{2-}) and polysulfide- (S_x^{2-}) intercalated layered double hydroxides (LDHs) have recently been discovered and are applied in the removal of heavy metal ions, radioactive ions and precious metal ions from aqueous solutions. The metal sulfides contain sulfur-based adsorption sites with intrinsic selectivity to soft metal ions. The intrinsic sulfur-based active sites usually have better adsorption performance than the functionalized sulfur groups.[9] The regeneration of the KMS materials, MoS_4^{2-}-LDH and S_x^{2-}-LDH is very challenging because they bind strongly to the soft ions and are not very stable in acids.[8, 10-11] Therefore, the MoS_2 nanosheet is advantageous with relatively high acidic stability and feasible regeneration under acidic conditions.[12]

MoS_2 has gained worldwide attention because the single-layered and few-layered MoS_2 displays different outstanding electronic, photonic, mechanic and thermal properties. MoS_2 nanosheets have been widely applied in electrochemical hydrogen evolution reaction (E-HER) and photocatalytic hydrogen evolution reaction (P-HER). Recently, MoS_2 nanosheets were demonstrated to be good adsorbents towards Hg^{2+} and Pb^{2+}.[12,13] The adsorption capacity of Hg^{2+} and Pb^{2+} reached as high as 2,565 and 1,479 mg/g respectively. However, the adsorption of Cu^{2+} towards MoS_2 has yet to be investigated. This therefore motivates us to investigate the potential of MoS_2 on Cu^{2+} adsorption. In this study, MoS_2 was prepared by a facile and economical hydrothermal process because hydrothermal

synthesis is capable of controlling the size, shape and edge activity of MoS_2 nanosheets to a certain degree.[14]

1.2 Objectives

The objectives of the current work are as follows:

1. To optimize the preparation methods of MoS_2, such as the pre-treatment method, dose of precursor, additives and drying method.
2. To determine the adsorption ability of MoS_2 towards Ni^{2+}, Cu^{2+}, Co^{2+}, Cd^{2+}, As (III), As(V), Pb^{2+}, Sr^{2+}, Ag^{+}, Zn^{2+} and Hg^{2+}.
3. To study the adsorption performance of meatal doped MoS_2.
4. To investigate the adsorption capacity of mesocellular siliceous foams (MCF)-MoS_2 through hydrothermal sulfidation and impregnation.
5. To investigate the effect of pH, time, initial concentration and salt on Cu^{2+} adsorption by MoS_2.
6. To elucidate the Cu^{2+} adsorption mechanisms of MoS_2 by characterization studies such as XPS, SEM-EDX and XRD.

1.3 Organization of thesis

This thesis includes seven chapters.

Chapter 1 Introduction: This chapter introduces the background and objectives of the current study.

Chapter 2 Literature Review: This chapter contains two main sections: a review on the application of metal sulfide and the hydrothermal synthesis of transition metal dichalcogenides (TMDs).

Chapter 3 Materials and Methods: This chapter describes the preparation methods and materials of various MoS_2 and the procedures for conducting the adsorption study.

Chapter 4 Results and Discussion: This chapter discusses and presents metal screening results, synthesis and characterization of different MoS_2-based adsorbents, effects of various operating parameters on the Cu^{2+} removal ability of different MoS_2-based adsorbents, and Cu^{2+} removal mechanism of MoS_2-based adsorbents.

Chapter 5 Conclusion: This chapter concludes the major experimental results and findings.

Chapter 6 Further studies: This chapter suggests additional experiments to confirm the adsorption mechanism and further studies to extend this research to other areas.

Chapter 7 References: This chapter lists the references cited in this thesis.

Chapter 2 Literature Review

2.1. Application of metal sulfide in adsorption

A number of metal sulfide-based ion-exchangers and adsorbents such as MoS_2[12], KMS[15], tetrathiomolybdate[16] (MoS_4^{2-}) and polysulfide[7] (S_x^{2-}) intercalated layered double hydroxides have been discovered and applied in the removal of heavy metal ions, radioactive ions and precious metal ions. Their adsorption performance, including their maximum absorption capacity, adsorption speed and active pH range are summarized in Table 1. KMS, MoS_2 and intercalated layered double hydroxides will be discussed in detail because their adsorption behavior and mechanism may be more relevant to the present study.

Table 1 Summary of layered metal sulfide adsorption						
Adsorbent	Q_m[a] mg/g	Concentration range in isotherm (ppm)[b]	Opt. pH or pH used	Time reaching equilibrium concertation and removal percentage[c]	I_o of kinetics	Ref.
Hg^{2+}						
$K_2MgSn_2S_6$ (KMS-2)	296.9	382.6	10	~200 min, 99 %	~885.8 ppm	15
$K_{2x}Sn_{4-x}S_{8-x}$ (x= 0.65–1; KTS-3)	372	~400	2-10	<10min, >99 %	~0.21 ppm	17
$[S_x]^{2-}$-LDH	686	10 to 2006	3	NA	NA	7
MoS_4^{2-}-LDH	500	40 - 500	1.98-3.25	30 min, >99.7 %	30 ppm	16
MoS_4^{2}-Mn-LDH	594	1 - 1800	1 - 2	60 min, 99 %	50 ppm	18
MoS_2/Fe_3O_4	425.5	0 - 300 (Ce)	5 - 9	20 min, > 90 %	200 ppm	19
$K_{2x}Mn_xSn_{3-x}S_6$ (x=0.5–0.95) (KMS-1)	377	0.02 – 350	3	<6 min, > 99 %	116 ppb	20
$H_{2x}Mn_xSn_{3-x}S_6$ [(x=0.11–0.25)] or LHMS-1 (for Layered Hydrogen Metal Sulfide-1	87	0 - 0.05 (Ce)	< 0, 0 - 9	15 min, > 99%	63.7 ppb	21
Graphene-MoS_2 hybrid aerogels	719	NA	NA	NA	NA	22
Li_XMoS_2, Li_xWS_2, $LixTS_2$, Li_xTaS_2	580	200	<0	NA	NA	23
Au/Fe_3O_4/ MoS_2 Composition Aerogels	1527	0 to 1200 (Ce)	NA	30 min, > 99 %	10 ppm	24
MoS_2 with widened interlayer spacing	2563	0-150 (Ce)	3	5 min, 16.9 ppb 24 h, 0.2 ppb	10 ppm	12
MoS_2	~254 and 305 for 20 and 35 °C	30 - 250	6 - 8	180 min, ~6 %	100 ppm	25

Table 1 (continued) Summary of layered metal sulfide adsorption						
Pb^{2+}						
$[CH_3NH_3]2_xMn_xSn_{3-x}S_6 \cdot 0.5H_2O$ (x = 0.5 – 1.1) (CMS)	1053	0- 1600 Ce	2 - 7	30 min, 90 %	400 ppm	26
$K_{2x}Sn_{4-x}S_{8-x}$ (x = 0.65 – 1; KTS-3)	391	0-400	2 - 10	< 10min, > 99 %	~0.2 ppm	17
$[S_x]^{2-}$-LDH	483	10 - 2072	3	NA	NA	7
MoS_4^{2-}- LDH	290	48 - 1040	3.4 - 5.3	30 min, > 99.7 %	30 ppm	16
MoS_4^{2-}-Mn-LDH	357	50 - 1800	1 - 2	40 min, 99 %	50 ppm	18
$K_{2x}Mn_xSn_{3-x}S_6$ (x=0.5 – 0.95) (KMS-1)	319	0.2 – 300	4	< 6 min, > 99%	61 ppb	20
Graphene-MoS2 hybrid aerogels	449	NA	NA	NA	NA	22
MoS_2	1479, 35◦C 1083 20 ◦C	30 - 2000	5	20 min, EQ	600 ppm	13
Cd^{2+}						
$[CH_3NH_3]_{2x}Mn_xSn_{3-x}S_6 \cdot 0.5H_2O$ (x = 0.5–1.1) (CMS)	515	0-1200 (Ce)	3-	90 min, 90 %	200 ppm	26
$K_{2x}Sn_{4-x}S_{8-x}$ (x =0.65–1; KTS-3)	205	0-300	2-6	<5 min, 99 %	~0.17ppm	17
$K_{2x}Mn_xSn_{3-x}S_6$ (x=0.5 – 0.95) (KMS-1)	329	145-680	3-9	< 6 min, 99 %	98 ppb	20
Ag^{+}						
$K_2MgSn_2S_6$ (KMS-2)	407.7	382.6	10	~200 min, 99 %	693.6 ppm	15
Polysulfide intercalated layered double hydroxides	383	10 - 1078.6	3	NA	NA	7
MoS_4^{2-}- LDH	452	10 - 1685	4.63 -7.43	30 min, > 99.7 %	30 ppm	16
MoS_4^{2-}-Mn-LDH	565	50 - 1800	1 - 2	< 20 min, 99 %	50 ppm	18

Table 1 (continued) Summary of layered metal sulfide adsorption						
Cu^{2+}						
$K_{2x}Mn_xSn_{3-x}S_6$ (x=0.5–0.95) KMS-1	164.7, 155.6 and 152.7 (10, 25 and 40 °C)	0-500	3-6	20 min, 90%	127	8
$[S_x]^{2-}$-LDH	127	10 - 635	3	NA	NA	7
MoS_4^{2-}- LDH	181	48.70 - 2223	53.36-5.75	30 min, > 99.7 %	30 ppm	16
Cs^+						
$K_{2x}Mg_xSn_{3-x}S_6$ (x = 0.5−1) (KMS-2)	531.7	0-800, Ce	7	NA	NA	27
$K_{2x}Sn_{4-x}S_{8-x}$ (x =0.65–1) KTS-3	280	0-600 (Ce)	4-10	5 min 95 %	1-1.2 ppm	28
$(Me_2NH_2)_{4/3}(Me_3NH)_{2/3}Sn_3S_7$ $1.25H_2O$ (FJSM-SnS)	408.91	1 - 2920	1 - 10	10 min, ~85 %, 65 ºC 30 min, ~85 %, 17 ºC	128 ppm	29
Sr^{2+}						
$K_{2x}Mg_xSn_{3-x}S_6$ (x = 0.5−1) (KMS-2)	86.89	0 - 300	7	NA	NA	27
$K_{2x}Sn_{4-x}S_{8-x}$ (x =0.65–1) KTS-3	102	0 - 350 (Ce)	4 - 10	5 min, 95 %	1-1.2 ppm	28
$K_{2x}Mn_xSn_{3-x}S_6$ (x=0.5–0.95) (KMS-1)	77	0.45-79.5	4-6	NA	NA	30
$(Me_2NH_2)_{4/3}(Me_3NH)_{2/3}Sn_3S_7$ $1.25H_2O$ (FJSM-SnS)	65.19	6 - 151	7	10 min, ~80 %, 65 ºC 30 min, ~80 %, 17 ºC	44.31 ppm	29
UO_2^{2+}						
$K_{2x}Sn_{4-x}S_{8-x}$ (x =0.65–1) KTS-3	287	0 - 160 (Ce)	4 - 8	5 min, 95 %	1-1.2 ppm	28
Sx-LDH	333	22.1 - 1478.2	3.5 - 6.2	180 min, 95 %	6.82 ppb	10
$K_{2x}Mn_xSn_{3-x}S_6$ (x = 0.5−0.95), KMS-1	382	33 - 400	2.5 - 9	10 min, ~0.3 ppb	35 ppb	31

Table 1 (continued) Summary of layered metal sulfide adsorption						
Se(IV)						
MoS_4^{2-}- LDH	85	9.59-316	6.79-8.79	NA (NO Se adsorption alone)	NA	32
Se(VI)						
MoS_4^{2-}- LDH	294	9.59-316	6.29-9.19	NA (NO Se adsorption alone)	NA	32
As(V)						
MoS_4^{2-}- LDH H	56	10.29-306	7.42-11.41	5 min, 96%	~10ppm	33
As(III)						
MoS_4^{2-}- LDH	99	7.76-341	10.58-6.73	24h, 98.9%	~10ppm	33
Cr(VI)						
MoS_4^{2-}- LDH	130	9.94-311	7.56-10.37	5 min, >96%	~10ppm	33

NA = not available,

a: Q_m (mg/g) = maximum adsorption capacity

b: Initial concentration in isotherm, equilibrium concentration marked as (Ce)

c: EQ means only adsorption equilibrium was reached.

2.1.1 KMS

The general formula of KMS materials is $K_{2X}M_XSn_{3-X}S_6$. The metal M can be Mn^{2+} for KMS-1 or Mg^{2+} for KMS-2, and the X ranges from 0.5 to 1.0. KMS materials can be prepared on a large scale by hydrothermal synthesis or solid-state reaction. As shown in Figure 1, the structure of KMS-1 and KMS-2, has CdI_2 type layered structure made of edge sharing "Sn/Mg or Mn" S_6 octahedra. The Sn^{4+} and M^{2+} are in the same crystallographic position, while S^{2-} is coordinated to three metal ions. As the negative charge of the Sn/MS_2 layer is balanced by positively charged K^+, the theoretical adsorption capacity of KMS materials can be predicted by assuming that only K^+ participates in ion-exchange. The K^+ in KMS materials can be exchanged by cationic ions such as H^+ or $CH_3NH_3^+$. Because the interlayer space of KMS materials is too large to accommodate K^+, the K^+ ions are loosely bound, highly mobile and exchangeable. A partial exchange of the Sn^{4+} by Mn^{2+} or Mg^{2+} in SnS_2 results in the derivation of KMS-1 and KMS-2. As shown in Figure 2, the structural difference between KMS-1 and KMS-2 is pattern of layer stacking.

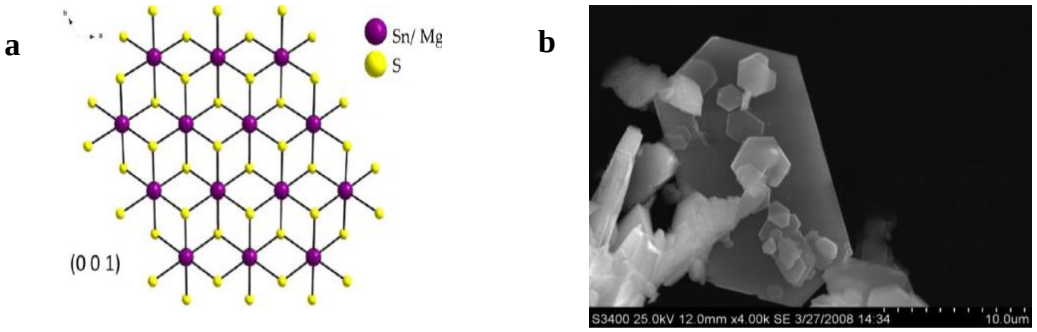

Figure 1 a) Layered structure of KMS-2, b) SEM image of hexagonal plate-like KMS-2 with size of 200 µm.[27]

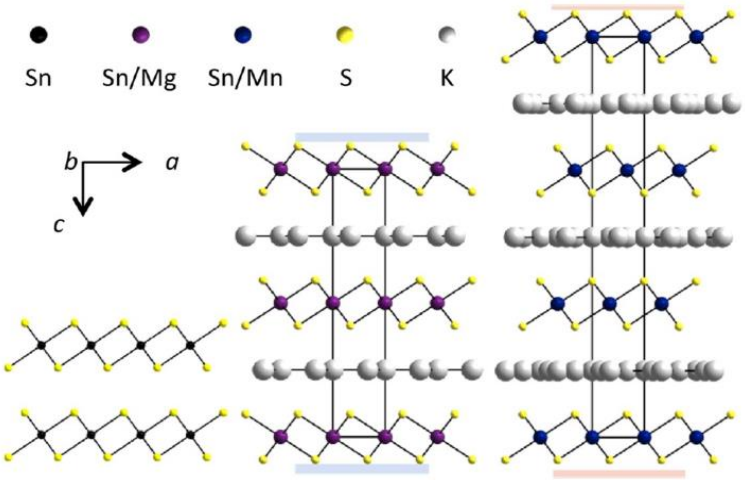

SnS_2 KMS-2 KMS-1

Figure 2 Layer stacking of SnS_2, KMS-2 and KMS-1. SnS_2: A-A stacking, KMS-2: A'-A-A' stacking, KMS-1: A-B-C-A stacking.[27]

Generally, the K^+ in the metal sulfide layer was replaced by targeted harmful cations through ion-exchange mechanism. After the capture of metal ions by ion-exchange, the interlayer distance of KMS materials would either expand or shrink. The degree of expansion or shrinkage depends on the relative size between K^+ and the targeted harmful ions. For example, the shrinkage of interlayer distance from 0.85 nm to 0.58 nm has been reported after the adsorption of Hg^{2+} on KMS-1.[20] Various KMS and KMS-based materials have been developed for the removal of radioactive ions (Cs^+,Sr^{2+}, UO_2^{2+} and Ni^{2+}), heavy metals (Hg^{2+},Cd^{2+} and Pb^{2+}) and a precious metal ion (Ag^+).The driving force of the adsorption on KMS or KMS-based materials is usually dependent on the interaction between metal ions and the sulfide group. Since the interaction is usually soft-soft interaction, the adsorbent is in general more receptive to soft cations. The adsorption capacity is furthermore affected by common hard ions, such as Na^+. K^+. Ca^{2+} and Mg^{2+} to a limited extent. KMS materials are stable in open-air environments for years but the stability in aqueous solutions is limited and depends on their pH levels. For example, the KMS-2 in a pH 3-9 aqueous solution was stable for a few days, but the material decomposed in more acidic or alkaline conditions.[27]

Isotherm studies have revealed that the Hg^{2+}, Pb^{2+} and Cd^{2+} adsorption capacity of KMS-1 reached 377, 319 and 329 mg/g, respectively. This high capacity was attributed to the strong metal-sulfide interaction after an ion-exchange with K^+. Interestingly, there was an exchange between Cd^{2+} and Mn^{2+} in the metal sulfide layer framework, leading to a complete loss of Mn^{2+} in the KMS-1 material. The KMS-1 material was not stable in strong acids. As a result, the regeneration of metal-laden KMS-1 adsorbent was difficult. Another

problem of KMS-1 was the leaching of Mn^{2+} which has led to an increase in the number of health concerns related to drinking water. KMS-2 was thus developed with safer Mg^{2+}. In addition, KMS-2 showed comparable Hg^{2+}, Pb^{2+} and Cd^{2+} adsorption capacity to that of KMS-1.[20]

The acid sulfide analogue of KMS-1 $H_{2x}Mn_xSn_{3-x}S_6$ (x= 0.11–0.25) (LHMS-1), was formed by the treatment of dilute acid of KMS-1 accompanied by a partial loss of Mn^{2+} and the loss of S as H_2S. The acid derivative of KMS-1 is able to adsorb Hg^{2+} in acidic conditions as strong as 6.0M HNO_3 and 3.6 M HCl. Atomic pair distribution function (PDF) and synchrotron radiation diffraction analysis revealed the octahedral coordination of Hg^{2+} with layered sulfide atom in LHMS-1, and the Hg-S bond length was 0.257 nm. Although LHMS-1 can be regenerated by 12 M HCl without any loss in Hg^{2+} adsorption capacity, the strong acidic regenerating condition leads to 40-60% weight loss of the adsorbent.[21] The $[CH_3NH_3]_{2x}Mn_xSn_{3-x}S_6 \cdot 0.5H_2O$ (x = 1.0–1.1) (CMS) was applied in the Pb^{2+} and Cd^{2+} adsorption, and the maximum capacity reached 515 and 1053 mg/g for Cd^{2+} and Pb^{2+} respectively.[26]

The adsorption performance of KMS-1 or KMS-2 on radioactive ions such as Cs^+, Sr^{2+}, Ni^{2+} and UO_2^{2+} was investigated in detail. KMS-1 was able to capture UO_2^{2+} over a broad pH range (2.5-9) with high adsorption capacity (~380 mg/g). Over 99.9% and 84% removal of U was achieved in seawater contaminated with 1.2-1.3 ppm U and 3.8 ppb U, respectively. The U-laden adsorbent could be regenerated by Na_2CO_3 solution, but the adsorption capacity would drop to 120~190 mg/g in six adsorption/desorption cycles.[31]

KMS-1 and KMS-2 were capable of adsorbing Cs^+, Sr^{2+} and Ni^{2+}, while the performance of KMS-2 was better than that of KMS-1. The adsorption capacity of KMS-

1 on Cs^+ was 226 mg/g, which was about half of KMS-2 (499.3 mg/g). In addition, the adsorption capacity of KMS-1 on Sr^{2+} (77 mg/g) was a little lower than that of KMS-2 (86.89 mg/g). For Ni^{2+} adsorption, the performance of KMS-2 (151.1 mg/g) was five times better than KMS-1 (29.08 mg/g). The oxidation of Mn^{2+} was the major reason for the poor adsorption capacity of KMS-1. Since Mn^{2+} in KMS-1 layer might be oxidized to Mn^{3+}, the adsorption capacity of KMS-1 dropped, due to the increase in positive charge of the sulfide layer. The KMS-2 showed higher adsorption capacity towards Ni^{2+}, due to the ion-exchange between Ni^{2+} and Mg^{2+}. The adsorption capacity of KMS-2 on Sr^{2+} was 50 % of the theoretical capacity. The expansion of interlayer space from 8.52 nm to 13.80 nm after Sr^{2+} adsorption, indicating $Sr(H_2O)_6^{2+}$ which had a large hydrated size and required more volume to be accommodated. As a result, KMS-2 might not have enough space to accommodate Sr $(H_2O)_6^{2+}$ to the theoretical level.

The adsorption of Ag^+ and Hg^{2+} in cyanide solution by KMS-2 was also reported. KMS-2 reached maximum Ag^+ and Hg^{2+} adsorption (173 and 221 mg/g respectively) within three hours. Since the adsorption capacity of KMS-2 was higher than the theoretical value, the Mg^{2+} in KMS-2 framework that participated in the adsorption Hg^{2+} could be recovered by thermal treatment of Hg^{2+}-laden adsorbent as HgS form, while the recovery of Ag^+ required the dissolution of spent KMS-2 by nitic acid. PDF studies revealed the tetrahedral coordination of Ag^+ and Hg^{2+} with S atom in the KMS-2 sulfide layers. The Ag-S and Hg-S distances were determined as 0.264 nm and 0.261 nm respectively. The strong attraction between metal ions and sulfide group on KMS-2 layers was the major reason for the adsorption of Ag^+ and Hg^{2+}.[15]

2.1.2 Transition metal dichalcogenides (TMDs)

Transition metal dichalcogenides (TMDs) include several members, such as MoS_2, $MoSe_2$, WSe_2 and WS_2, with the majority of researchers focusing on MoS_2-based materials.

The first paper related to TMDs adsorption was published in 1998[23] while the single-layered MoS_2 had not yet been discovered at that time. This paper reports the application of lithium-ion intercalated TMDs (Li_xMoS_2, Li_xWS_2, Li_xTiS_2 and Li_xTaS_2) on the removal of Cd^{2+}, Zn^{2+}, Pb^{2+} and Hg^{2+} from acidic solutions. However, Li_xTiS_2 and Li_xTaS_2 undergo hydrolysis to form S^{2-}, leading to the precipitation of metal sulfide during the adsorption process. Li_xMoS_2 showed the highest adsorption to Hg^{2+} capacity (580 mg/g) and the highest removal percentage, when compared with $Cd^{2+,}$ Zn^{2+}, Pb^{2+}. The Hg-laden adsorbent ($HgMoS_2$) could be regenerated by heating (425 ^oC) under vacuum in which the MoS_2 and Hg vapor were obtained.

After the discovery of the single-layered MoS_2, researchers began to investigate the potential of MoS_2-based materials for the adsorptive removal of dyes and metal ions. Porous MoS_2 which exhibited high adsorption capacity to rhodamine B (RhB), methylene blue (MB) and methyl orange (MO) at 420 min contact time (q =163.0, 499.0 and 125.1 mg/g, respectively), was prepared by hydrothermal synthesis. The porous MoS_2 showed better performance in MB adsorption, achieving over 99% MB removal at 200 ppm of MB. The flower-like MoS_2 was also developed and its adsorption capacity to adsorb RhB, MB and MO was examined. However, the adsorption ability of MoS_2 towards cationic dyes (RhB and MB) was better than towards anionic dye (MO) due to the negative zeta potential

on the surface of MoS_2. Alkaline solutions with pH 14 can regenerate MoS_2 materials with satisfactory results.

Hg^{2+} and Pb^{2+} are common adsorption targets of MoS_2-based materials. Generally, the optimal pH for Hg^{2+} adsorption is over pH 5, probably because the zeta potential of MoS_2-based materials will become more negative when pH increases.[19, 25]

The interlayer spacing of defect-rich MoS_2 was extended from 0.62 nm to 0.94 nm by adjusting the precursor concentration, which resulted in increasing Hg^{2+} adsorption capacity from 1114.7 mg/g to 2562.8 mg/g. It is interesting to note that the interlayer spacing of the defect-rich MoS_2 reduced from 0.94 nm to 0.62 nm after the Hg^{2+} adsorption. The adsorbent showed high affinity to Hg^{2+} when the Hg^{2+} concentration was reduced from 10 ppm to 0.2 ppb in 24h of contact time. The results of H^1 solid-state NMR spectroscopy suggested the acidic nature of MoS_2, and hence the ion exchange between H^+ in $H_X MoS_2$ and Hg^{2+} in solution phase was the major adsorption mechanism. The Hg^{2+}-laden adsorbent could be recovered with 12M HCl. An adsorption study was conducted using real wastewater from polyvinyl chloride (PVC) production. Despite the presence of ~6500 ppm Na^+ and other cations in ppm level, the adsorption process successfully reduced the Hg^{2+} concentration in the wastewater from 126 ppb to 0.055 ppb.

Au nanoparticles, Fe_2O_3 nanoparticles and graphene oxide (GO) doped -MoS_2 composite aerogels (Au/Fe_2O_3/MoS_2CA) were developed and their application on the detection and adsorption of Hg^{2+} was investigated.[24] The Hg^{2+} adsorption kinetics of Au-MoS_2CA showed that the adsorption equilibrium was reached within 30 min in 10 ppm of Hg^{2+} and the Hg^{2+} equilibrium concertation was 0.11 ppb. The isotherm study revealed the

maximum adsorption capacity of ~ 1527 mg/g was achieved using Au/Fe_2O_3/MoS_2CA. The Hg^{2+}-laden Au/Fe_2O_3/MoS_2CA could be regenerated by the reduction of Hg^{2+} to elemental Hg by disodium citrate solution, followed by a thermal treatment to obtain Au−Hg amalgam. Additionally, the Fe_2O_3/MoS_2 also showed a maximum Hg^{2+}adsorption capacity of 425.5 mg/g.[19] The Hg^{2+}-laden Fe_2O_3/MoS_2 was regenerated using 0.25 M HCl and over 85% of its adsorption capacity was maintained after 5 adsorption-desorption cycles.

MoS_2 nanosheet was successfully prepared by electrochemical exfoliation method and its ability to remove Hg^{2+} was tested.[25] The isotherm study revealed that thermal treatment of the MoS_2 nanosheet could significantly enhance the maximum adsorption capacity from 254 mg/g to ~800 mg/g. The atomic force microscopy (AFM) study visualized–the growth of the Hg^{2+} layer with increasing adsorption time, indicating the absorption of the multilayered Hg^{2+}. This multilayered Hg^{2+} adsorption was further suggested by the excellent fitting of Freundlich isotherm model to the experimental data. Moreover, the results of zeta potential measurement and XPS study revealed that the positively-charged Hg^{2+} was electrostatically adsorbed on the negatively-charged MoS_2 surface and the Hg-S and Hg-O bonds were formed.

For Pb^{2+} adsorption, the Fe_2O_3/MoS_2, Co-Fe_2O_3/MoS_2/carbon dot and Mn-Fe_2O_3/MoS_2/carbon dot composite materials could achieve very high maximum adsorption capacity of 1479, 660.67 and 588.24 mg/g respectively.[13, 34] The XPS study suggested that both the formation of Pb-S and Pb-O bonding contributed to the Pb^{2+} adsorption. The Pb-S bond formation would play a more important role than the Pb-O one in the adsorption. On the other hand, the contribution of Co-Fe_2O_3, Mn-Fe_2O_3, hydroxyl and amino groups

in Pb^{2+} adsorption was also justified. More recently, the reaction of Pb^{2+} and Pb^{4+} towards the few-layered MoS_2 nanosheet has been reported. The reaction formed $PbMoO_{4-X}S_X$.[35] Interestingly, only MoS_2 nanosheets with fewer than 5 layers were reactive towards lead ion. The oxygen source in the oxidation of MoS_2 to MoO_4^{2-} came from the reduction of hydroxyl ions. The reaction can be summarized as follows:

$$4OH^- \rightarrow 2H_2O + O_2 + 4e^-$$

$$Mo(IV) + 4NO_3^- + 2H_2O + O_2 + 4e^- \rightarrow 2MoO_4^{2-} + 4NO_2 + 4H^+$$

$$MoO_4^{2-} + Pb^{2+} + S^{2-} \rightarrow PbMoO_{4-x}S_x$$

NO_3^- is the counter ion of Pb^{2+}.

2.1.3 Intercalated Layered Double Hydroxides

Layered double hydroxides (LDHs) intercalated with tetrathiomolybdate (MoS_4^{2-}) or polysulfide (S_x^{2-}) have recently been developed as absorbents towards various kinds of cations and anions.

Polysulfide intercalated layered double hydroxides (S_x-LDH) were highly selective toward Cu^{2+}, Ag^+ and Hg^{2+}, compared with Ni^{2+}, Cd^{2+}, Zn^{2+}, Pd^{2+} and Cd^{2+}. High maximum absorption capacity to Hg^{2+} and Ag^+ was achieved at 686 and 383 mg/g, respectively. Metal ions were immobilized on S_x-LDH due to the formation of polysulfide complex.[7]

The ability of S_x-LDH to capture UO_2^{2+} and elemental Hg was also demonstrated. S_x-LDH exhibited high maximum absorption capacity to UO_2^{2+} (330 mg/g), high removal

percentage (>95%) and excellent tolerance to coexisting cations (Na^+ and Ca^{2+}).[10] At a low concentration of UO_2^{2+}, polysulfide S_4^{2-} reacted with UO_2^{2+} to form $[UO_2(S_4)_2]^{2-}$ complex in the S_x-LDH interlayer. However, if the concentration of UO_2^{2+} or co-existing anion (Cl^-) was high, UO_2S_4 salt would be formed outside the S_x-LDH while the interlayer would be intercalated by NO_3^-or Cl^-. Furthermore, the Hg vapor can be immobilized in S_x-LDH in the form of HgS through the reaction with intercalated polysulfide in the S_x-LDH material. The adsorption capacity was 500 to 1,000 mg/g.[11]

Tetrathiomolybdate (MoS_4^{2-}) intercalated layered double hydroxides (MoS_4^{2-}-LDH) were tested for the removal of cation and anions. The adsorption capacity of MoS_4^2-MgAl-LDH towards Hg^{2+} and Ag^+ reached ~500 mg/g and 450 mg/g, respectively. The adsorbent displayed higher selectivity towards Ag^+, Hg^{2+}, Cu^{2+} and Pb^{2+} than Co^{2+}, Ni^{2+}, Zn^{2+} and Cd^{2+}.[16] Three binding modes of metal ions were proposed, based on the relationship between the basal spacing and the initial metal concentration. At low metal concentration, $[M(MoS_4)_2]^{2-}$ would be formed in the interlayer. MoS_4^{2-} was the major anions in the interlayer of raw MoS_4^{2-}-LDH which have a basal spacing of 1.07 nm. After metal adsorption, the metal-laden adsorbent had a basal spacing of 0.96 or 1.0 nm contributed by $M(MoS_4)_2]^{2-}$. If the metal concentration was high, $MMoS_4$ would be formed in bulk phase while the interlayer would be intercalated by NO_3^-. High adsorption capacity for Hg^{2+}, Ag^+ and Pb^{2+} (594, 564 and 357 mg/g respectively) was also achieved by MoS_4^{2-}-MnMgAl-LDH.[18]

In addition to cations, MoS_4^{2-}-LDH could also remove anions such as $HAsO_4^{2-}$, $HAsO_3^{2-}$, $HSeO_3^-$, SeO_4^{2-} and CrO_4^{2-}. The adsorption capacity of MoS_4^{2-}—LDH on $HSeO_3^-$, SeO_4^{2-}, $HAsO_4^{2-}$, $HAsO_3^{2-}$, and CrO_4^{2-} was 85, 294, 99, 56, and 130 mg/g, respectively.[32,33]

The removal of CrO_4^{2-} was accomplished by a reduction in Cr^{3+} by MoS_4^{2-} while the adsorption of $HAsO_4^{2-}$ and that of $HAsO_3^{2-}$ were attributed to the As-S interaction.[33] The mechanism of Se oxoanions removal was a complex process.[32] The SeO_4^{2-} was adsorbed through the ion-exchange mechanism with MoS_4^{2-}.For the removal of $HSeO_3^-$, $HSeO_3^-$ was reduced by MoS_4^{2-} into elemental Se, which was accompanied by the formation of SO_4^{2-}. The presence of metal ions (Hg^{2+}, Cu^{2+} and Cd^{2+}) could enhance the adsorption capacity and adsorption rate of selenium oxoanions by the reactions of the metal ions with the interlayer MoS_4^{2-} anions.

2.2 Hydrothermal synthesis of transition metal dichalcogenides (TMDs)

2.2.1 Precursors of hydrothermal synthesis

Metal oxides such as molybdenum trioxide (MoO_3)[36], ammonium molybdate ($(NH_4)_6Mo_7O_{24}$)[37], sodium molybdate (Na_2MoO_4)[38], and sodium tungstate (Na_2WO_4)[39] and metal chlorides such as tungsten hexachloride (WCl_6)[40] and molybdenum pentachloride ($MoCl_5$)[41] were metal precursors commonly used in the hydrothermal synthesis of transition metal dichalcogenides (TMD). Thiourea (H_2NCSNH_2)[42], sodium sulfide (Na_2S)[43], carbon disulfide (CS_2)[43], thioacetamide (CH_3CSNH_2)[44], potassium thiocyanate (KSCN)[43, 45], elemental sulfur (S)[37, 46], sodium thiosulfate ($Na_2S_2O_3$)[47], L-cysteine ($C_3H_7NO_2S$)[48-49], selenium (Se)[50-51] and sodium selenosulfate (Na_2SeSO_3)[47] were applied as sulfur and selenium precursor in the literature. Some special precursors such as ammonium tetrathiotungstate ($(NH_4)_2WS_4$)[52] and ammonium tetrathiomolybdate ($(NH_4)_2MoS_4$)[53-56] could simultaneously serve as both metal and chalcogens sources.

Apart from the tungsten and molybdenum salts, the structured tungsten and molybdenum oxides could act as precursors for TMD hybrid materials and nanostructures. Direct sulfidation of porous MoO_2[57] or MoOx/PANI[58] (PANI = Polyaniline) nanowires in hydrothermal condition led to the formation of MoS_2/MoO_2 and MoS_2/PANI hybrid materials. The sulfidation of WO_3 nanorods by thiourea resulted in the formation of quasi-1-D WS_2 nanocrystals.[59]

Solvents played a critical role in hydrothermal synthesis and water was the most common solvent. Besides, a mixture of water and an organic solvent such as water/EtOH[60] and water/NMP[61], [BMIM]Cl/water[62] and [EMIM]Br/water/DMF[63] were aslo frequently used. The low solubility of metal precursors such as ammonium molybdate in organic solvents limited the use of pure organic solvents. There are a few studies that utilized ammonium tetrathiomolybdate $(NH_4)_2MoS_4$ as precursor and DMF as a solvent.[64-65] It should be noted that $(NH_4)_2MoS_4$ can be dissolved in organic solvents such as DMF and NMP. The use of water-organic solvent mixture may reduce the reaction temperature and achieve better control over size and morphology. For example, MoS_2 is not able to grow in water but is able to do so in water/NMP mixture at 180^oC on SiO_2/Si.[61] The shape of MoS_2 can be controlled by adjusting the ratio of water/DMF mixture in ionic liquid assisted-solvothermal synthesis. Hollow MoS_2 spheres can be prepared in pure water whereas MoS_2 nanospheres and nanoflakes can be prepared in 3:6 and 5:4 v/v mixture of water/DMF, respectively.[63]

The choice of precursors allows the control of the TMDs' shape. MoS_2 nanospheres and nanosheets can be prepared using L-cysteine and thiourea as sulfur sources,

respectively. Polypeptide from the polymerization of L-cysteine under synthetic condition can direct the formation of MoS_2 nanospheres.

2.2.2 pH and reaction mechanism

Ammonium molybdate ($(NH_4)_6Mo_7O_{24}$) and sodium molybdate *(*Na_2MoO_4*)* are the most common metal precursors for the hydrothermal synthesis of MoS_2 while thioacetamide (CH_3CSNH_2) and thiourea (H_2NCSNH_2) are frequently used as sulfur precursors. Therefore, the major discussion on the pH effect and reaction mechanism would focus on these common precursors. Thermal decomposition mechanism and oxidation-reduction mechanism are the two main MoS_2 formation mechanisms. The thermal decomposition mechanism includes four steps: 1) the decomposition of sulfur precursors to form H_2S; 2) the sulfidation of MoO_4^{2-} by H_2S to form MoO_XS_{4-X}; 3) the formation of MoS_3 from MoO_XS_{4-X}; and, 4) the thermal decomposition of MoS_3 to MoS_2. The mechanism is supported by the observation of the intermediates and catalytic effect of acid. The intermediate MoO_XS_{4-X} was isolated in a continuous-flow hydrothermal reactor at 250-400 ^oC.[66] At the early stage of the hydrothermal synthesis of the worm-like MoS_2, the colorless reaction mixture turned to red-brown without any formation of precipitate.[67] The color change might be due to the formation of colored MoO_XS_{4-X} intermediate, and the color depended on the sulfidation levels.

Acid is a catalyst for the formation of MoO_XS_{4-X} and MoS_3. Erickson *et al.*[68] demonstrated that acids could facilitate the sulfidation of MoO_4^{2-} to MoO_XS_{4-X}. Acids can protonate the O atoms at MoO_4^{2-}, so much so that the HS^- can easily undergo nucleophilic substitution to the protonated MoO_4^{2-}. Moreover, MoO_XS_{4-X} can be precipitated by acids

to form MoS_3.[66] The proposed oxidation-reduction mechanism consists of two major steps : 1) the decomposition of sulfur precursors to form H_2S; and, 2) the oxidation-reduction process to form MoS_2. Li et al.[43] proposed the following chemical equation for the oxidation-reduction process:

$$4Na_2MoO_4 + 9H_2S + 6HCl \rightarrow 4MoS_2 + Na_2SO_4 + 12H_2O + 6NaCl$$

Based on their discovery on the formation of SO_4^{2-} in the solution phase after the hydrothermal synthesis, Tian *et al.*[69] also reported the formation of SO_4^{2-} in the filtrate on the hydrothermal synthesis of MoS_2 nanotubes and nanorods. In summary, the H_2S formation is the first step in both mechanisms, but the respective pathways for MoS_2 formation is different.

Hydrothermal synthesis under alkaline conditions is rarely reported. MoS_2 cannot be synthesized in strongly alkaline condition. Ding *et al.*[70] noticed that the morphology of MoS_2 could be controlled by adjusting the NaOH concentration in MoS_2 synthesis. The MoS_2 particles (~500 nm), made up of nanosheets, were formed without NaOH whereas the flower-shaped MoS_2 particles (~4 μm) were formed in 1 M NaOH. When the concentration of NaOH further increased to 3 M, the size of MoS_2 particles would increase to 5–10 μm, and the MoS_2 particles became denser. A similar observation in size increase was demonstrated by using an ammonium solution as a base in synthesizing MoS_2. The catalytic effect of base in thiourea hydrolysis resulted in the size increase of MoS_2 particles.

2.2.3 Temperature

Temperatures between 180 and 220 ^oC are the typical growing conditions for MoS_2 in hydrothermal synthesis. The growing of other TMDs such as $MoSe_2$ and WS_2 requires

higher temperatures or the presence of reducing agents. Shang *et al.*[59] demonstrated that WS_2 was obtained at 265 ^oC, but the synthesis was not completed at 240 ^oC. The insufficient hydrothermal temperature at 220 ^oC resulted in the formation of WO_2 in WS_2/reduced graphene oxide (rGO) composites.[39] Hydroxylamine hydrochloride ($NH_2OH{\cdot}HCl$) and hydrazine monohydrate ($N_2H_4{\cdot}H_2O$) served as reducing agents to reduce the growth temperature of $MoSe_2$ and WS_2 to 180-220 ^oC.[60, 51, 71-72] It should be noted that reducing agents were not only used to the synthesis of $MoSe_2$ and WS_2, but they were also applied to the MoS_2 synthesis.[73]

2.2.4 Hydrothermal synthesis of TMDs with different morphologies

1-D nanotubes, 2-D nanosheets and 3-D hierarchical structure of MoS_2 can be prepared by hydrothermal synthesis. The sulfidation of 1-D precursor and the direct synthesis from simple precursor are the two ways to synthesize 1-D TMDs. MoS_2 nanorods (60–100 nm) and nanotubes (500 nm) have been prepared by the sulfidation of MoO_3 by KSCN at 180 and 220 ^oC, respectively.[69] The formation of tubes and rods structure could be attributed to the rolling and curving of MoS_2 nanosheets. Cetyltrimethylammonium bromide (CTAB), a surfactant, was capable of promoting the formation of WS_2 nanorods by selective adsorption in a particular direction.[74] The sulfidation of WO_3 nanorods with a structured precursor, thiourea, resulted in the formation of quasi 1-D WS_2 nanocrystals.[59]

TMDs prefer to grow into 2-D nanosheets because of its anisotropic property. MoS_2 nanoparticles are observed at the early stage of the synthesis of nanosheets so the formation of nanosheets is believed to account for oriented aggregation of nanoparticles.[62] The flower-like, worm-like and hollow microspheres MoS_2 are 3-D hierarchical structures

made up of 2-D nanosheets (Figure 3). Micro-sized droplets of ionic liquids can serve as a nucleation site for the growth of MoS_2 nanosheets because of the coulombic attraction between the ionic liquids and MoO_4^{2-}.[62] The hollow structure was formed after having the ionic liquids removed. The CTAB-assisted self-assembling of nanosheets can reduce the surface energy of nanosheets, leading to flower-like MoS_2 structures.[75] A three-D hierarchical structure made of MoS_2 nanosheets with a thickness of 3.9 nm has been demonstrated in polyvinylpyrrolidone(PVP)-assisted hydrothermal synthesis.[76]

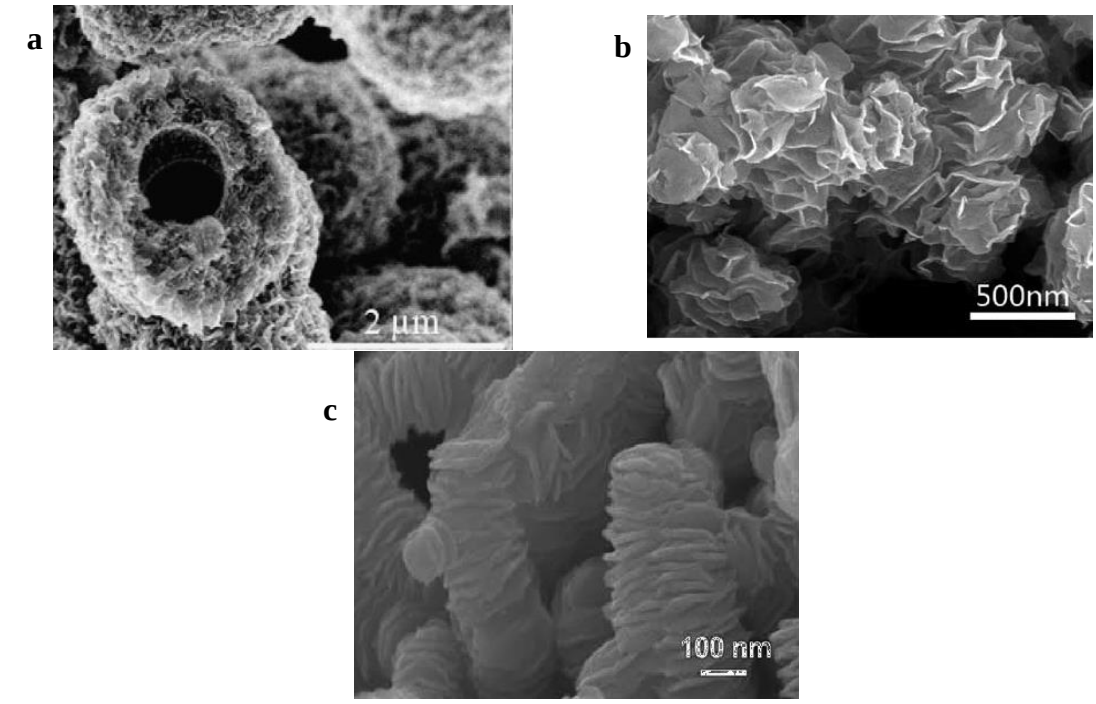

Figure 3 FETEM or SEM images of three-dimensional hierarchical MoS_2 structures: (a) hollow microspheres[62] (SEM), (b) flower-like structures[75] (SEM), (c) worm-like structures[67] (FETEM).

Chapter 3 Materials and Methods

3.1 Chemicals

Nickel(II) sulfate hexahydrate ($NiSO_4.6H_2O$), calcium chloride ($CaCl_2$), cobalt(II) chloride hexahydrate ($CoCl_2.6H_2O$), potassium chloride (KCl), manganese(II) chloride tetrahydrate ($MnCl_2.4H_2O$), sodium tungstate dihydrate ($Na_2WO_4.2H_2O$), caesium chloride (CsCl), sodium arsenate dibasic heptahydrate ($HAsNa_2O_4.7H_2O$), 6-amino-4-azahexyltrimethoxysilane (NN silane), P123 and copper (II) nitrate trihydrate ($Cu(NO_3)_2.3H_2O$), nickel(II) nitrate hexahydrate ($Ni(NO_3)_2.6H_2O$), silver nitrate ($AgNO_3$), ethylenediaminetetraacetic acid disodium salt dihydrate (Na_2EDTA), cobalt(II) nitrate hexahydrate ($Co(NO_3)_2.6H_2O$), cadmium nitrate tetrahydrate ($Cd(NO_3)_2.4H_2O$), mercury(II) nitrate monohydrate ($Hg(NO_3)_2.H_2O$), lead(II) nitrate ($Pb(NO_3)_2$), zinc nitrate hexahydrate ($Zn(NO_3)_2.6H_2O$), strontium chloride hexahydrate ($SrCl_2.6H_2O$) and sodium (meta) arsenite ($NaAsO_2$) were purchased from Sigma Aldrich. Sodium hydroxide (NaOH), thiourea (CH_4N_2S), molybdenum (IV) sulfide (MoS_2), ammonium fluoride (NH_4F), sodium molybdate dihydrate ($Na_2MoO_4.2H_2O$), ammonium molybdate ($(NH_4)_6Mo_7O_{24}$), tetraethylorthosilicate (TEOS) and L- cysteine ($HSCH_2CHNH_2COOH$) were supplied by Acros Organics. Carbon disulfide (CS_2), thioacetamide (CH_3CSNH_2) and diethylamine $(C_2H_5)_2NH$ were purchased from Dieckmann. Hydrochloric acid, nitric acid, n-hexane and dichloromethane (DCM) were purchased from Anaqua Chemical Supply.

3.2 Instrumentation and methodology

All XPS spectra were collected with a Kratos Axis Ultra DLD with Al Cu-K_α radiation. XRD measurements were performed on a Rigaku SmartLab X-ray diffractometer with Cu-K_α radiation. SEM images were obtained from a Tescan Vega3 and EDX spectra were acquired from the OXFORD instruments X-Max^n. ICP-OES data were collected from Agilent Technologies 700 Series ICP-OES. The wavelength used in ICP-OES measurement is listed in Table 2. All glassware or plasticware involved in the ICP-OES measurement and adsorption study had been immersed in 10% HNO_3 for at least 24 hours. N_2-adsroption isotherms were obtained from a Micromeritcs ASAP 2020 plus at 77 K. Prior to the measurement, samples were degassed at 120 ^oC for 10 hours under vacuum. The Brumauer-Emmett-Teller (BET) method was used to determine its surface area. The Barret–Joyner–Halenda (BJH) method was used to calculate pore volume and pore size distribution. An adsorption region of isotherm was used in both the BJH and BET calculations. The Raman spectra were acquired from a Renishaw invia micro-Raman spectrometer with a 532 nm laser, 60s exposure time and 0.1 % intensity under ambient conditions. The Raman spectrometer was calibrated by a Si peak at 520 cm^{-1}. Synthetic MoS_2 was separated by a SIGMA 2-16 centrifuge. Solid-liquid separation in adsorption studies were carried out on a Hettich Mikro 120 centrifuge. A Uniequip Unitwist 400 orbital shaker and a Unihood temperature controller were used in the adsorption study. Hydrothermal synthesis was conducted in a Hewlett Packard (HP) 5890 series II gas chromatograph oven. The accuracy of the oven temperature was confirmed by a K-type thermocouple thermometer. Elemental analysis was performed on an Elementar vario MICRO cube.

Table 2 Wavelength used in ICP-OES analysis for various elements	
Element	Wavelength (nm)
Mo	202.032
Cu	213.598
S	181.972
Ni	230.299
Sr	215.283
Pb	220.353
Co	230.786
As	188.980
Cd	214.439
Ag	328.068
Hg	253.652
Zn	213.870

3.3 Synthesis of MoS_2 and metal doped MoS2

Additives, metal precursors and chalcogens precursors in the desired quantities were dissolved in 20 ml DDI water to prepare MoS_2 materials, according to Table 3. The solution was transferred to a Teflon-lined stainless-steel autoclave and then heated to 200 ^oC in a heating rate of 5 ^oC/min in an electric oven. The product was centrifuged at 8,000 rpm for fifteen minutes and washed with DDI water thrice. Then the product was re-dispersed in 50-ml DDI water and then shaken at 250 rpm in a shaker overnight. Finally, the product was collected by centrifugation at 8,000 rpm for 15 minutes, washed with ethanol thrice and stored for freeze-drying in ethanol. Prior to the freeze-drying, the product was washed with DDI water thrice to remove the ethanol. The product was freeze-dried at -50 ^oC at 0.02 mbar overnight and then sieved with a 180 μm brass sieve. The dry product was stored at a desiccator.

To investigate the effect of drying on MoS_2, three methods, namely oven-drying, air-drying and freeze-drying, were used to dry MoS_2-1:7, and they were named oven-dried MoS_2-1:7, air-dried MoS_2-1:7 and freeze-dried MoS_2-1:7 respectively. Oven-dried and freeze-dried MoS_2 samples were separated from the solution by centrifugation at 8,000 rpm for 15 minutes, followed by oven-drying at 60 ^oC or lyophilizing at -50 ^oC and pressure of 0.02 mbar overnight. Air-dried samples were separated by suction filtration and air-dried at room temperature overnight.

Table 3 List of additives, metal precursor, chalcogens precursor and synthesis time in preparation of MoS_2 materials

Sample	Additive (mg)	Metal source (mg)	Chalcogens source (mg)	Time in hydrothermal synthesis (hours)
MoS_2-1:2[a]	/	270 mg $Na_2MoO_4.2H_2O$	165 mg CH_3CSNH_2	24
MoS_2-1:4[a]	/	270 mg $Na_2MoO_4.2H_2O$	330 mg CH_3CSNH_2	24
MoS_2-1:7[a]	/	270 mg $Na_2MoO_4.2H_2O$	533 mg CH_3CSNH_2	24
Cys-MoS_2-1:7[a]	/	270 mg $Na_2MoO_4.2H_2O$	859 mg $HSCH_2CHNH_2COOH$	24
Cys-MoS_2-1:4[a]	/	270 mg $Na_2MoO_4.2H_2O$	533 mg $HSCH_2CHNH_2COOH$	24
Ni-MoS_2	29.2 mg $NiSO_4.6H_2O$	270 mg $Na_2MoO_4.2H_2O$	533 mg CH_3CSNH_2	24
Co-MoS_2	26.4 mg $CoCl_2.6H_2O$	270 mg $Na_2MoO_4.2H_2O$	533 mg CH_3CSNH_2	24
K-Mn-MoS_2	82.0 mg KCl 54.4 mg $MnCl_2.4H_2O$	270 mg $Na_2MoO_4.2H_2O$	533 mg CH_3CSNH_2	24
W-MoS_2	181.4 mg $Na_2WO_4.2H_2O$	270 mg $Na_2MoO_4.2H_2O$	533 mg CH_3CSNH_2	24
Mn-MoS_2	54.4 mg $MnCl_2.4H_2O$	270 mg $Na_2MoO_4.2H_2O$	533 mg CH_3CSNH_2	24
K-MoS_2	82.0 mg KCl	270 mg $Na_2MoO_4.2H_2O$	533 mg CH_3CSNH_2	24
Cs-MoS_2	185 mg CsCl	270 mg $Na_2MoO_4.2H_2O$	533 mg CH_3CSNH_2	48

a: MoS_2 samples were named based on the mole ratio of metal precursors and chalcogens precursors used in the hydrothermal synthesis. For example, the MoS_2 was named MoS_2-1:2 when one mole of sodium molybdate and two moles of thioacetamide were used in the MoS_2 synthesis.

3.4 Incorporation of MoS_2 into MCF

3.4.1 Synthesis of mesocellular siliceous foam (MCF):

Four grams of P123 were dissolved in 150 ml of 1.6 M HCl solution (130 ml DDI water and 20 ml 37% HCl solution) in a 250 ml beaker. Then, 4.62 ml (4 g) of 1,3,5-trimethylbenzene (TMB) was added to the mixture before the mixture was heated at 40 ^oC for one hour under 500 rpm using magnetic stirring (size of stir bar = 20x5 mm). After that, 0.046g NH_4F and 9.36 ml TOES (8.8 g) were added to the milky mixture, and the mixture was kept at 40 ^oC for 20 hours with magnetic stirring. Next, the mixture was sealed in a 500 ml PP bottle and kept at 90 ^oC in an oil bath for 24 hours under static conditions. The white product was vacuum filtrated and washed with DDI water until no Cl^- ion was detected by 0.5 M $AgNO_3$ solution in the filtrate. The product was vacuum dried overnight and then calcined at 550 ^oC for five hours at a heating rate of 1 $^oC\ min^{-1}$ to remove P123.[77-78]

3.4.2 Synthesis of dithiocarbamates (DTC) metal complex: Cis-$Mo(IV)O_2(S_2CNEt_2)_2$ (MoDTC-2)

Cis-$Mo(IV)O_2(S_2CNEt_2)_2$ was prepared according to reference[79]. Diethylamine (2.4 ml, 23 mmol) and sodium hydroxide (0.9 g, 23 mmol) were added into DDI water (50 mL) in a 250- ml Erlenmeyer flask. After stirring for five minutes, carbon disulfide (1.4 mL, 23 mmol) was added to the mixture. A watch glass was placed over the top of the flask and the solution was stirred for 90 minutes. Sodium molybdate(VI) dihydrate (3.5 g, 14.5 mmol) was added to the mixture which was then treated dropwise with 0.7 M 100 ml HCl solution for over about 10 minutes. Vigorous stirring was required during the dropwise addition;

the yellow-brown product precipitated. The solid was isolated by vacuum filtration, washed well with water and n-hexane, and dried under suction. The crude sample was recrystallized by having it dissolved in dichloromethane (DCM), filtered, and n-hexane was added to the clear filtrate to precipitate MoDTC-2.

3.4.3 Synthesis of MoS_2-DTC-MCF

Two hundred milligrams of MCF was added into 5 ml DCM solution of Cis-$Mo(IV)O_2(S_2CNEt_2)_2$ (MoDTC-2) in a 50 ml beaker under magnetic stirring to allow the evaporation of DCM. The MoS_2-DTC-MCF samples prepared from 60 mg and 240 mg MoDTC-2 were named MoS_2-DTC-MCF-0.06 and MoS_2-DTC-MCF-0.24, respectively. Then, MoDTC-2@MCF was dispersed in 20 ml DDI water containing 300 mg thioacetamide. The mixture was transferred to a Teflon-lined stainless-steel autoclave and then heated in an electric oven at 200 ° C for 24 hours at a heating rate of 5 ^oC/min. The product-was collected at the bottom, and the supernatant was discarded. The black product was washed with 50% ethanol thrice and 95% ethanol once using centrifugation at 8,000 rpm for 10 min. Products were freeze-dried overnight and then sieved with a 180 μm brass sieve.

3.4.4 Synthesis of MoS_2-NN-MCF

Five hundred milligrams of sieved MCF was dispersed into 40 ml toluene in a 2-neck round bottom flask. The synthesis system was kept in nitrogen atmosphere with magnetic stirring. 1 ml 6-amino-4-azahexyltrimethoxysilane (NN silane) was added to the MCF solution using a syringe, and the product was named NN-MCF. The mixture was refluxed in nitrogen atmosphere with magnetic stirring for six hours. The modified MCF

was recovered by suction filtration and washed once with hexane, ethanol and then water. The modified MCF was dried at room temperature under suction overnight and sifted through a 180 μm sieve.

The NN-MCF was dispersed in 50 ml ammonium molybdate solution (containing 1.34 g ammonium molybdate) for 24 hours. MoO_3-NN-MCF was separated from the Mo solution by centrifugation, then dried at 60 ^{O}C overnight before being sifted through a 180 μm sieve. MoO_3-NN-MCF (0.5 g) and 20 ml DDI water containing 300 mg thioacetamide were transferred to a Teflon-lined stainless-steel autoclave and heated in an electric oven at 200 ° C for 24 hours at a heating rate of 5 ^{o}C/min. The product was collected at the bottom, and the supernatant was discarded. The black product was washed with 50% ethanol thrice and ethanol once by centrifugation at 8,000 rpm for 10 minutes. The product was dried at 60 ^{O}C overnight and stored at a desiccator.

3.5 Adsorption study

The adsorption capacity (q) was calculated using the following equation:

$$q = \frac{(C_0 - C_s)D_f}{d}$$

q = adsorption capacity (mg/g), C_0 = concentration of the metal ions in the control, C_s = concentration of the metal ions in the supernatant, D_f = dilution factor, d = dose of adsorbent (g/L)

3.5.1 Screening

Five milligrams of adsorbent were added into 10 ml of 1 or 2 mM metal solutions. The metal solution was prepared by dissolving copper (II) nitrate trihydrate ($Cu(NO_3)_2.3H_2O$), nickel(II) nitrate hexahydrate ($Ni(NO_3)_2.6\ H_2O$), silver nitrate ($AgNO_3$), cobalt(II) nitrate hexahydrate ($Co(NO_3)_2.\ 6H_2O$), cadmium nitrate tetrahydrate ($Cd(NO_3)_2.\ 4H_2O$), mercury(II) nitrate monohydrate ($Hg(NO_3)_2.\ H_2O$), lead(II) nitrate ($Pb(NO_3)_2$), zinc nitrate hexahydrate ($Zn(NO_3)_2.\ 6H_2O$), strontium chloride hexahydrate ($SrCl_2.6H_2O$), sodium arsenate dibasic heptahydrate ($HAsNa_2O_4.\ 7H_2O$) or sodium (meta) arsenite ($NaAsO_2$) in DDI water. The pH value was adjusted by adding NaOH or HNO_3 to the desired value. The suspension was shaken at 250 rpm in an orbital shaker at 25ºC. After 24 hours the suspension was centrifuged at 15000 rpm for two minutes to remove adsorbent. The supernatant was diluted with 1% HNO_3 to a suitable concentration for ICP-OES analysis.

3.5.2 Effect of pH

Five milligrams of adsorbent were added into 10 ml of 1 mM Cu^{2+} solution. The pH value was adjusted by adding NaOH or HNO_3 to the desired value. The suspension was shaken at 250 rpm in an orbital shaker at 25ºC. After 24 hours the suspension was

centrifuged at 15000 rpm for two minutes to remove adsorbent. The supernatant was diluted with 1% HNO_3 to a suitable concentration for ICP-OES analysis.

3.5.3 Effect of NaCl

Five milligrams of adsorbent were added into 10 ml of 2 mM Cu^{2+} solution with 0, 10, 100 and 500 mM NaCl. The pH was adjusted by adding NaOH or HNO_3 to the desired value. The suspension was shaken at 250 rpm in an orbital shaker at 25°C. After 24 hours the suspension was centrifuged at 15000 rpm for two minutes to remove adsorbent. The supernatant was diluted with 1% HNO_3 to suitable concentration for ICP-OES analysis.

3.5.4 Isotherm

Five milligrams of adsorbent were added into 10 ml of 0.4, 0.8, 1.2, 2.0, 3.0 and 4.0 mM Cu^{2+} solution. The pH was adjusted by adding NaOH or HNO_3 to pH 5.0. The suspension was shaken at 250 rpm in an orbital shaker at 25°C. After 24 hours the suspension was centrifuged at 15000 rpm for two minutes to remove adsorbent. The supernatant was diluted with 1% HNO_3 to a suitable concentration for ICP-OES analysis.

3.5.5 Kinetics

Twenty-five milligrams of adsorbent were added into 50 ml of 1 mM Cu^{2+} solution. The pH was adjusted by adding NaOH or HNO_3 to the desired value. The suspension was shaken at 250 rpm in an orbital shaker at 25°C. The suspension was centrifuged at 15000 rpm for two minutes to remove adsorbent. The supernatant was diluted with 1% HNO_3 to suitable concentration for ICP-OES analysis.

3.5.6 Regeneration

For screening of desorption agents, 0.005 g of Cu-laden MoS_2-1:7 was added into 1 ml of desorption agents. 0.1 M HCl, 1.0 M HCl, 2.0 M HCl, 4.0 M HCl, 0.05 M EDTA in 1.0 M HCl, 0.05 M EDTA in 0.1 M HCl, 0.1 M thiourea in 0.1 M HCl, 1 M NaCl, 1 M Cysteine, 0.1 M EDTA, 1 M $CaCl_2$ and DDI water were desorption agents. The suspension was shaken at 250 rpm in an orbital shaker at 25°C. After 24 hours the regenerated MoS_2-1:7 was separated by centrifugation at 15,000 rpm for two minutes. The supernatant was diluted with 1% HNO_3 to a suitable concentration for ICP-OES analysis.

For the adsorption-desorption cycle study of MoS_2-1:7, the adsorption was investigated with 10 ml of 1 mM Cu^{2+} solution at pH 5.0. The pH was adjusted by adding NaOH or HNO_3 to the desired value. The suspension was shaken at 250 rpm in an orbital shaker at 25°C.After 24 hours the suspension was centrifuged at 15000 rpm for two minutes to remove adsorbent. The desorption procedure followed the previous desorption method using 1.0 M HCl as a desorption agent. The adsorption-desorption study was conducted with the same amount of MoS_2-1:7. As a result, oxidation or weight loss of MoS_2 could occur, resulting in a change of the adsorption capacity.

3.6 Kinetic modeling

The kinetic data were simulated with four different kinetic models as follows:[80]

3.6.1 Pseudo-first-order kinetics:

$$\text{Linear form: } ln(q_e - q_t) = lnq_e - kt$$

$$\text{Non-linear form: } q_t = q_e(1 - exp(-kt))$$

q_t = adsorption capacity (mg/g) at t (min), t = contact time (min),

q_e = equilibrium adsorption capacity (mg/g), k = pseudo-first-order rate constants (min^{-1})

3.6.2 Pseudo-second-order kinetics

$$\text{Linear form: } t/q_t = \frac{1}{k(q_e{}^2)} + \frac{1}{q_e}t$$

$$\text{Non-linear form: } 1/q_t = \frac{1}{k(q_e{}^2)t} + \frac{1}{q_e}$$

q_t =adsorption capacity (mg/g) at t (min), t = contact time (min),

q_e = equilibrium adsorption capacity (mg/g),

k = pseudo-second-order rate constants (g/mg-min)

3.6.3 Elovich kinetics

$$\text{Linear form: } q_t = \beta ln\alpha\beta + \beta lnt$$

$$\text{Non-linear form: } q_t = \frac{ln((1+\alpha\beta t))}{\beta}$$

q_t =adsorption capacity (mg/g) at t (min), t = contact time (min),

α = desorption constant (g/mg-min^2), β = initial adsorption rate (mg/g-min)

3.6.4 Intra-particle diffusion kinetics

$$\text{Non-linear form: } q_t = k(t^{0.5})$$

q_t = adsorption capacity (mg/g) at t (min), t = contact time (min),

k = intraparticle diffusion rate constant mg/g-√min

3.7 Isotherm modeling

Adsorption characteristics may be found by using isotherm modeling. Five different isotherm models are listed as follows[81-82]:

3.7.1 Langmuir isotherm

$$\text{Linear form: } \frac{C_e}{q_e} = \frac{1}{bq_m} + \frac{C_e}{q_m}$$

$$\text{Non-linear form: } q_e = q_m bC_e/(1 + bC_e)$$

q_e= equilibrium adsorption capacity (mg/g), q_m = maximum adsorption capacity (mg/g),

C_e = equilibrium concentration of metal ions (ppm),

b = Langmuir isotherm constant (L/mg)

3.7.2 Freundlich isotherm

$$\text{Linear form: } lnq_e = lnK_f + \frac{1}{n} lnC_e$$

$$\text{Non-linear form: } q_e = K_f(C_e^{\frac{1}{n}})$$

q_e= equilibrium adsorption capacity (mg/g),

C_e = equilibrium concentration of metal ions (ppm),

n = Freundlich isotherm constant

K_f = Freundlich isotherm constant (mg/g)

3.7.3 Temkin isotherm

$$\text{Linear form: } q_e = \frac{RT}{b} lnA + \frac{RT}{b} lnC_e$$

$$\text{Non-linear form: } q_e = \left(\frac{RT}{b}\right) ln(AC_e)$$

q_e= equilibrium adsorption capacity (mg/g),

C_e = equilibrium concentration of metal ions (ppm),

T = temperature (K)

R = ideal gas constant (J/mol-K)

b = Temkin constant (J/mol)

A = Temkin constant

3.7.4 Dubinin-Radushkevich (DR) isotherm

$$\text{Linear form: } ln(q_e) = lnq_m - k\left[RTln\left(1 + \frac{1}{C_e}\right)\right]^2$$

$$\text{Non-linear form: } q_e = q_m exp\left\{-k\left[RTln\left(1 + \frac{1}{C_e}\right)\right]^2\right\}$$

q_e = equilibrium adsorption capacity (mg/g),

C_e = equilibrium concentration of metal ions (ppm),

T = temperature (K)

R = ideal gas constant (J/mol-K)

q_m = maximum adsorption capacity (mg/g)

k = Dubinin-Radushkevich isotherm constant (mol^2/kJ^2)

3.7.5 Sips isotherm

Non-linear form: $q_e = \frac{q_m b C_e^m}{1+b*C_e^m}$

q_e= equilibrium adsorption capacity (mg/g),

C_e = equilibrium concentration of metal ions (ppm),

q_m = maximum adsorption capacity (mg/g),

m = Sips isotherm constant

b = Sips isotherm constant (L/mg)

Chapter 4 Results and Discussion

4.1 Metal screening of MoS_2

Table 4 compares the capacities of various MoS_2 materials for the adsorption of Ni^{2+}, Cu^{2+}, Co^{2+}, Cd^{2+}, AsO_2^-, $HAsO_4^{2-}$, Pb^{2+}, Sr^{2+}, Ag^+, Zn^{2+} and Hg^{2+}. MoS_2-1:7 showed better performance than the metal-doped MoS_2 in removing most metal ions tested, except Pb^{2+}. Metal screening results showed that MoS_2-1:7 effectively captured Cu^{2+}, Pb^{2+}, Ag^+ and Hg^{2+} with high adsorption capacities of 128.8, 200.6, 224.16 and 386.13 mg/g, respectively. The commercially available bulk-MoS_2 (purchased from Acros Organics) had negligible adsorption capacity towards Cu^{2+}, Pb^{2+}, Ag^+ and Hg^{2+}. The reason for this poor adsorption capacity will be discussed in Section 4.7. It should be noted that common unit of adsorption is expressed as milligram of metal ions per grams absorbent. This unit will be affected by the molar mass of metal ions. For metal ions with high molar mass such as Pb^{2+} (207.2 g/mol) and Hg^{2+} (200.59 g/mol), the adsorption capacity will be higher these ions with low molar mass such as copper (63.5 g/mol). Besides the adsorption capacity, another parameter for adsorbent is the removal efficiency. The high percentage in the removal by the adsorption of Cu^{2+}, Ag^+ and Hg^{2+} indicates the strong affinity between MoS_2-1:7 and the metal ions. When Co-MoS_2 and Ni-MoS_2 were added into the Pb^{2+} solution, a white precipitate was observed. In addition, after suspending Ni-MoS_2 in DDI water for 24 hours to remove soluble impurities, the adsorption performance of the Pb^{2+} declined by nearly 50%. The adsorption capacity of Pb^{2+} may be overestimated because of possible precipitation of Pb^{2+} as $PbSO_4$ and $PbMoO_4$ (Table 5). Recently, a reaction between exfoliated MoS_2 and Pb^{2+} and Pb^{4+} to form $PbMoO_{4-x}S_x$ was reported.[35] Since

$PbMoO_{4-x}S_x$ is insoluble in water, this reaction was used for capturing Pb^{2+}. However, as the reaction would consume MoS_2 adsorbent, regeneration could not be achieved. The interaction between Ag^+ and MoS_2 was also reported in which Ag particles were formed on a MoS_2-based material.[83]

MoS_2-1:7 effectively captured Cu^{2+}, Pb^{2+}, Ag^+ and Hg^{2+} with high adsorption capacity. However, the product of MoS_2 (oxidation generates MoO_4^{2-} and SO_4^{2-})[84] and the formation of sulfate and molybdate salts might lead to an overestimation of the adsorption capacity. The low solubility of sulfate and molybdate salts might lead to an overestimation of adsorption capacity and adsorption affinity of MoS_2 based adsorbents. Table 5 lists the solubility of different sulfate and molybdate salts. In general, the solubility of sulfate salts is higher than that of molybdate salts, so molybdate salts would more likely be formed than sulfate salts. Since the solubility of $PbMoO_4$ is extremely low, the Pb^{2+} adsorption capacity might be significantly overestimated. The solubilities of Ag_2MoO_4 and $CuMoO_4$ correspond to 107.9 ppm Cu^{2+} and 221.65 ppm Ag^+ in solutions respectively. The solubility has little effect on Cu^{2+} and Ag^+ adsorption data because these concentrations of Cu^{2+} and Ag^+ are higher than the concentrations usually used in adsorption studies. Due to the lack of information on the solubility of sulfate and molybdate salts of mercury, extremely low solubility of lead sulfate and molybdate, uncertainty of interaction between Ag^+ and MoS_2 and availability of Hg^{2+} and Pb^{2+} adsorption studies, Cu^{2+} adsorption was chosen for further investigations.

Table 4 Metal adsorption screening of various MoS_2

	Adsorption capacity (mg/g) (% removal)										
Adsorbent	Ni^{2+}	Cu^{2+}	Co^{2+}	Cd^{2+}	AsO_2^- As(III)	$HAsO_4^{2-}$ As(V)	Pb^{2+}	Sr^{2+}	Ag^+	Zn^{2+}	Hg^{2+}
MoS_2-1:7	13.8 ± 0.8 (11.1%)	128.8 ± 0.0 (89.6%)	14.7 ± 0.1 (11.75%)	26.3 ± 0.1 (11%)	2.1 ± 1.5 (1.9%)	2.1 ± 0.8 (0.9%)	200.6 ± 13.2 (47.3%)	16.8 ± 1.1* (9.63%)	224.2 ± 0.4 (>99%)	13.2 ± 0.2 (9.4%)	386.1 ± 0.2 (96.3%)
Ni-MoS_2	ND	49.7 ± 2.00 (34.6%)	12.8 ± 1.5 (10.2%)	17.5 ± 3.2 (7.6%)	ND	4.14 ± 0.78 (1.35%)	394.9 ± 0.1 (93.2%) 209.5 ± 2.9 (49.9%)*	NA	NA	NA	NA
Co-MoS_2	9.4 ± 3.0 (7.6%)	67.5 ± 3.6 (46.9%)	4.4 ± 1.2 (3.5%)	16.4 ± 0.3 (7.1%)	ND	NA	382.6 ± 6.8 (90.3%)	NA	NA	NA	NA
Bulk-MoS_2	NA	4.2 ± 2.4 (3.0%)	NA	NA	NA	NA	27.1 ±1.5 (8.8%)	NA	26.9 ± 0.9 (11.9%)	NA	59.5 ± 10.8 (14.8%)

NA: Not available
ND: Not detected adsorption
* Adsorbent was suspended in water for 24 hours before adsorbed with Pb^{2+}.
[Initial metal concentration 1 mM, dose 0.5 g/L, pH 5.0 except Ag^+ (no pH adjustment), 250 rpm, 298 K, 24 hours.]

Table 5 Solubility (g/100 g water) of sulfate and molybdate salts

		Cations			
Anions		Ag^+	Hg^{2+}	Pb^{2+}	Cu^{2+}
	SO_4^{2-}	Ag_2SO_4 0.83[a]	Decompose into insoluble products[b]	$PbSO_4$ 0.0044[a]	$CuSO_4$ 18.0[a]
	MoO_4^{2-}	Ag_2MoO_4 0.0386[b]	/	$PbMoO_4$ 0.000012[b]	$CuMoO_4$ 0.038[b]

a, Solubility was taken from reference[85]
b, Solubility was taken from reference[86]

4.2 MoS_2 Synthesis

4.2.1 MoS_2 synthesis conditions

The Cu^{2+} adsorption results of MoS_2 with different pretreatment methods, precursors and precursor ratios are summarized in Table 6. Thioacetamide and cysteine were used as the sulfur sources in the hydrothermal synthesis of MoS_2 and Cys-MoS_2, while sodium molybdate was applied as the metal source. The Cu^{2+} adsorption capacities of MoS_2 prepared from cysteine (Cys-MoS_2-1:4 and Cys-MoS_2-1:7) were significantly lower than those of MoS_2 prepared from thioacetamide (MoS_2-1:4 and MoS_2-1:7). The use of different sulfur precursor on MoS_2 synthesis are mainly based on trial and error. To the best of my knowledge, there are few or even no research related to the use of different sulfur precursor on MoS_2 adsorption. It is believed that the use of different sulfur precursor on MoS_2 might reduce the activity of Cu^{2+} adsorption sites or induce morphologic changes to MoS_2, leading to diminished Cu^{2+} adsorption sites. As a result, the MoS_2 prepared from thioacetamide was applied in further adsorption studies.

Different mole ratios of sodium molybdate and thioacetamide were used for MoS_2 synthesis since the mole ratios might affect the structure or chemical nature of MoS_2. The MoS_2 was named 1:2 when one mole of sodium molybdate and two moles of thioacetamide were used in the hydrothermal synthesis. MoS_2-1:2 had a very low Cu^{2+} adsorption capacity probably due to the low concentration of S_2^{2-} that might serve as an adsorption site for Cu^{2+}. The detailed adsorption mechanism is further discussed in Section 4.7. As both MoS_2-1:4 and MoS_2-1:7 performed better in Cu^{2+} adsorption than MoS_2-1:2, MoS_2-1:4 and MoS_2-1:7 were thus used for further adsorption studies.

Table 6 Cu^{2+}adsorption capacities of vaious MoS_2 at different synthetic and pretreatment conditions		
Adsorbent	Adsorption capacity of Cu^{2+}(mg/g)	Removal %
Bulk-MoS_2	8.04 ± 3.41	3.0%
MoS_2-1:2	13.8 ± 1.26	5.5%
MoS_2-1:4	184.25 ± 0.58	67.47%
MoS_2-1:7	161.14 ± 7.00	59.63%
Cys-MoS_2-1:4	135.6 ± 2.0	50.2%
Cys-MoS_2-1:7	115.5 ± 1.8	42.8%
MoS_2-1:4 treatment at pH 1.5	186.37 ± 2.76	68.25%
MoS_2-1:4 treatment at pH 11	189.01 ± 7.43	69.21%
[Initial Cu^{2+} concentration 2 mM, dose 0.5 g/L, pH 5.0, 250 rpm, 298 K, 24 hours.]		

The effect of acid or base pretreatment of MoS_2 on Cu^{2+} adsorption was negligible (Table 6), indicating that the adsorption sites on MoS_2 were chemically stable to acidic and alkaline conditions.

Table 7 Effect of drying methods on Cu^{2+} adsorption and leaching of Mo and S in supernatant					
Adsorbent	Adsorption capacity of Cu^{2+}(mg/g)	Removal	Mo concentration in supernatant (ppm)	S concentration in supernatant (ppm)	Particle size
Freeze-dried MoS_2-1:7	127.15 ± 2.44	94%	13.90 ± 0.75	13.50 ± 0.74	less than 180 µm
Air-dried MoS_2-1:7	131.56 ± 4.29	97%	20.43 ± 2.4	17.62 ± 1.91	2-10 mm
Oven-dried MoS_2-1:7	126.60 ± 0.40	93%	21.5 ± 0.64	20.15 ± 0.59	2 - 3 cm
[Initial Cu^{2+} concentration 1 mM, dose 0.5 g/L, pH 5.0, 250 rpm, 298 K, 24 hours.]					

Three drying methods, oven dry, air dry and freeze dry, were furthermore used to prepare MoS_2-1:7. The drying methods significantly affected the size of MoS_2 nanosheets that could be observed by the naked eye. The oven-dried MoS_2-1:7 was a big stone-like object with a size of 2 - 3 cm, while the air-dried MoS_2 sample contained small particles with a size of 2-10 mm. Since the oven-dried MoS_2-1:7 and air-dried MoS_2-1:7 were too large for adsorption, the two samples were milled by mortar and pestle, and sifted using a 180 μm brass sieve. It was surprising that the freeze-dried MoS_2 sample was fine powder with a diameter smaller than 180 μm.

The effect of drying methods on Cu^{2+} adsorption and leaching of Mo and S in the supernatant is listed in Table 7. Generally, the drying methods had little influence on the Cu^{2+} adsorption capacity. However, different drying methods might affect the oxidation rate of MoS_2-1:7 as indicated by the leaching of Mo and S in aqueous solutions. The amount of Mo and S released by freeze-dried MoS_2-1:7 was about 33% lower than those by oven-dried MoS_2-1:7- and air-dried MoS_2-1:7. The freeze-drying process allowed the sublimation of ice in the frozen samples under high vacuum, which inhibited the oxidation of MoS_2 samples. In conclusion, freeze-drying was found to be the most suitable method of drying MoS_2 because of the minimum oxidation effect and the direct use of the MoS_2 for adsorption without further grinding.

4.2.2 Metal doping of MoS_2

Table 8 summarizes the Cu^{2+} adsorption capacities of different metal-doped MoS_2. The Cu^{2+} adsorption capacities of K-Mn-MoS_2,W-MoS_2, Mn-MoS_2, K-MoS_2 and Cs-MoS_2 ranged from 171.6 mg/g to 177.85 mg/g. Compared with MoS_2-1:4, the metal doping of K-Mn, K, Mn, W and Cs showed no significant improvement on Cu^{2+} adsorption. The metal doping of Ni and Co even reduced the Cu^{2+} adsorption capacity of MoS_2-1:4 from 135.57 to 49.68 and 67.46 mg/g, respectively. It is believed that the doping of Ni and Co on MoS_2 might reduce the activity of Cu^{2+} adsorption sites or induce morphologic changes to MoS_2, leading to diminished Cu^{2+} adsorption sites.

The doping of metal ions on MoS_2 is believed to enhance the adsorption capacity of heavy metal ions by increasing the layer spacing, reducing the number of layers, increasing the amount and activity of active sites. However, the doping of metal ions on MoS_2 synthesis are mainly based on trial and error. Most of the literature related to doping of metal ions focus on hydrogen evolution reaction. To the best of my knowledge, there are few or even no research related to doping of metal ions on MoS_2 adsorption. The Co^{2+} doped MoS_2/Al_2O_3 showed enhanced adsorption to elemental Hg vapor, but the role of Co^{2+} on the adsorption was poorly understood.[87] Besides, the incorporation of Ni^{2+} into MoS_2 could control the growth of MoS_2 nanosheets by inhibiting the growth of MoS_2 at basal planes.[88] An increase in layer spacing from 0.62 nm to 0.97 nm was observed in W-doped MoS_2 for the application related to electrochemical hydrogen evolution reaction.[41]

Table 8 Cu^{2+} adsorption capacities of metal doped MoS_2

Adsorbent	Adsorption capacity of Cu^{2+}(mg/g) (initial Cu^{2+} concentration = 1 mM)	% removal	Adsorption capacity of Cu^{2+}(mg/g) (initial Cu^{2+} concentration = 2 mM)	% removal
Ni-MoS_2	49.68 ± 2.00	34.56%	NA	NA
Co-MoS_2	67.46 ± 3.6 0	46.9%	NA	NA
MoS_2-1:4	135.57 ± 0.56	99.5%	180.0 ± 15.5	69.96%
K-Mn-MoS_2	NA	NA	171.6 ± 1.70	65.31%
W-MoS_2	NA	NA	177.85 ± 1.36	69.13%
Mn-MoS_2	NA	NA	177.38 ± 2.67	68.94%
K-MoS_2	NA	NA	176.39 ± 20.44	68.56%
Cs-MoS_2	NA	NA	172.97 ± 14.72	67.23%

NA: not available
[Dose 0.5 g/L, pH 5, 250 rpm, 298 K, 24 hours.]

4.2.3 Incorporation of MoS_2 into MCF

Mesocellular siliceous foam [78] (MCF) characterized by high hydrothermal stability, high surface area and large pore volume, was believed to be a suitable host material for MoS_2. MCF was capable of withstanding 600 ^oC 100% steam for 12 hours.[77] The incorporation of MoS_2 into MCF might increase the adsorption capacity and adsorption speed by increasing the surface area.

Two methods, (1) hydrothermal sulfidation and (2) impregnation, were applied to incorporate MoS_2 into MCF, and the obtained samples were named MoS_2-NN-MCF and DTC-MoS_2-MCF respectively. In the first method, amino-MCF was pre-adsorbed with $NH_4Mo_2O_7$ and before it was made to undergo hydrothermal sulfidation with thioacetamide as the sulfidation agent. In the impregnation method, MCF was impregnated with cis-$Mo(IV)O_2(S_2CNEt_2)_2$ in dichloromethane, followed by hydrothermal treatment with thioacetamide solution. However, microscope images (Figure 4) reveal that the MoS_2 and MCF were evenly distributed in MoS_2-NN-MCF, indicating a homogeneous mixture of MoS_2 and MCF. The hydrothermal sulfidation method had thus successfully incorporated MoS_2 into MCF. Meanwhile, the impregnation method failed to incorporate MoS_2 into MCF since MoS_2-DTC-MSF-0.06 and MoS_2-DTC-MCF-0.24 were heterogeneous mixtures of MoS_2 and MCF, as shown in Figure 4. The sulfur contents of MoS_2-NN-MCF, DTC-MoS_2-MCF-0.06 and DTC-MoS_2-MCF-0.24 were determined by elemental analysis (Section 4.3.5). The S contents of MoS_2-NN-MCF, DTC-MoS_2-MCF-0.06 and DTC-MoS_2-MCF-0.24 were 18.30 ± 0.21, 3.80 ± 0.04 and 9.62 ± 0.09 wt %, respectively,

corresponding to the MoS_2 contents of 45.75, 9.50 and 24.05 wt %. From the results of the adsorption study shown in Table 9, the Cu^{2+} adsorption capacities of MoS_2-NN-MCF, DTC-MoS_2-MCF-0.06 and DTC-MoS_2-MCF-0.24 were lower than that of MoS2-1:4, which could be explained by the lower MoS_2 content in MoS_2-NN-MCF, DTC-MoS_2-MCF-0.06 and DTC-MoS_2-MCF-0.24.

MCM-41, a mesoporous material, was used as the host material for MoS_2 synthesis in a preliminary study. However, MCM-41 was not able to withstand the hydrothermal condition due to its thin silica wall. It was found that the drastic condition of hydrothermal synthesis at 200 ^oC with water as solvent completely damaged the structure of MCM-41. Although the MoS_2-MCM-41 composite material could be synthesized with the use of polar aprotic solvent DMF and $(NH_4)_2MoS_4$ as precursor, DMF and $(NH_4)_2MoS_4$ are neither cost-effective nor environmentally- friendly.

Table 9 Cu^{2+} adsorption capacities of MoS_2/MCF				
Adsorbent	Adsorption capacity of Cu^{2+}(mg/g)	% removal	S content(wt%)[1]	Calculated MoS_2 content(wt%)[2]
MoS_2-NN-MCF	79.44 ± 0.65	58.9%	18.30 ± 0.21	45.75
DTC-MoS_2-MCF-0.06	12.1 ± 0.86	9.0%	3.80 ± 0.04	9.50
DTC-MoS_2-MCF-0.24	73.30 ± 1.20	54.5%	9.62 ± 0.09	24.05 wt %
MoS_2-1:4	135.57 ± 0.56	99.5%	Not applicable	Not applicable
[Initial Cu^{2+} concentration 1 mM, dose = 0.5 g/L, pH 5.0, 250 rpm, 298 K, 24 hours] 1, S content(wt%) based on elemental analysis 2, MoS_2 content was calculated based on S content and assumption pure MoS_2 has 40 wt% of S				

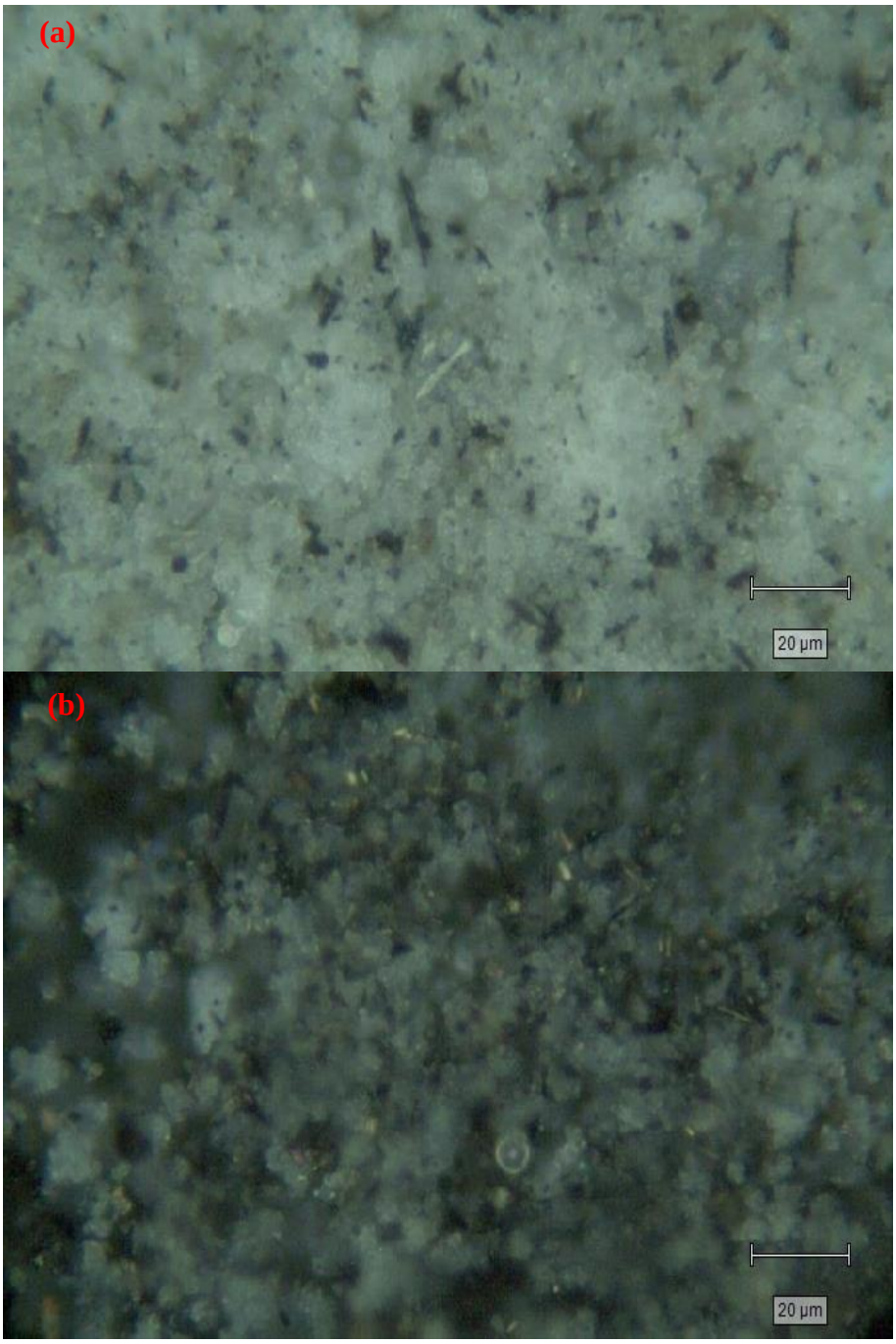

Figure 4 Microscope images (50x) of (a) DTC-MoS_2-MCF-0.06, (b) DTC-MoS_2-MCF-0.24, (c) MoS_2-NN-MCF, (d) MCF.

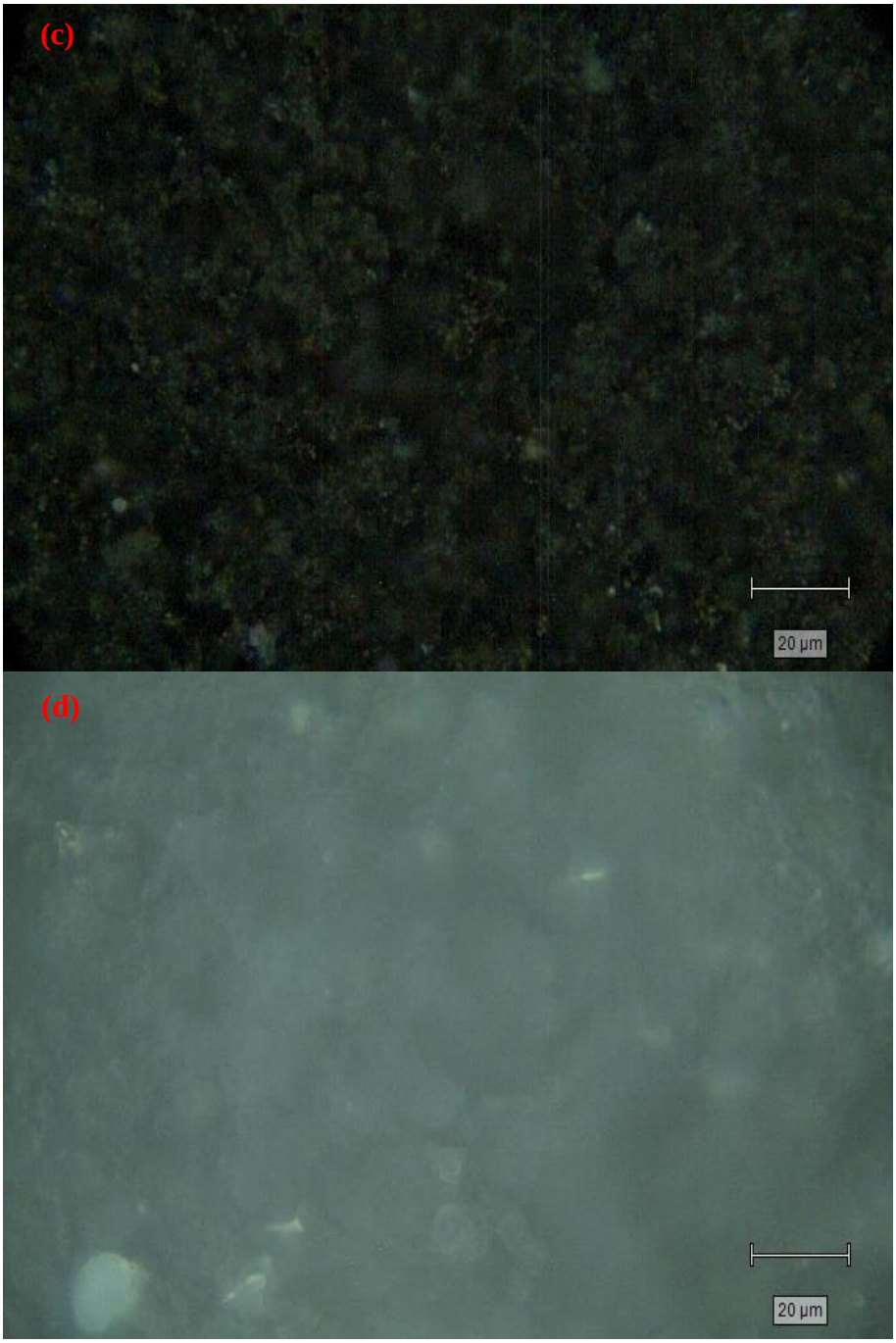

Figure 4 (continued) Microscope images (50x) of (a) DTC-MoS_2-MCF-0.06, (b) DTC-MoS_2-MCF-0.24, (c) MoS_2-NN-MCF, (d) MCF.

4.3 Characterization

4.3.1 SEM

The SEM images of bulk-MoS_2, MoS_2-1:2, MoS_2-1:4, MoS_2-1:7 and MoS_2-1:4-Cu are shown in Figures 5 – 9. Cu-laden MoS_2-1:4 was named MoS_2-1:4-Cu. The bulk MoS_2 contained plate-like particles with a lateral size of 200 to 2,000 nm and a smooth surface (Figure 5). The morphology of MoS_2-1:2 as displayed in Figure 6 is nanosheet-assembled MoS_2 nanoflowers with diameters ranging from 200 to 400 nm. This nanoflower structure was similar to other MoS_2 materials reported in the literature.[75] Figures 7 – 8 reveal that both MoS_2-1:4 and MoS_2-1:7 were rock-like, irregular and rough particles with sizes between 10 to 50 µm. The large sizes of MoS_2-1:4 and MoS_2-1:7 were beneficial to water treatment because the adsorbents could easily be separated from the liquid phase by sedimentation or filtration. The high-magnification (~55,000x) SEM images of MoS_2-1:4 and MoS_2-1:7 indicate that these two samples looked like wire-brush and were made up of an aggregation of MoS_2 nanoflakes with edge site exposure. The results of the high-magnification view concur with the XRD and XPS results, indicating the abundant S_2^{2-} species existing in the edges of MoS_2 nanosheets whose structure should be single or few-layered. In addition, the EDX reveals that the Mo:S atomic ratios of all MoS_2 samples were close to 1:2 (1:1.85-2.02). Figure 10 displays the SEM images and EDX elemental mapping of MoS_2-1:4 after Cu^{2+} adsorption using 1 mM Cu^{2+} solution for 24 h contact time. The Cu^{2+} loaded MoS_2-1:4 (MoS_2-1:4-Cu) showed similar morphology as the pristine MoS_2-1:4. The EDX elemental mapping reveals that the adsorbed Cu^{2+} was evenly distributed on the surface of MoS_2-1:4.

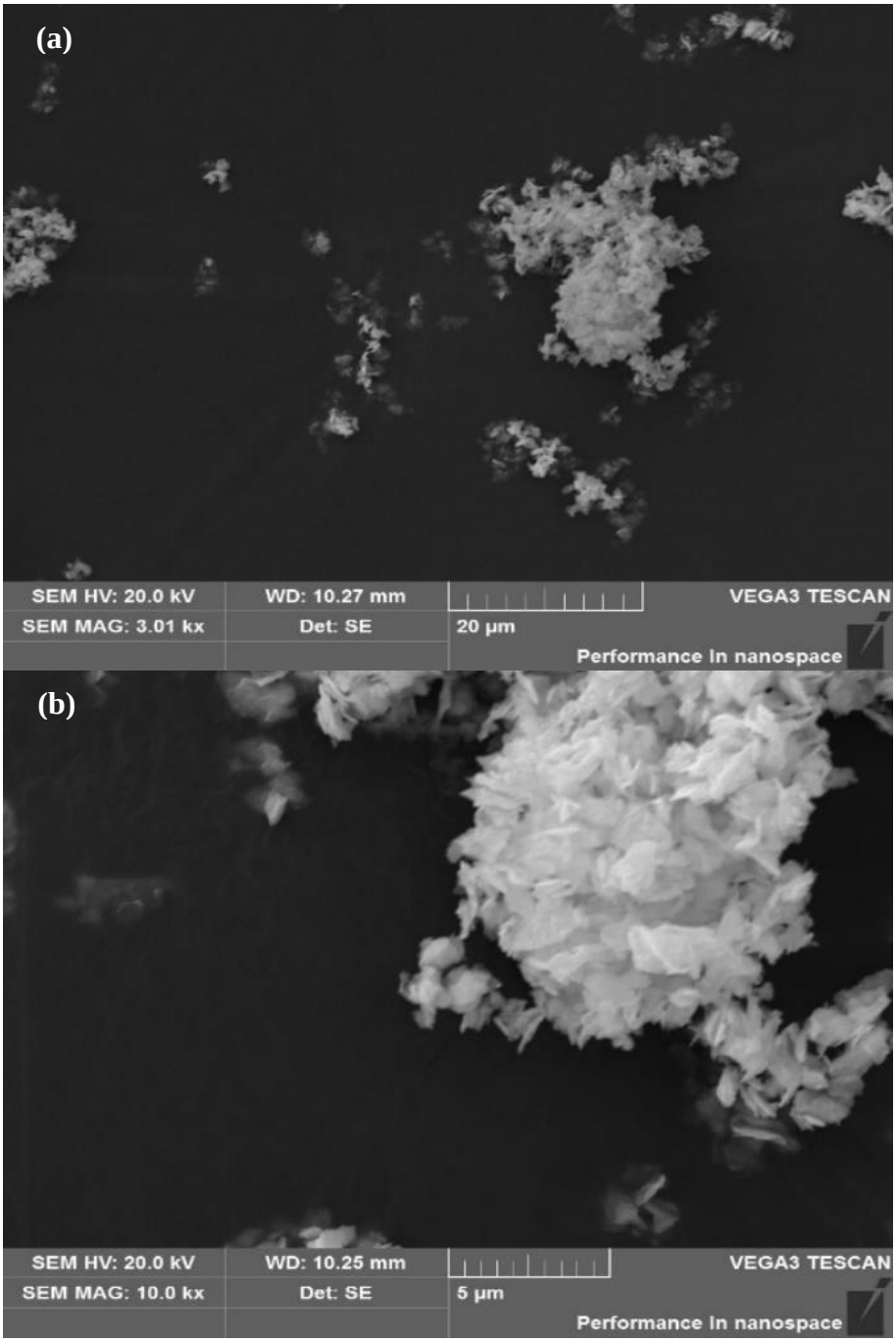

Figure 5 SEM images of bulk-MoS_2 (a) 3,000x, (b) 10,000x, (c) 20,000x.

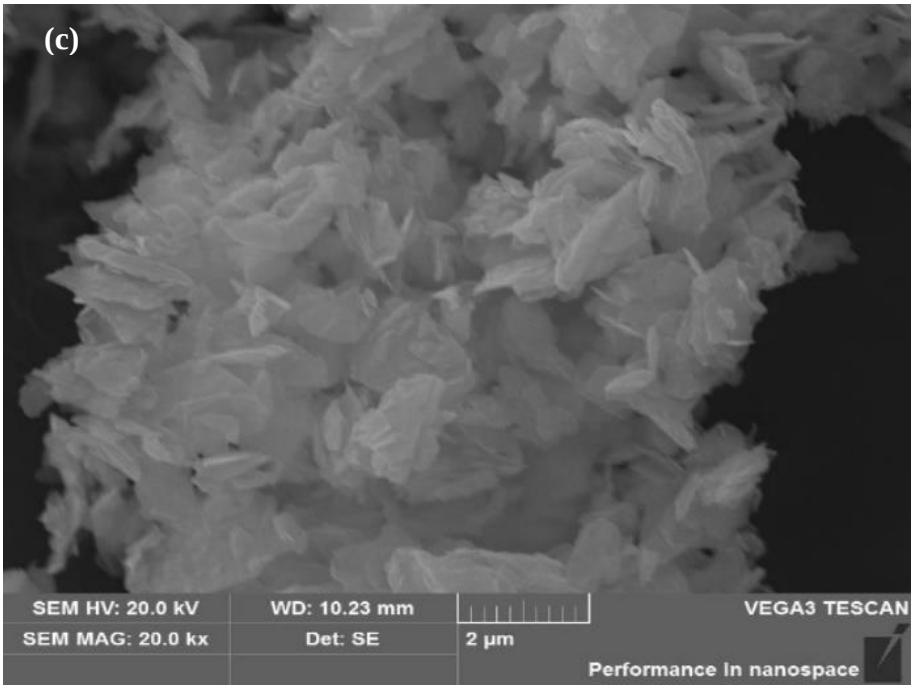

Figure 5 (continued) SEM images of bulk-MoS_2 (a) 3,000x, (b) 10,000x, (c) 20,000x.

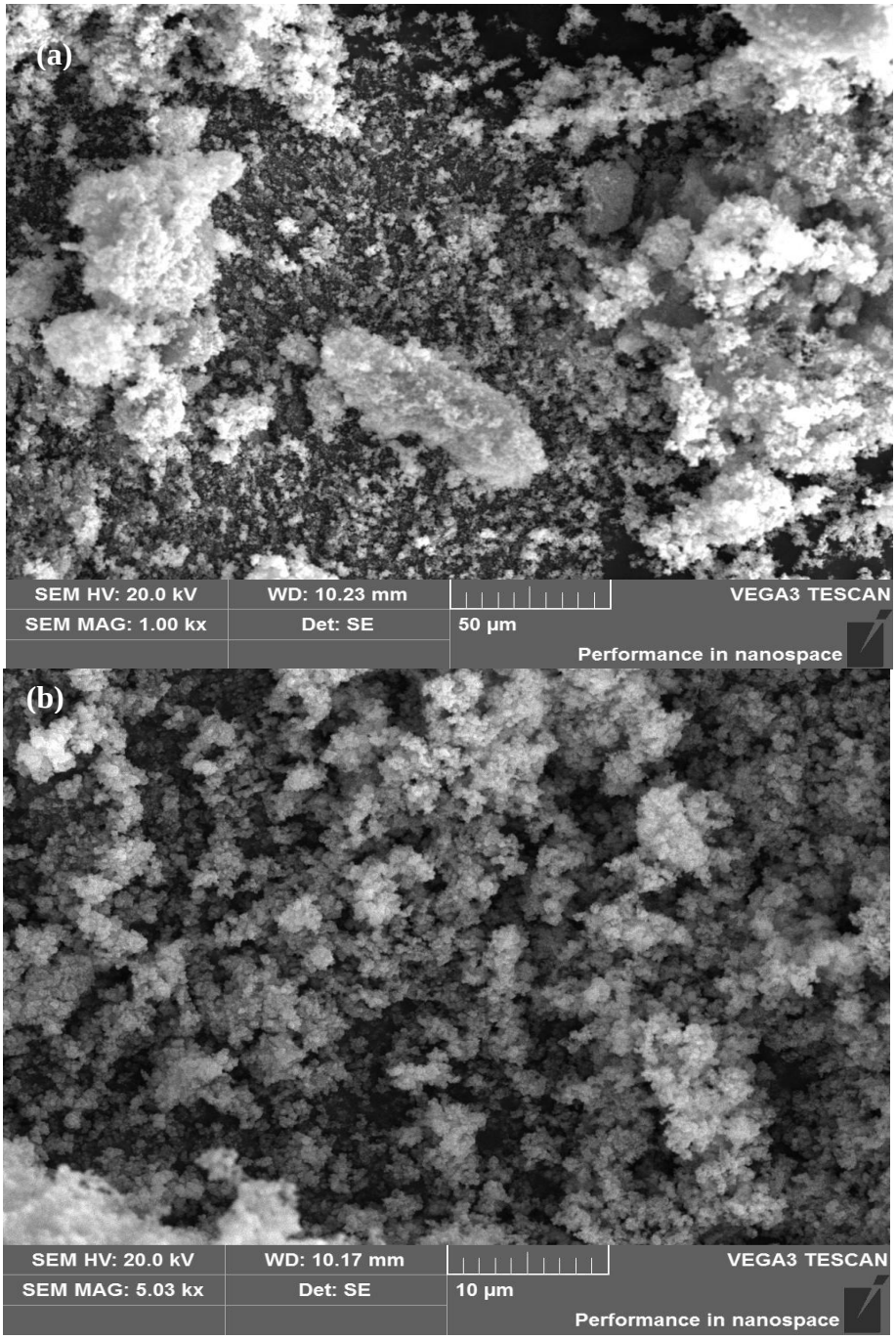

Figure 6 SEM images of MoS_2-1:2 (a) 1,000x, (b) 5,000x, (c) 20,000x, (d) 50,000x.

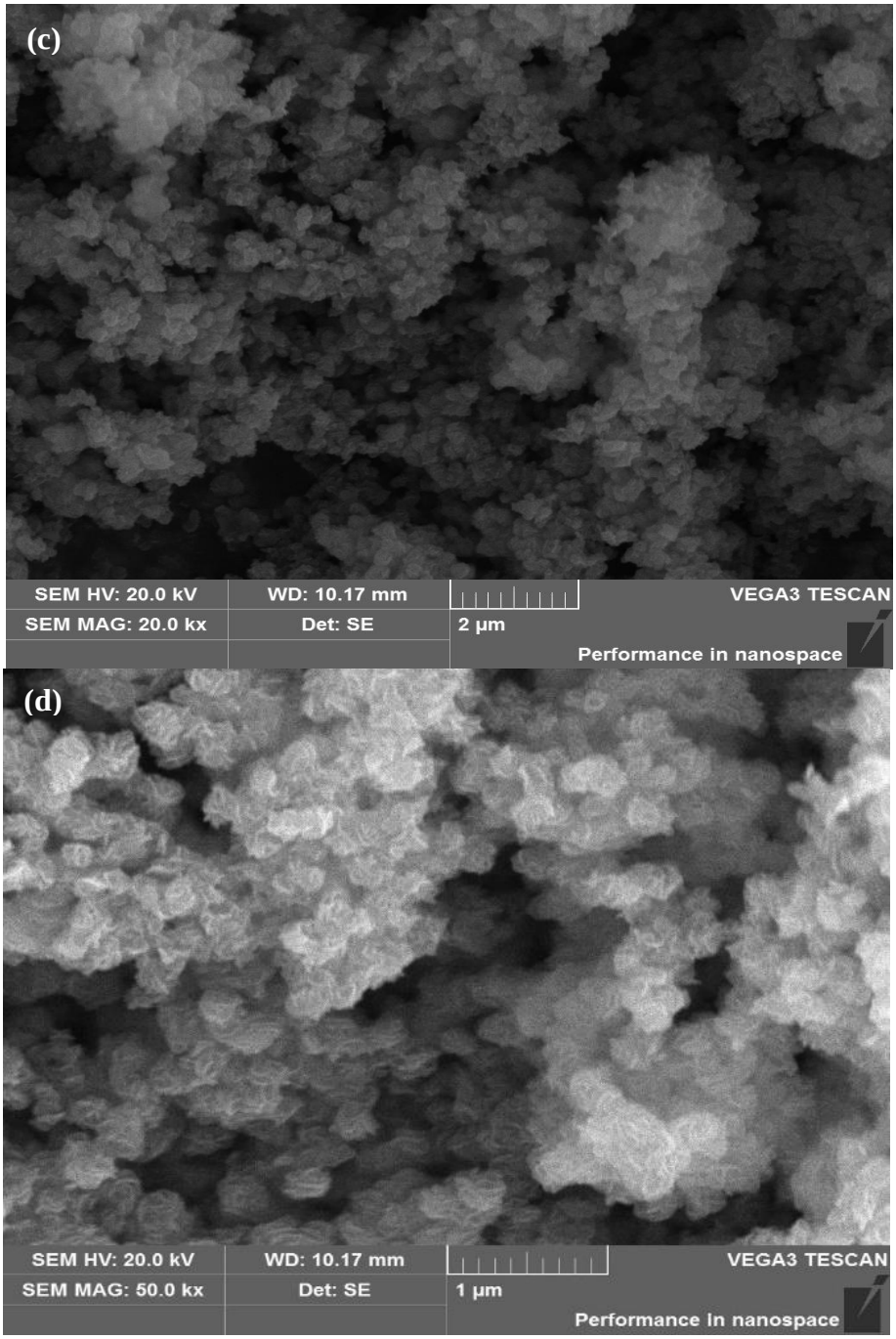

Figure 6 (continued) SEM images of MoS_2-1:2 (a) 1,000x, (b) 5,000x, (c) 20,000x, (d) 50,000x.

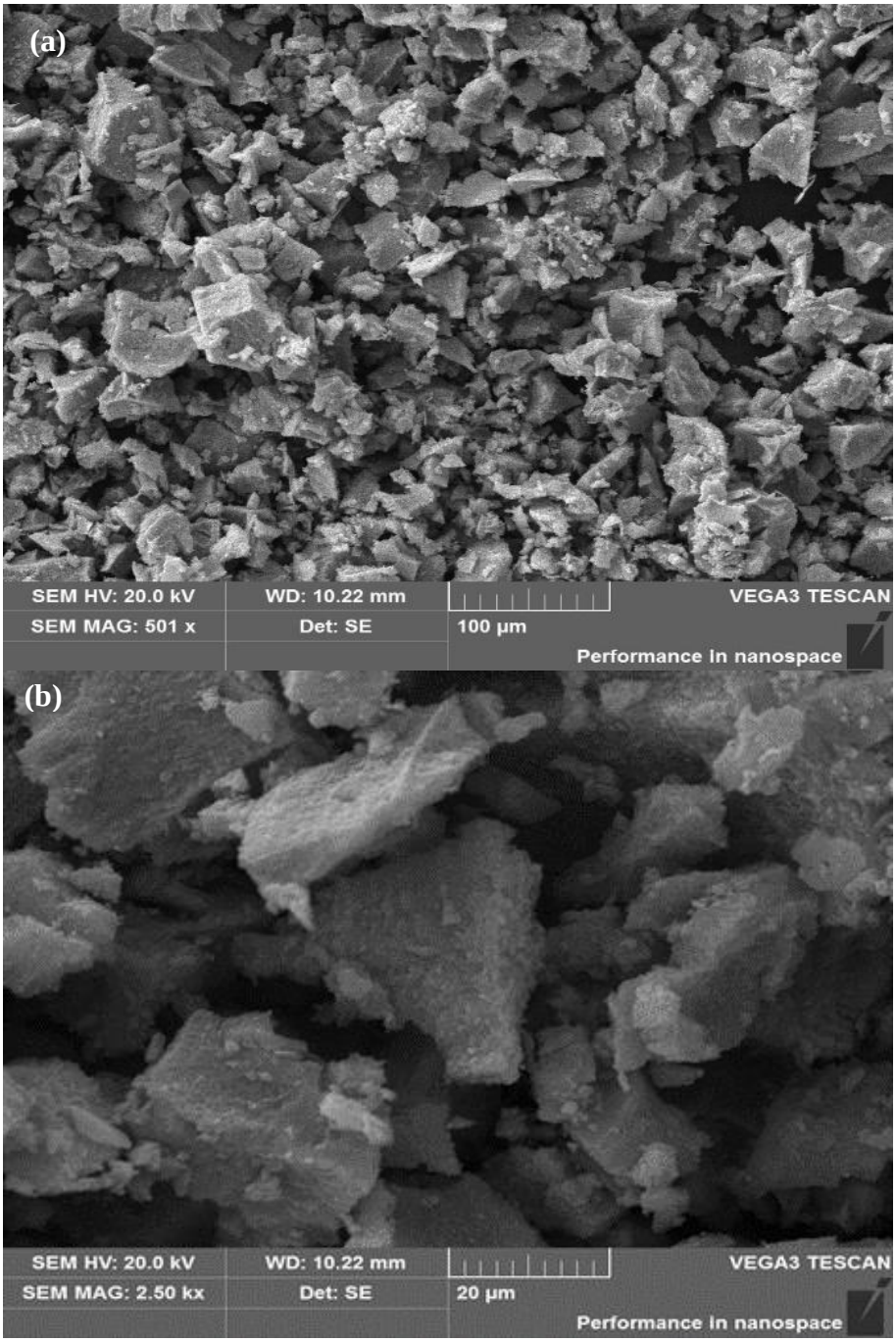

Figure 7 SEM images of MoS_2-1:4 (a) 1,000x, (b) 2,500x, (c) 5,000x, (d) 56,500x.

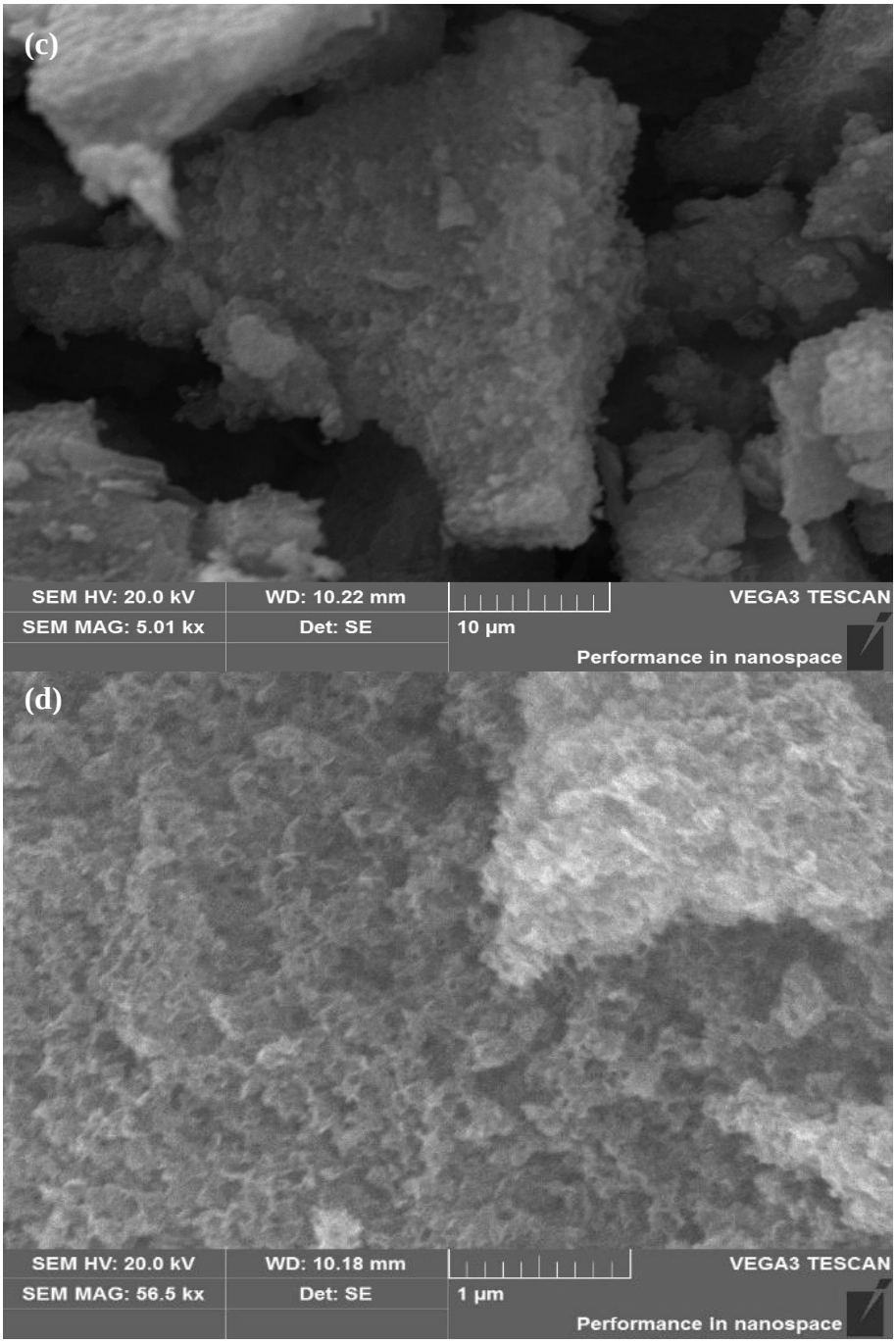

Figure 7 (continued) SEM images of MoS_2-1:4 (a) 1,000x, (b) 2,500x, (c) 5,000x, (d) 56,500x.

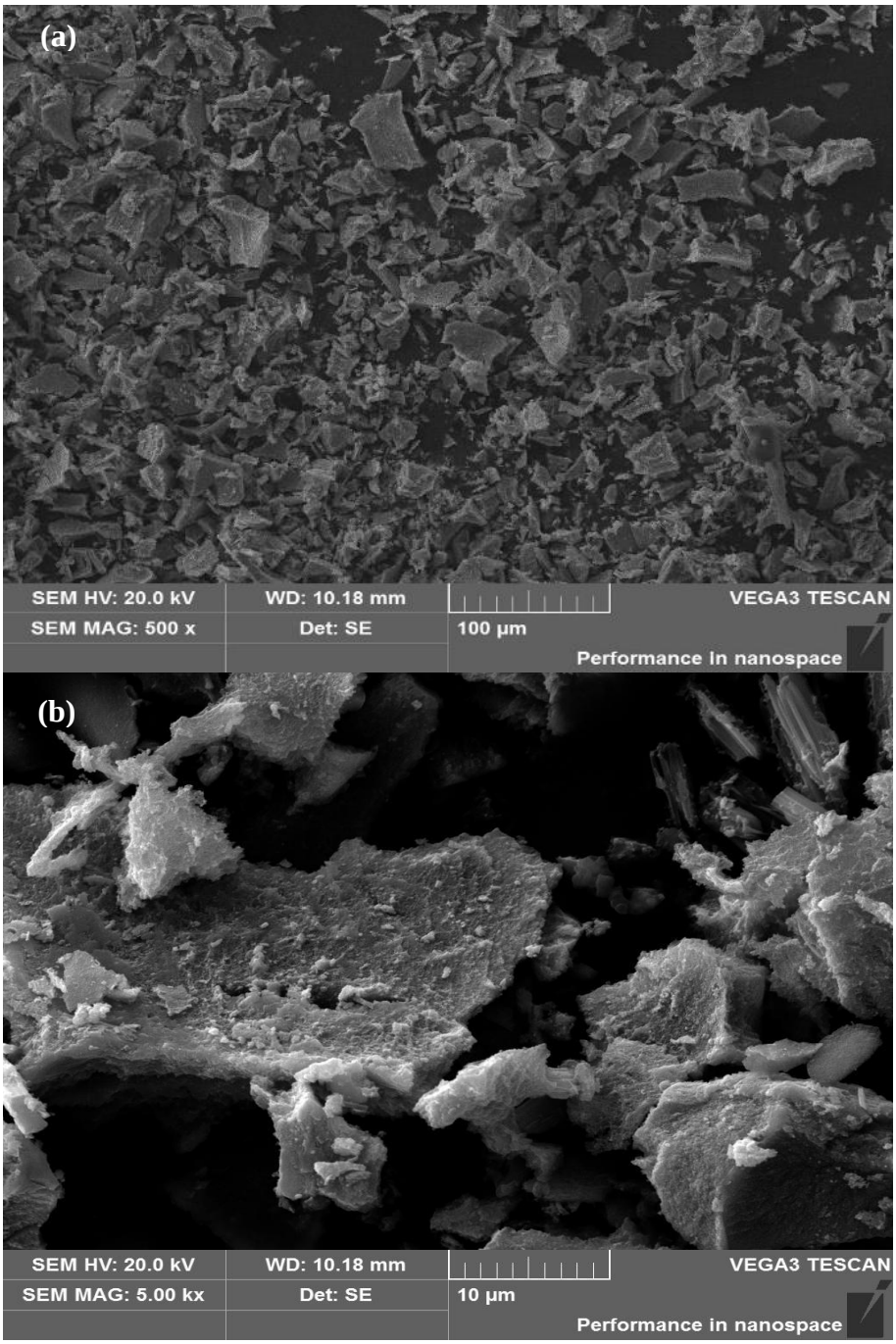

Figure 8 SEM images of MoS_2-1:7 (a) 500x, (b) 5,000x, (c) 20,000x, (d) 55,800x.

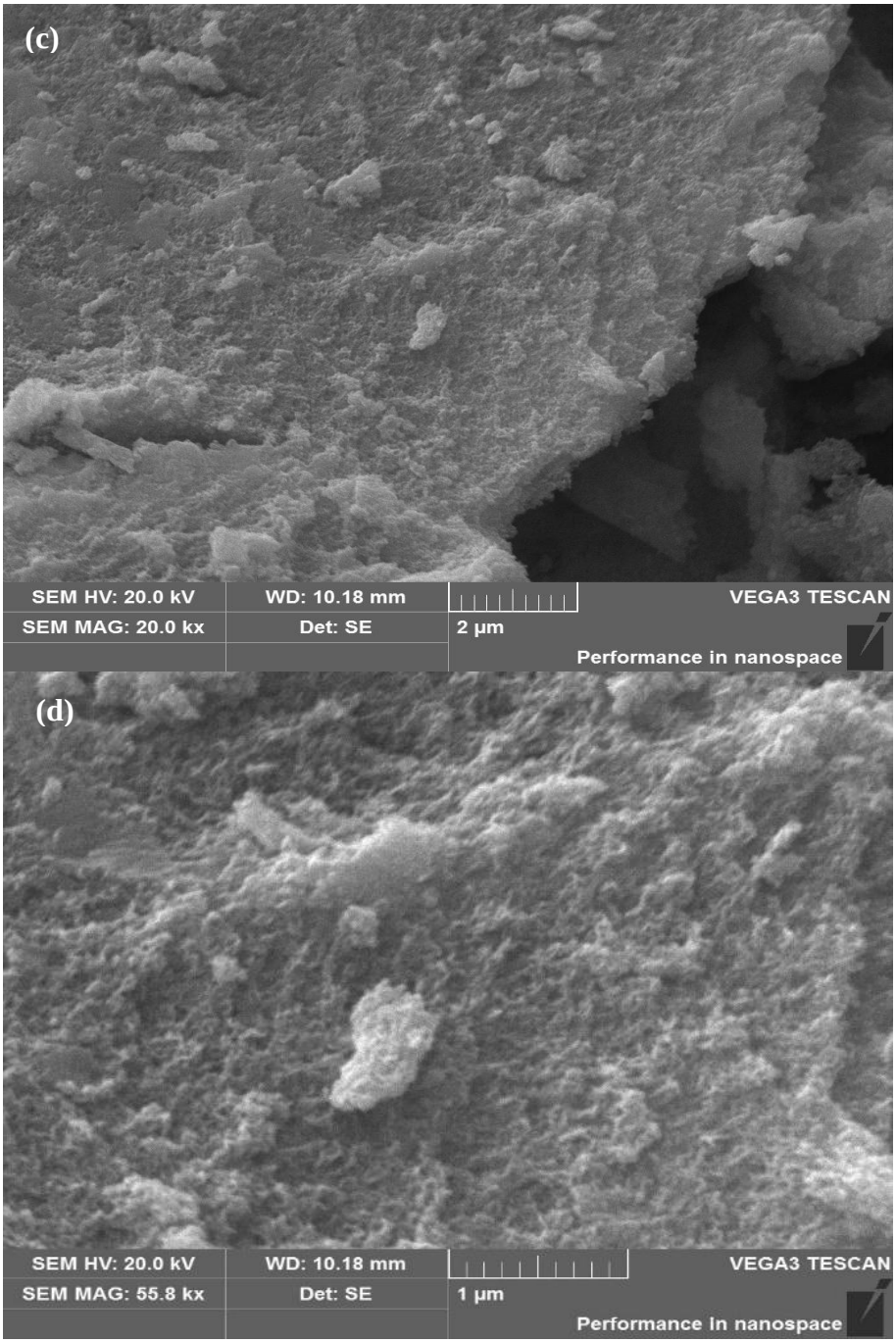

Figure 8 (continued) SEM images of MoS_2-1:7 (a) 500x, (b) 5,000x, (c) 20,000x, (d) 55,800x.

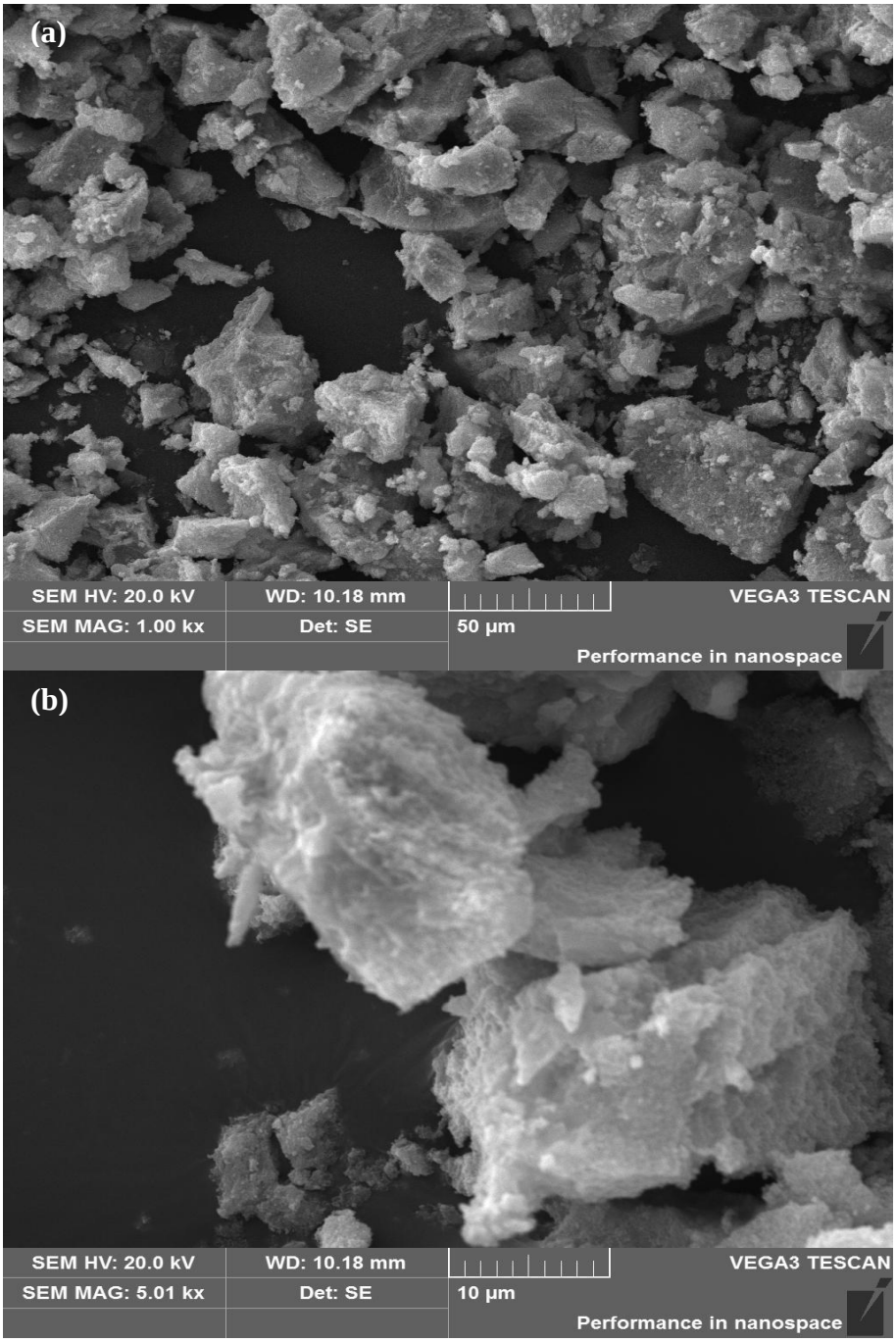

Figure 9 SEM images of MoS_2-1:4-Cu (a) 1,000x, (b) 5,000x, (c) 20,000x, (d) 55,000x.

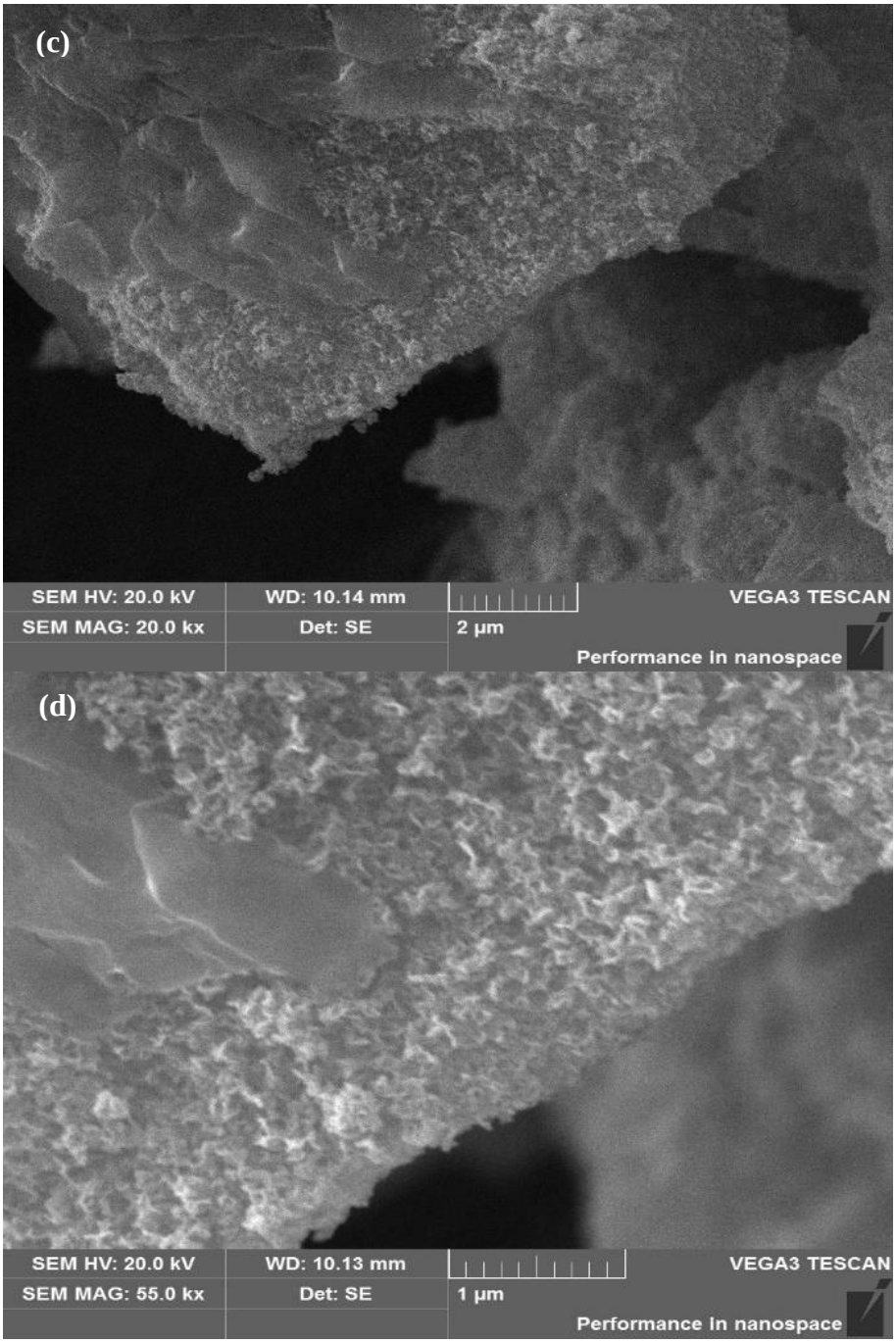

Figure 9 (continued) SEM images of MoS_2-1:4-Cu (a) 1,000x, (b) 5,000x, (c) 20,000x, (d) 55,000x.

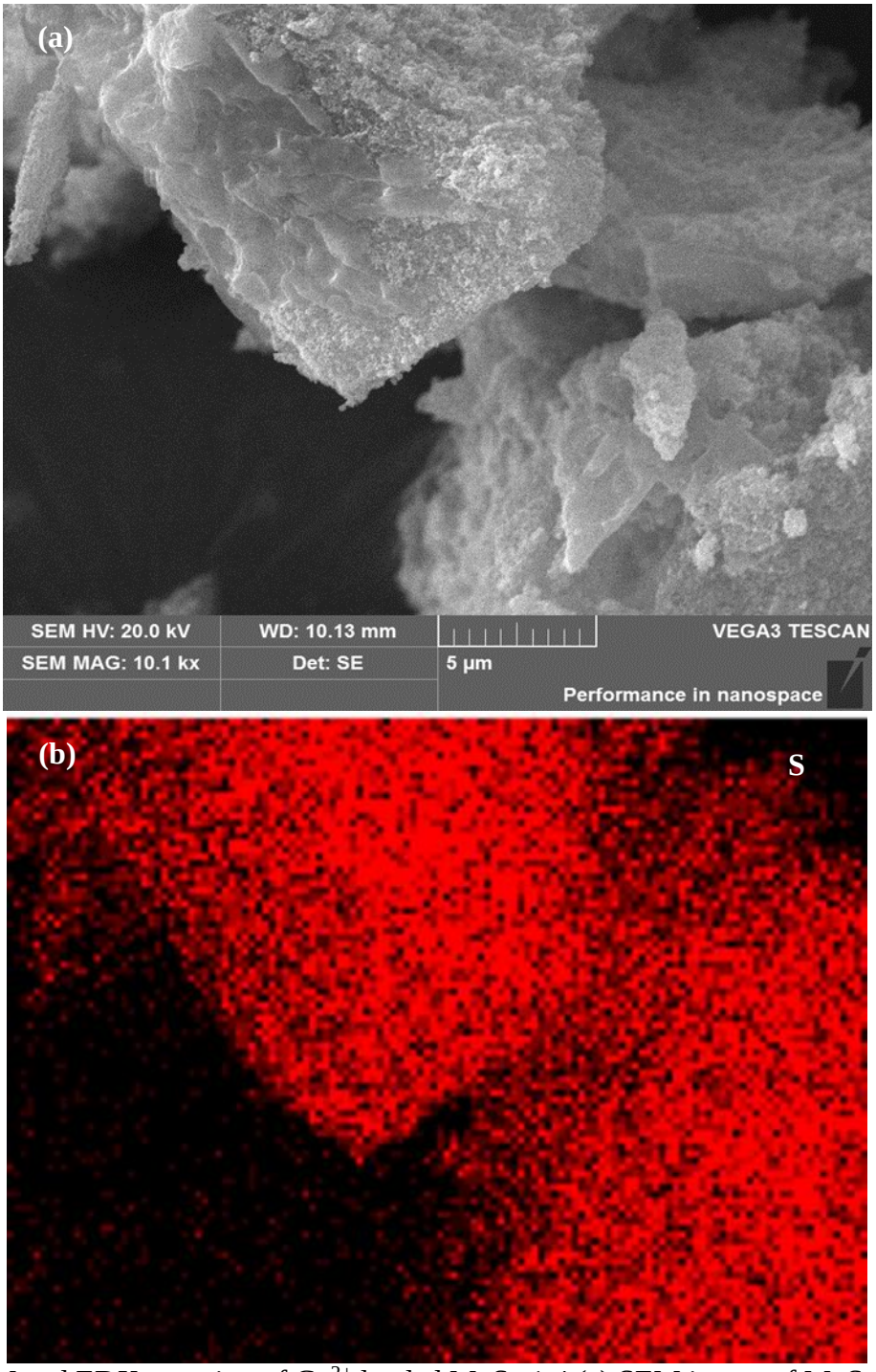

Figure 10 SEM and EDX mapping of Cu^{2+} loaded MoS_2-1:4 (a) SEM image of MoS_2-1:4-Cu (10,000x), (b)-(d) EDX elemental mapping images of S, Cu and Mo.

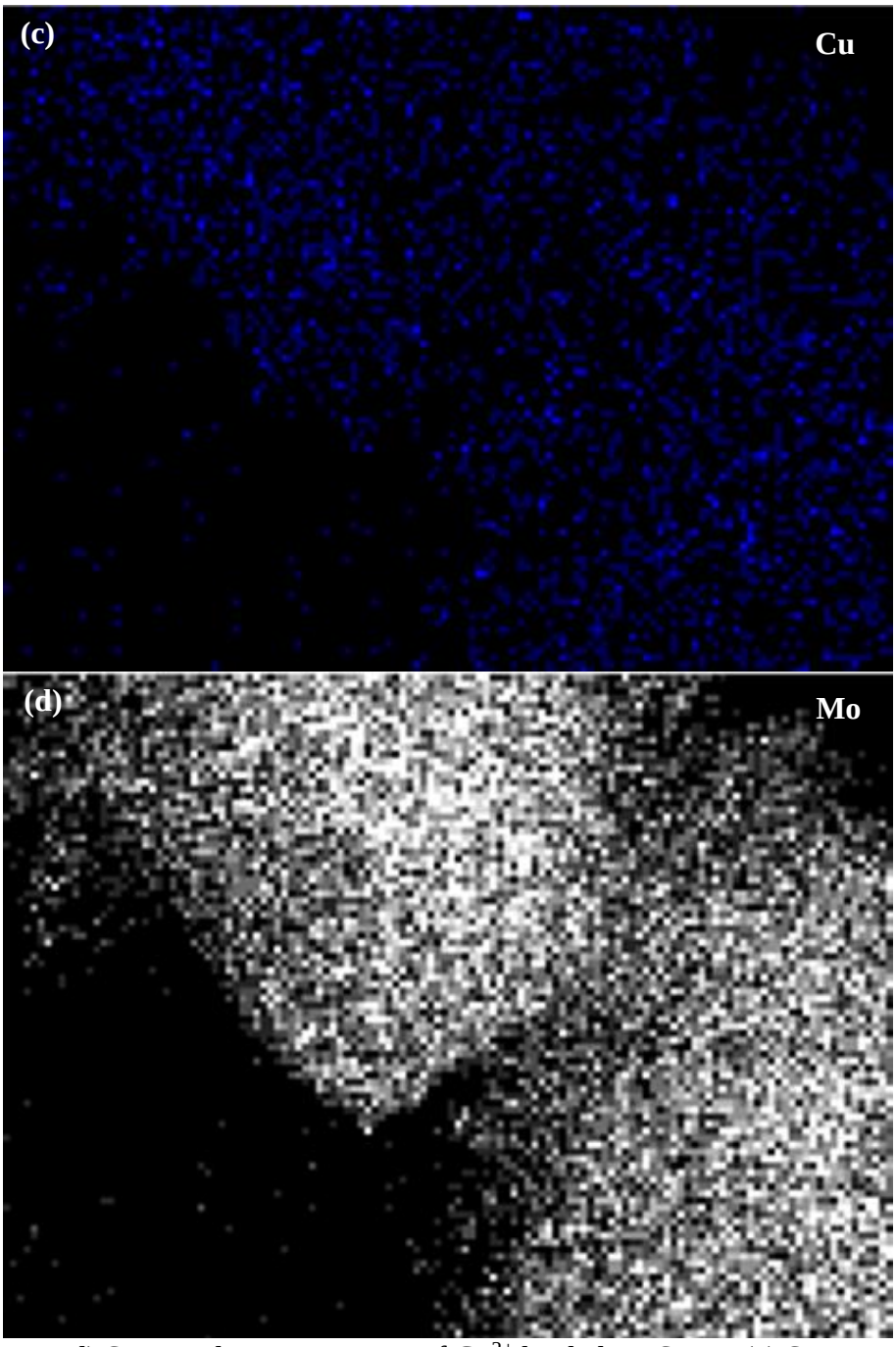

Figure 10 (continued) SEM and EDX mapping of Cu^{2+} loaded MoS_2-1:4 (a) SEM image of MoS_2-1:4-Cu (10,000x), (b)-(d) EDX elemental mapping images of S, Cu and Mo.

Figure 11 summarizes the SEM images of MCF and MoS_2-NN-MCF. As shown in Figure 11, MCF and MoS_2-NN-MCF were aggregated sphere particles with a diameter of about 1,000 nm. The morphology of the MCF remained similar after the hydrothermal treatment, indicating the high hydrothermal stability of MCF. Figure 11d reveals that small particles, which were probably MoS_2, were attached to the surface of MoS_2-NN-MCF. EDX elemental mapping in Figure 12 demonstrates that MoS_2 was evenly distributed on NN-MCF. The results of the EDX mapping and SEM confirmed that the hydrothermal sulfidation method had successfully incorporated MoS_2 into MCF.

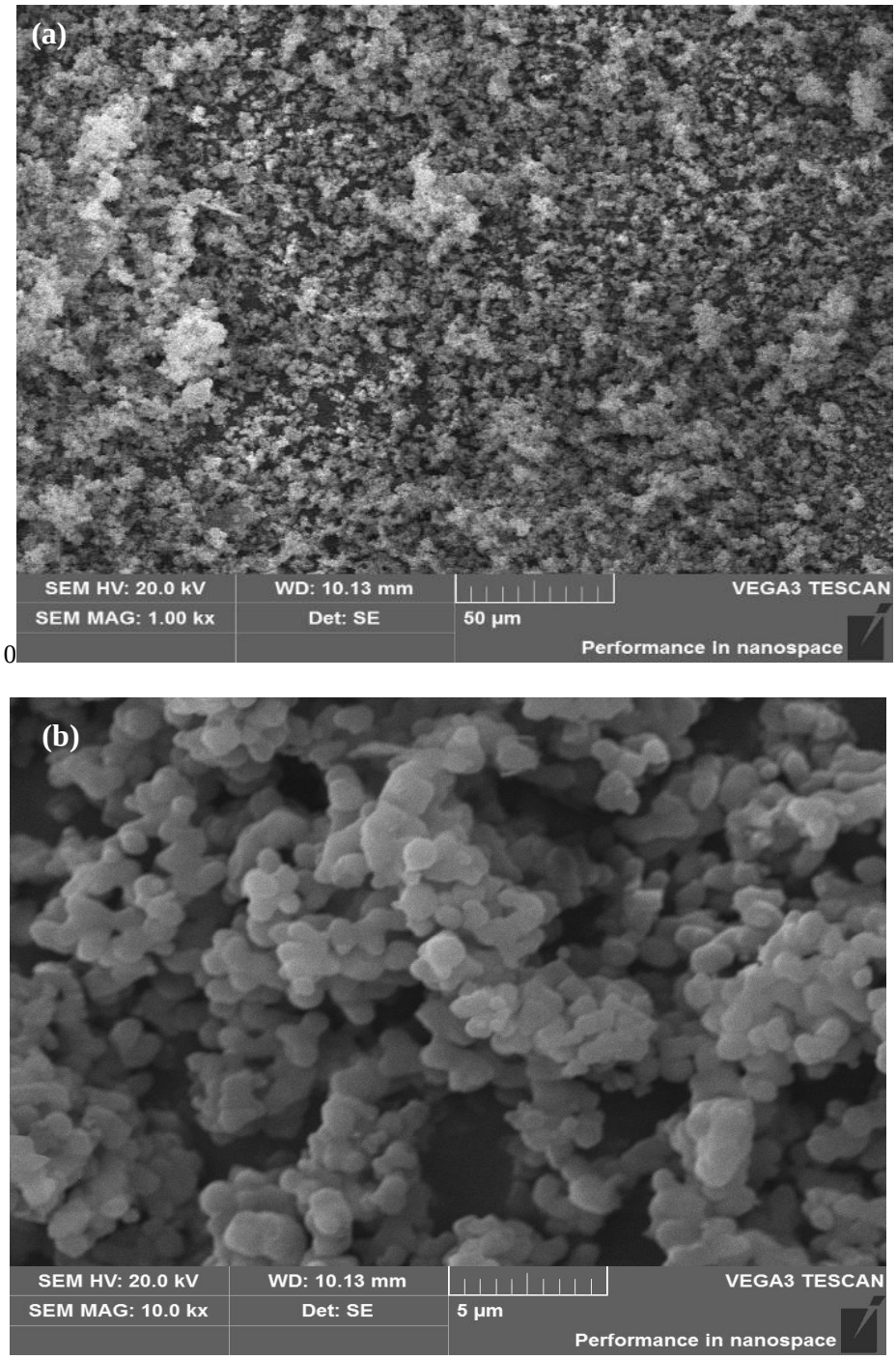

Figure 11 SEM images of MCF and MoS_2-NN-MCF. SEM images of MCF (a) 1,000x, (b) 10,000x; SEM images of MoS_2-NN-MCF (c) 10,00x, (d) 10,000x.

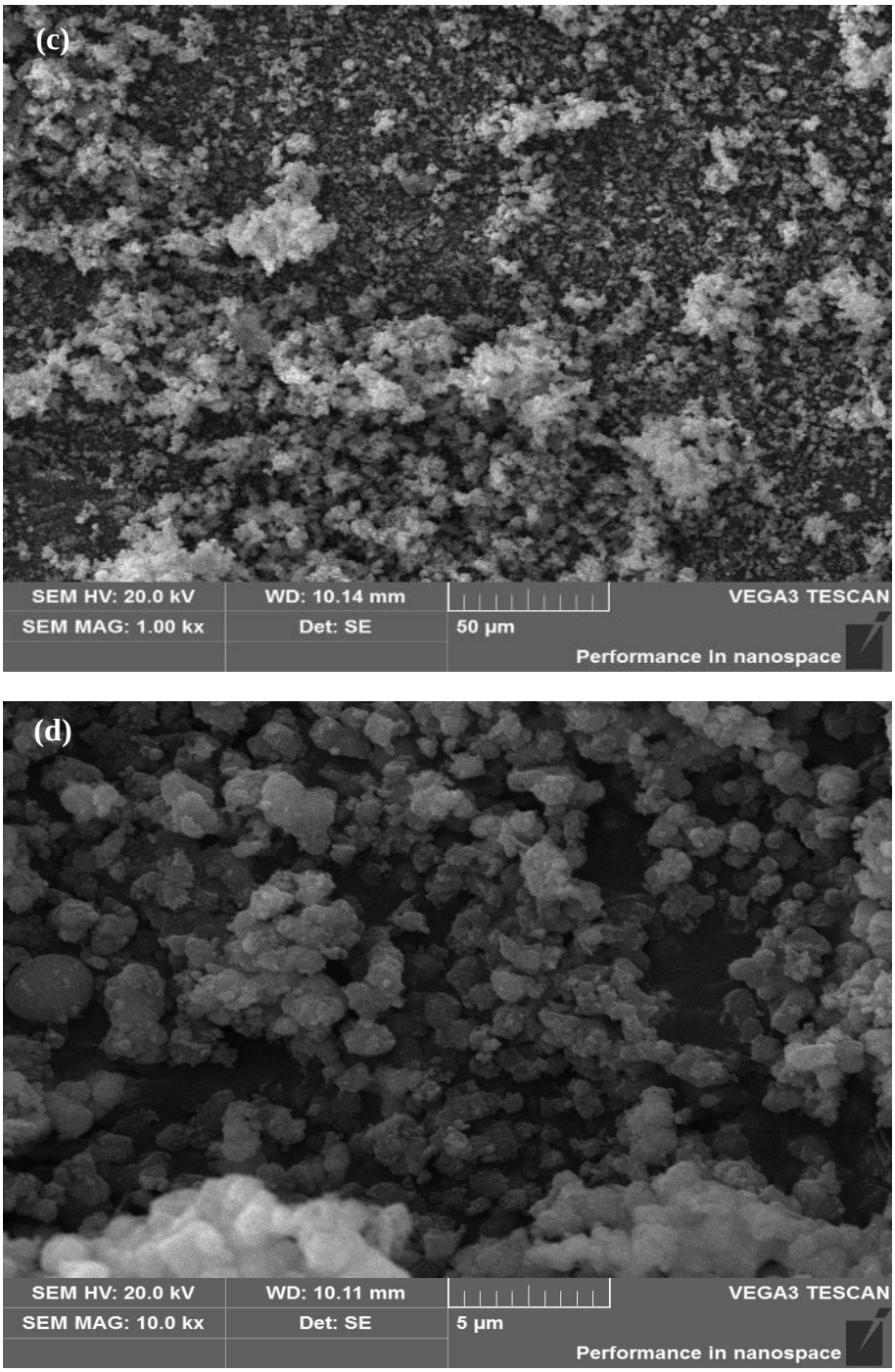

Figure 11 (continued) SEM images of MCF and MoS_2-NN-MCF. SEM images of MCF (a) 1,000x, (b) 10,000x; SEM images of MoS_2-NN-MCF (c) 10,00x, (d) 10,000x.

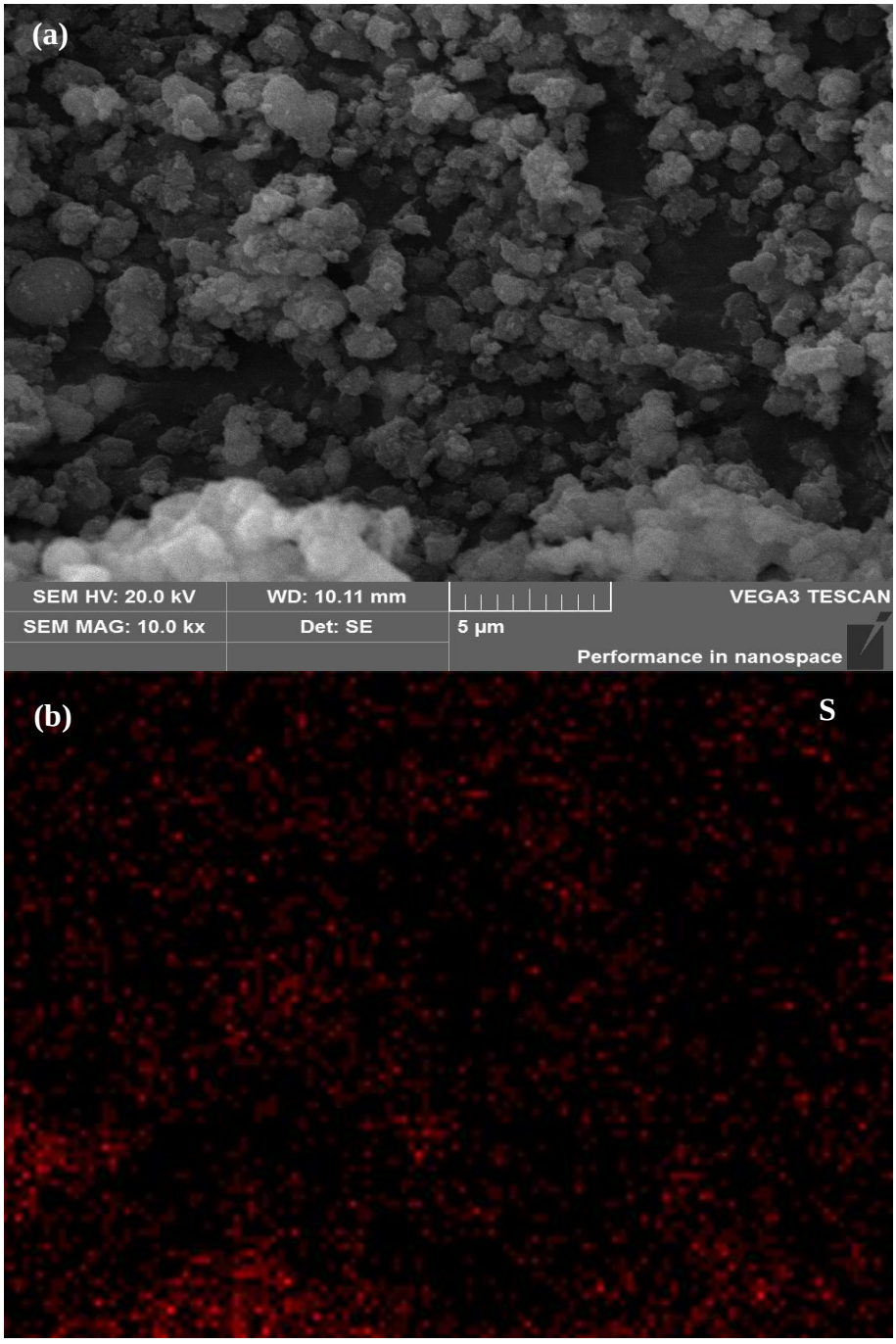

Figure 12 SEM and EDX mapping of MoS_2-NN-MCF (a) SEM image of MoS_2-NN-MCF (10,000x), (b)-(d) EDX elemental mapping images of S, Si and Mo.

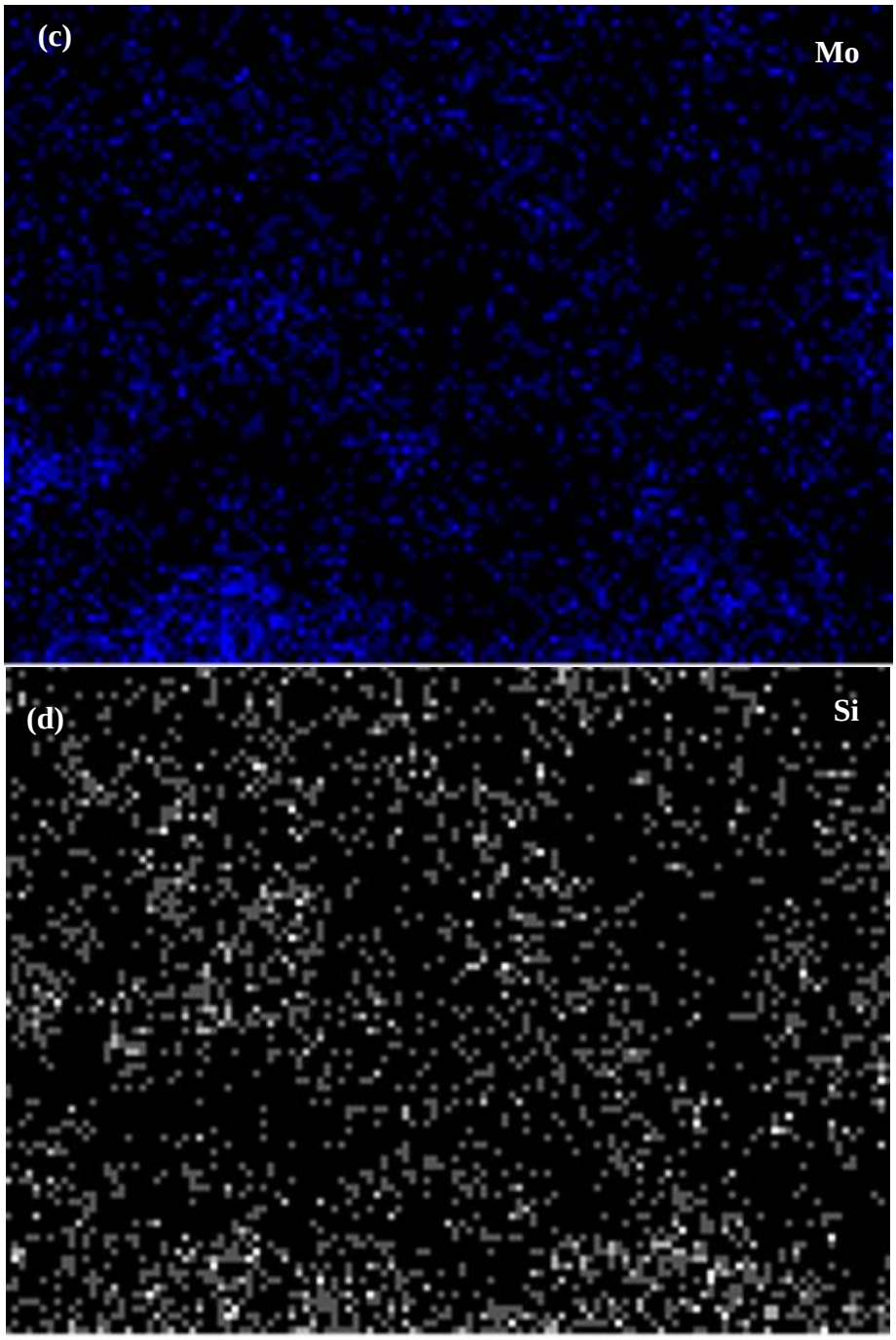

Figure 12 (continued) SEM and EDX mapping of MoS_2-NN-MCF (a) SEM image of MoS_2-NN-MCF (10,000x), (b)-(d) EDX elemental mapping images of S, Mo and Si.

4.3.2 N_2-adsorption/desorption isotherms

Table 10 lists the BET surface area, total pore volume and Cu^{2+} adsorption capacities of different MoS_2-based adsorbents and MCF. The bulk-MoS_2 and MoS_2-1:7 exhibited a smaller surface area and total pore volume ~~as~~ compared with MoS_2-1:2 and MoS_2-1:4. Both mesopores and macropores (>50 nm) contributed to the total pore volume in MoS_2-NN-MCF, MoS_2-1:4, MoS_2-1:7 and MoS_2-1:2, and the contribution of mesopores was more significant than that of macropores in MoS_2-1:4 and MoS_2-1:7. Over 90% of the total pore volume in MCF was attributed to mesopores (2 – 50 nm). Figure 13 shows that the N_2 adsorption/desorption isotherm of bulk-MoS_2 was classified as type III isotherm, while the isotherms of the other three samples belonged to type IV isotherm with H3 hysteresis loop. The BET surface area and total pore volume of MoS_2-1:2 were larger than those of bulk-MoS_2, but only negligible Cu^{2+} adsorption was observed for both MoS_2-1:2 and bulk-MoS_2. As a result, the data in Table 10 shows that that the total pore volume and surface area might not be a controlling factor for efficient Cu^{2+} adsorption by MoS_2.

N_2 gas adsorption isotherms and Barret–Joyner–Halenda (BJH) pore size distribution of MCF and MoS_2-NN-MCF are summarized in Figure 14. The BET surface area, pore volume, narrow pore size distribution (mainly 22 nm) and H1 hysteresis loop in type IV isotherm were similar to those reported for MCF in the literature[77, 89], indicating that MCF was successfully synthesized. Compared with MCF, the BET surface area and pore volume of MoS_2-NN-MCF dropped significantly. The pore size distribution of MoS_2-NN-MCF also became broader. The result indicated that amino-group grafting and MoS_2

loading blocked the pores and surface of MCF, leading to a reduction in the surface area and pore volume. Further study could be conducted to optimize the amount of amino-group grafting and MoS_2 loading in MCF.

Table 10 Effect of surface area and pore volume on Cu^{2+} adsorption capacities of different MoS_2 samples

Material	BET surface area (m^2/g)	Total pore volume (cm^3/g)	Adsorption capacity of Cu^{2+}(mg/g)
Bulk-MoS_2	16.20 ± 0.21	0.074 ± 0.002	8.04 ± 3.418[b]
MoS_2-1:2	95.51 ± 0.06	0.369 ± 0.001	13.8 ± 1.26[b]
MoS_2-1:4	71.34 ± 0.02	0.415 ± 0.001	184.25 ± 0.58[b] 135.57 ± 0.56[a]
MoS_2-1:7	15.19 ± 0.15	0.054 ± 0.001	161.14 ± 7.00[b]
MCF	676.24 ± 30.15	2.098 ± 0.09	NA
MoS_2-NN-MCF	60.39 ± 0.22	0.428 ± 0.01	79.44 ± 0.65[a]

NA: not available
a: Initial Cu^{2+} concertation = 1 mM
b: Initial Cu^{2+} concertation = 2 mM

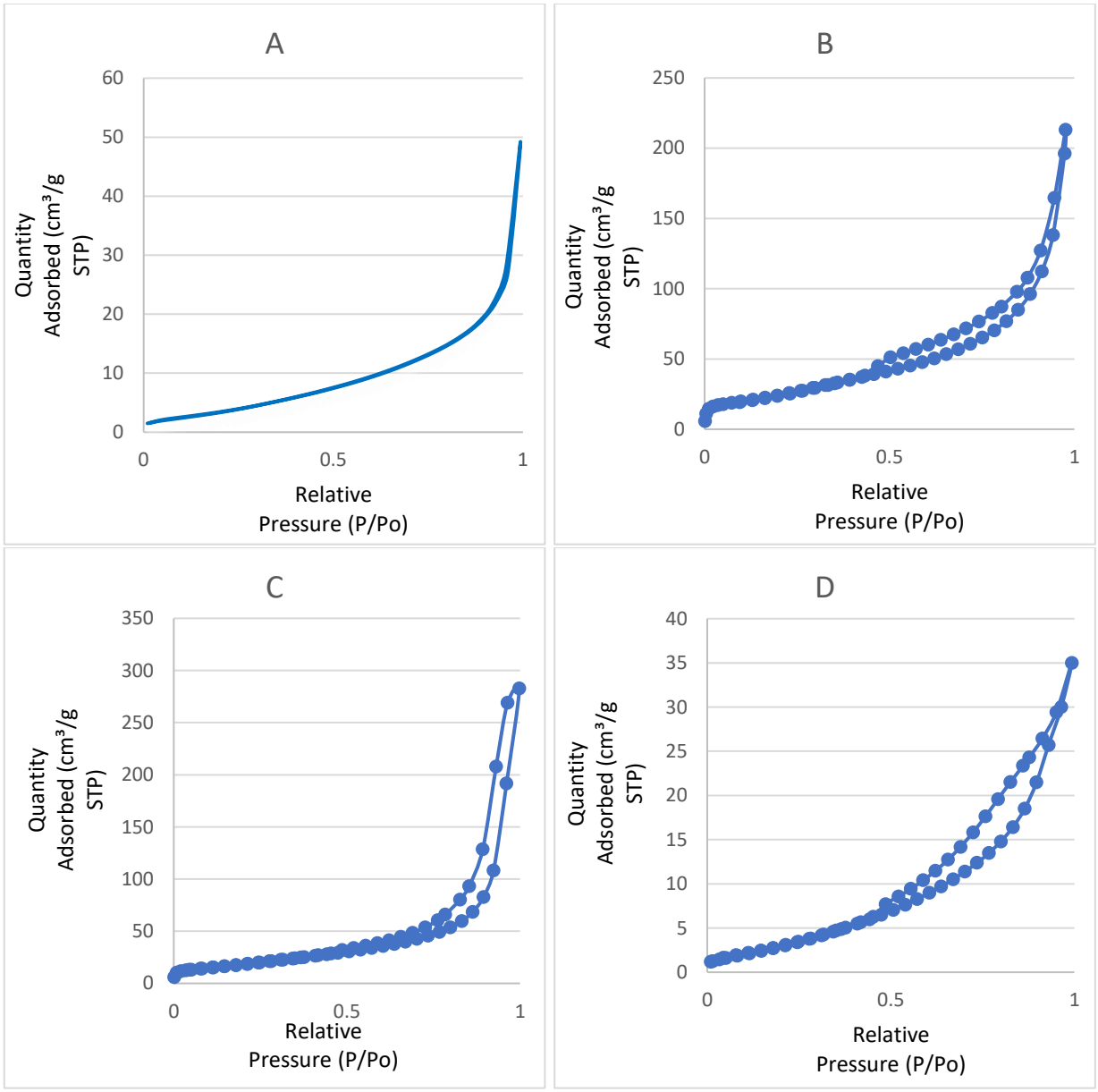

Figure 13 N_2 gas adsorption isotherms of A (bulk-MoS_2), B (MoS_2-1:2), C (MoS_2-1:4), D (MoS_2-1:7).

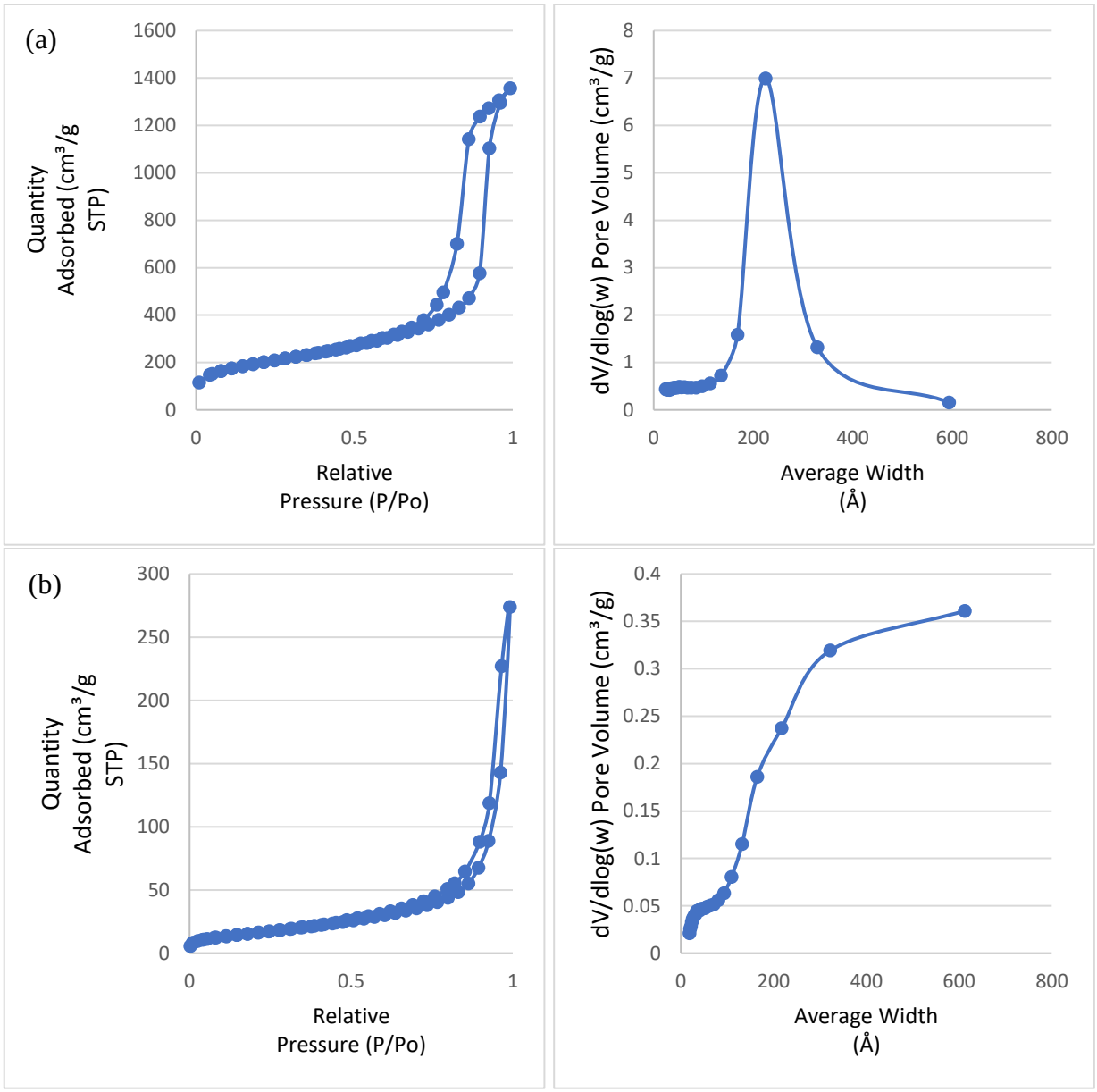

Figure 14 N_2 gas adsorption isotherms (left) and Barret–Joyner–Halenda (BJH) pore size distribution (right) of (a) MCF, and (b) MoS_2-NN-MCF.

4.3.3 XRD

Figure 15 shows the XRD diffraction patterns of bulk-MoS_2, MoS_2-1:2, MoS_2-1:4, MoS_2-1:7 and MoS_2-1:4-Cu. The diffraction peaks of (002) in MoS_2-1:4, MoS_2-1:7 and MoS_2-1:4-Cu were very weak, and shifted to an angle lower than that of bulk-MoS_2. Weak or even no (002) diffraction was typically found in the single- or few-layered MoS_2 nanosheet[90] and MoS_2 with low crystallinity[91]. Besides, the diffraction peak of (002) in bulk MoS_2 and MoS_2-1:2 was 14.7 ^{o} and 14.0 ^{o} respectively, which corresponded to the interlayer distances of 0.61 and 0.63 nm respectively, using Bragg's law. The relatively sharp peaks in the X-ray diffraction pattern of MoS_2-1:2 at 14.0 ^{o}, ~33 ^{o} and ~57 ^{o} indicated the high crystallinity of MoS_2-1:2. In MoS_2-1:2, MoS_2-1:4, MoS_2-1:7 and MoS_2-1:4-Cu, the two broad diffractions which peak at ~33 ^{o} and ~57 ^{o} could be assigned to (100) and (110) planes of MoS_2, indicating the analogous arrangement of Mo and S atoms along the basal plane.[92-93] The high index peaks such as (103) and (105) in MoS_2-1:2, MoS_2-1:4, MoS_2-1:7 and MoS_2-1:4-Cu were rarely observed in other exfoliated or synthetic MoS_2 nanosheets.[87,94] Furthermore, the characteristic XRD peaks of CuS, CuO, Cu_2S and Cu_2O were absent in MoS_2-1:4-Cu, suggesting that the adsorbed Cu^{2+} on MoS_2-1:4 did not form any large copper oxide or copper sulfide crystals.[95]

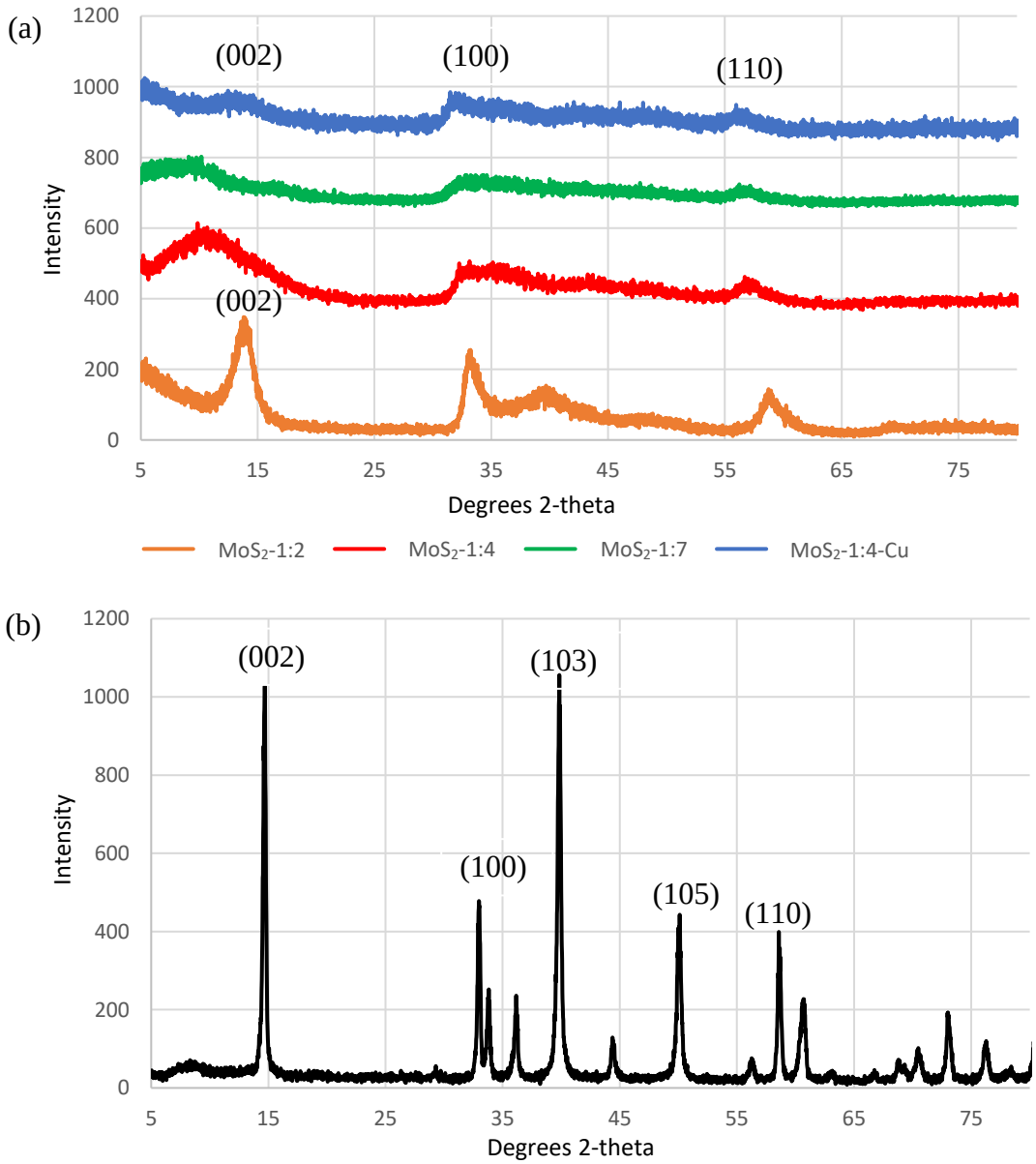

Figure 15 XRD diffraction patterns of (a) MoS_2-1:2, MoS_2-1:4, MoS_2-1:7, MoS_2-1:4-Cu and (b) bulk-MoS_2.

4.3.4 Raman spectroscopy

The Raman spectra of various MoS_2 samples are illustrated in Figures 16 -18. Characteristic Raman shifts of in-plane E^1_{2g} and the out-of-plane A_{1g} vibration of MoS_2 at about 378 cm^{-1} and 402 cm^{-1} respectively were found in all the tested samples. The two characteristic Raman shifts indicated that the MoS_2 samples were successfully synthesized. Additionally, no significant Raman peak shifting was observed in the MoS_2 samples, as compared with bulk-MoS_2. This result indicated that the thickness of the MoS_2 nanosheets in the samples might be more than six layers.[96]

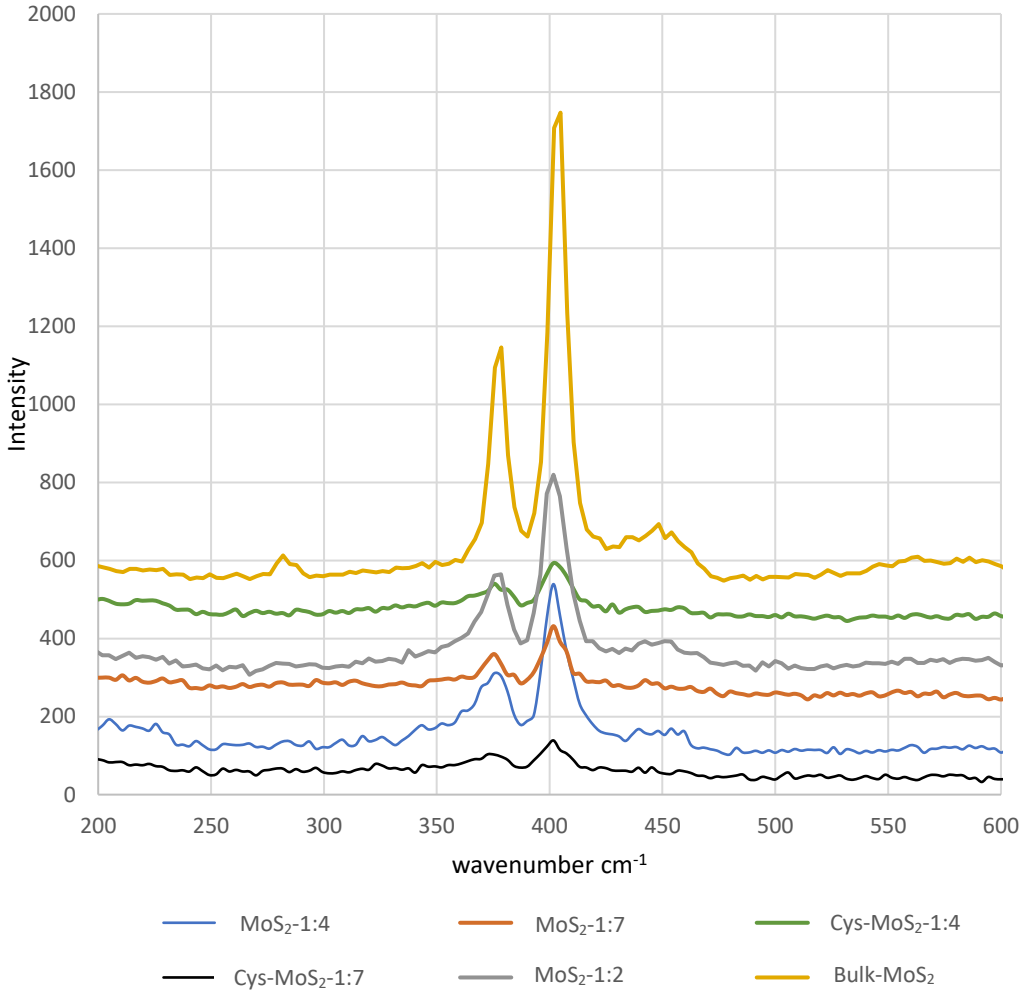

Figure 16 Raman spectra of MoS_2 prepared under different synthetic and pretreatment conditions.

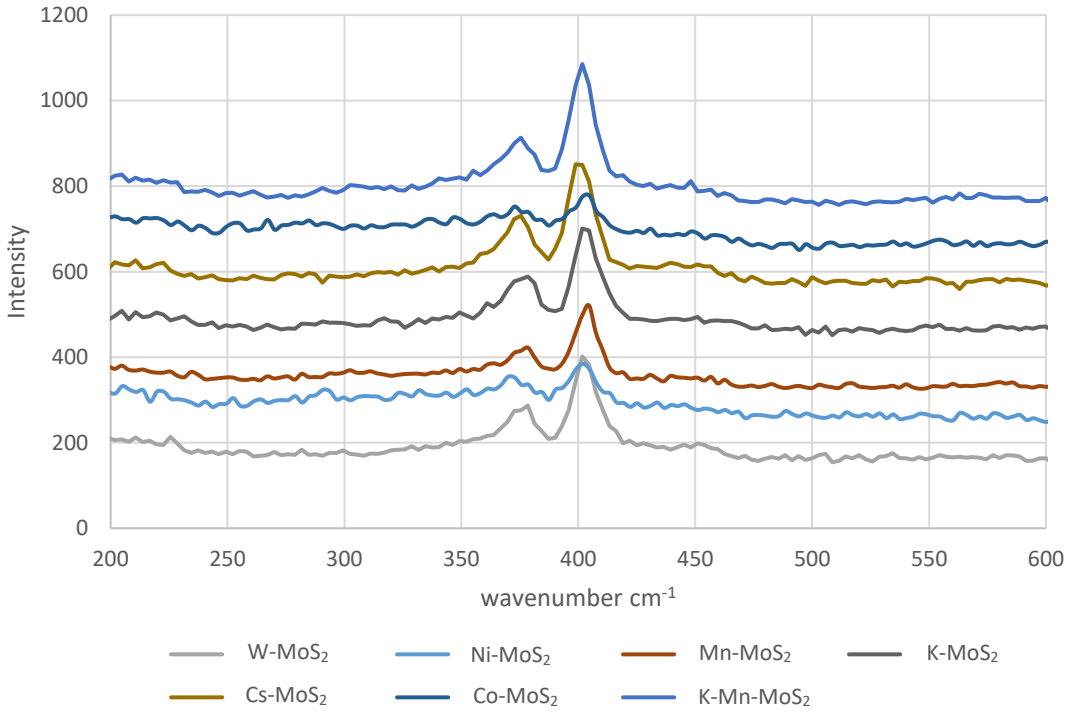

Figure 17 Raman spectra of metal-doped MoS_2.

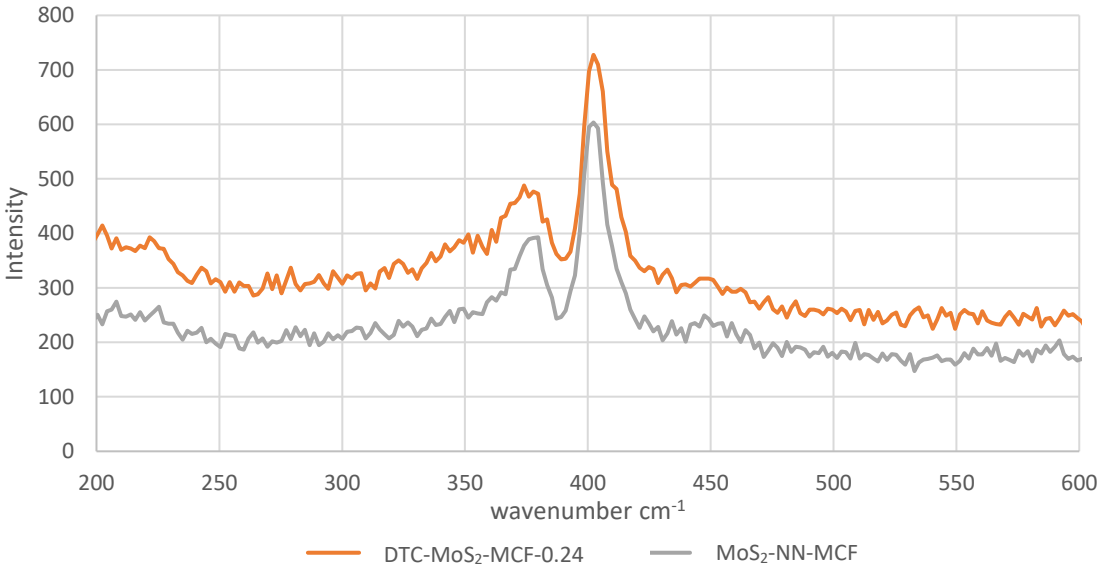

Figure 18 Raman spectra of DTC-MoS_2-MCF-0.24 and MoS_2-NN-MCF.

4.3.5 Elemental analysis

Elemental analysis could determine the purity of MoS_2 materials and the loading of MoS_2 in MoS_2-NN-MCF, DTC-MoS_2-MCF-0.06 and DTC-MoS_2-MCF-0.24 samples. The elemental contents of various MoS_2 samples are summarized in Table 11. MoS_2-NN-MCF contained 1.58 wt% N and 4.29 wt% C due to the grafting of amino-functional groups. Although MoDTC-2 (MoS_2 precursor for the preparation of DTC-MoS_2-MCF-0.24 and DTC-MoS_2-MCF-0.06) contained N and C, the elemental analysis revealed that the DTC-MoS_2-MCF-0.24 and DTC-MoS_2-MCF-0.06 were almost free of residuals N and C. These results indicated that the hydrothermal treatment of MoDTC-2 with thioacetamide solution could produce MoS_2 with high purity. Other MoS_2 samples only contained trace amounts of N, H, C residues, while the S content was close to the theoretical MoS_2 value of 40 wt %. The elemental analysis of MoS_2 samples confirmed the successful synthesis of high purity MoS_2.

Table 11 Elemental analysis of various MoS_2 samples.

Materials	N(wt%)	C(wt%)	H(wt%)	S(wt%)
MoS_2-NN-MCF	1.58 ± 0.13	4.29 ± 0.08	1.70 ± 0.10	18.30 ± 0.21
DTC-MoS_2-MCF-0.06	0.05 ± 0.01	0.00 ± 0.00	0.79 ± 0.01	3.80 ± 0.04
DTC-MoS_2-MCF-0.24	0.09 ± 0.03	0.04 ± 0.04	1.47 ± 0.05	9.62 ± 0.09
MoS_2-1:2	0.00 ± 0.00	0.00 ± 0.00	0.53 ± 0.15	38.69 ± 0.35
MoS_2-1:4	0.59 ± 0.01	0.02 ± 0.01	0.65 ± 0.02	42.46 ± 0.14
MoS_2-1:7	1.05 ± 0.01	0.82 ± 0.01	1.42 ± 0.04	41.46 ± 0.40
Air-dried MoS_2-1:7	1.15 ± 0.01	0.30 ± 0.00	1.5 ± 0.01	41.91 ± 0.31
Oven-dried MoS_2-1:7	0.59 ± 0.01	0.02 ± 0.01	0.65 ± 0.02	42.46 ± 0.14
Freeze-dried MoS_2-1:7	0.85 ± 0.01	0.29 ± 0.38	1.07 ± 0.10	42.64 ± 0.02
Cs-MoS_2	0.59 ± 0.01	0.02 ± 0.01	0.65 ± 0.02	42.46 ± 0.14
Ni-MoS_2	1.32 ± 0.01	0.57 ± 0.01	1.41 ± 0.04	43.46 ± 0.12
K-Mn-MoS_2	0.40 ± 0.01	0.00 ± 0.00	0.69 ± 0.03	41.15 ± 0.07
W-MoS_2	0.74 ± 0.02	0.02 ± 0.00	0.71 ± 0.04	41.29 ± 0.08
Co-MoS_2	0.58 ± 0.04	0.02 ± 0.00	1.99 ± 0.02	41.93 ± 0.07

4.3.6 XPS analysis of MoS_2-1:2, MoS_2-1:4 and MoS_2-1:7

The surface compositions of MoS_2-1:4-Cu, MoS_2-1:4, fresh MoS_2-1:4, MoS_2-1:2, reused MoS_2-1:4, bulk-MoS_2, CS_2-MoS_2-1:4 and MoS_2-1:7 were analyzed by XPS. The XPS results (Table 12) show that all MoS_2 samples were mainly composed of Mo, S, O and C. The MoS_2-1:4-Cu and reused MoS_2-1:4 also contained Cu. MoS_2-1:4-Cu was Cu-loaded MoS_2-1:4. The reused MoS_2-1:4 was MoS_2-1:4-Cu after regeneration by 1M HCl. CS_2-MoS_2-1:4 was MoS_2-1:4 washed with CS_2 several times to eliminate possibilities of elemental S contamination. The atomic ratios of Mo:S ranged from 1.88 to 2.71 (MoS_2-1:4-Cu=2.66, MoS_2-1:4=2.60, fresh MoS_2-1:4=2.58, MoS_2-1:2=2.07, reused MoS_2-1:4=2.64, CS_2-MoS_2-1:4=2.49, bulk-MoS_2-1:4=1.88 and, MoS_2-1:7=2.71). The atomic ratios of the MoS_2 samples were not close to the theoretical MoS_2 ratio of 2. By subtracting the atomic concentration of SO_x^- from the total atomic concentration of S element, the ratios ranged from 1.7-2.39 (MoS_2-1:4-Cu=2.34, MoS_2-1:4=2.16, fresh MoS_2-1:4=2.16, MoS_2-1:2=1.70, reused MoS_2-1:4 =2.36, CS_2-MoS_2-1:4=2.19, bulk-MoS_2=1.88 and, MoS_2-1:7=2.39) resulted. The adsorption of H_2O, O_2, CO_2 and the adventitious hydrocarbon from XPS equipment on the MoS_2 samples might contribute to the detection of O and C elements.[97]Additionally, the detection of O in the MoS_2 samples could also be attributed to the formation of SO_x^-.

Table 12 Atomic and mass concentrations of MoS_2 samples determined by XPS analysis

	Atomic concentration (%)							Mass concentration (%)						
Sample	Na	Cu	O	N	C	Mo	S	Na	Cu	O	N	C	Mo	S
MoS_2 1:4-Cu	0.02	9.5	20.17	0	12.3	15.84	42.17	0.01	15.29	8.18	0	3.74	38.51	34.26
MoS_2-1:4[a]	0.21	0.02	27.46	2.22	10.39	16.58	43.12	0.13	0.04	12.29	0.87	3.49	44.49	38.68
Fresh MoS_2-1:4[b]	0.12	0	26.04	1.8	9.19	17.56	45.29	0.08	0	11.28	0.68	2.99	45.63	39.33
MoS_2-1:2	0.02	0	17.89	1.42	4.43	24.82	51.42	0.01	0	6.52	0.45	1.21	54.24	37.56
Reused MoS_2-1:4	NM	2.32	21.69	0.58	10.14	17.89	47.24	NM	3.82	8.99	0.21	3.15	44.46	39.24
Bulk MoS_2	NM	0.13	12.75	0	12.31	26	48.81	NM	0.19	4.62	0	3.35	56.43	35.41
CS_2-MoS_2-1:4	NM	0.09	22.58	0.23	11.86	18.68	46.56	NM	0.15	9.51	0.09	3.75	47.18	39.32
MoS_2-1:7	NM	0.11	14.25	0.78	10.64	20.01	54.14	NM	0.18	5.65	0.27	0.17	47.55	43.01

a: Stored for ~30 day
b: Freshly prepared
NM: Not measured

4.3.6.1 High resolution Mo 3d XPS spectra

that were tested. The binding energy and peak assignments are summarized in Table 13 as follows: Mo^{IV} 3d 5/2 at 228.41 – 228.58 eV, Mo^{IV} 3d 3/2 at 231.50 – 231.80, Mo^{V} 3d 5/2 at 229.45 – 230.06 eV, Mo^{V} 3d 3/2at 232.61 – 233.20 eV, Mo^{VI} 3d 5/2 at 231.83 – 232.54 eV and Mo^{VI} 3d 3/2 at 234.42 – 235.23 eV. Mo species in V and VI oxidation states were present in all tested-samples, and this observation could be attributed to the oxidation of MoS_2. The freshly prepared MoS_2-1:4 (fresh MoS_2-1:4) did not show any significant differences in the concentration of Mo^{V} and Mo^{VI} compared with the MoS_2-1:4 that was stored for about 30 days. Therefore, the oxidation of Mo^{IV} by atmospheric oxygen was insignificant. The atomic concentrations of different Mo chemical states in each sample are illustrated in Figure 20. Except for MoS_2-1:2 and bulk-MoS_2, the Mo atomic concentrations of the three chemical states in other MoS_2 samples were similar to one another. The atomic concentration of Mo^{V} in MoS_2-1:2 and bulk-MoS_2 was lower than that of other MoS_2 samples.

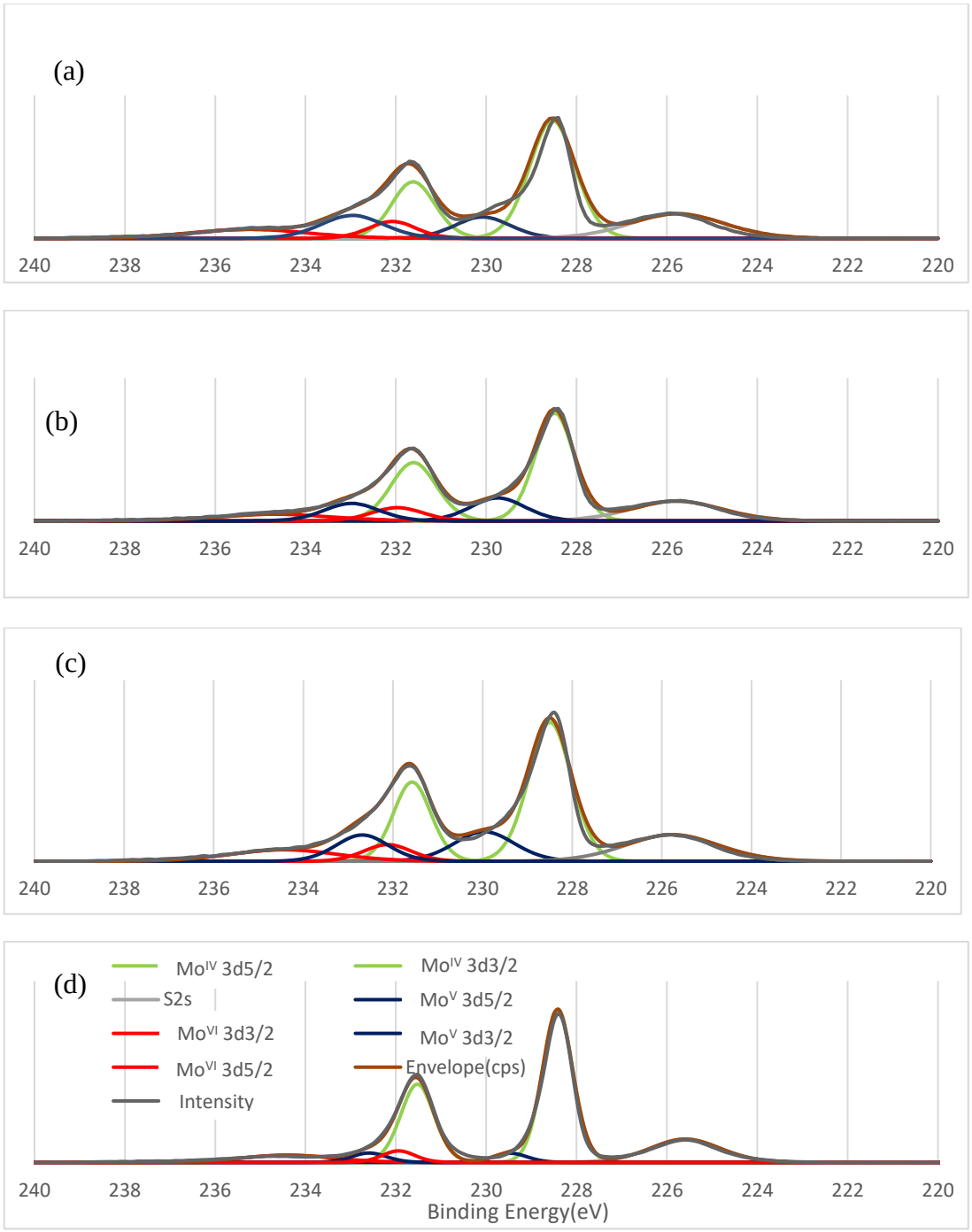

Figure 19 High resolution Mo 3d XPS spectra of (a) MoS_2-1:4-Cu, (b) MoS_2-1:4, (c) fresh MoS_2-1:4, (d) MoS_2-1:2, (e) reused MoS_2-1:4, (f) bulk-MoS_2, (g) CS_2-MoS_2-1:4 and (h) MoS_2-1:7.

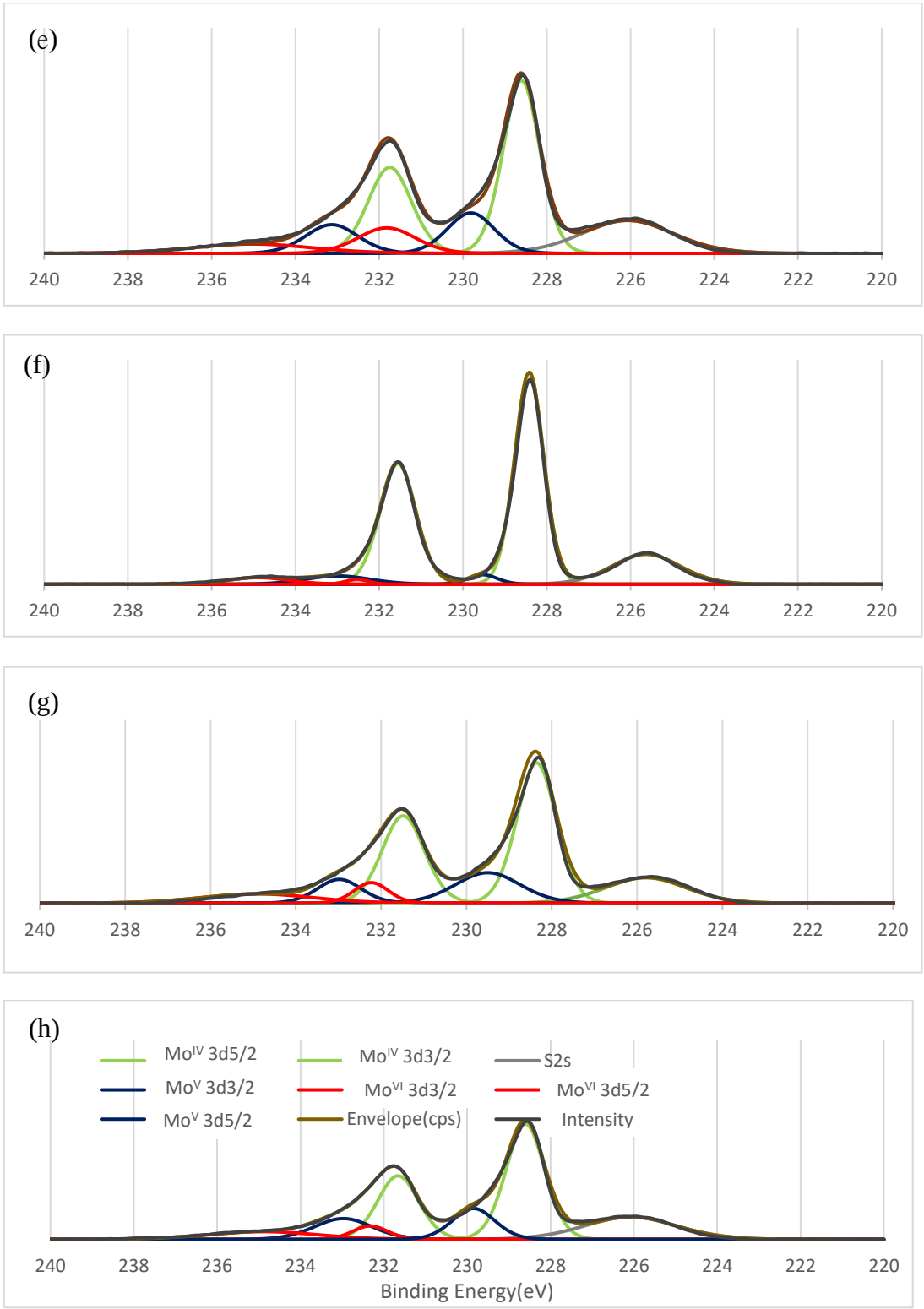

Figure 19 (continued) High resolution Mo 3d XPS spectra of (a) MoS_2-1:4-Cu, (b) MoS_2-1:4, (c) fresh MoS_2-1:4, (d) MoS_2-1:2, (e) reused MoS_2-1:4, (f) bulk-MoS_2, (g) CS_2-MoS_2-1:4 and (h) MoS_2-1:7.

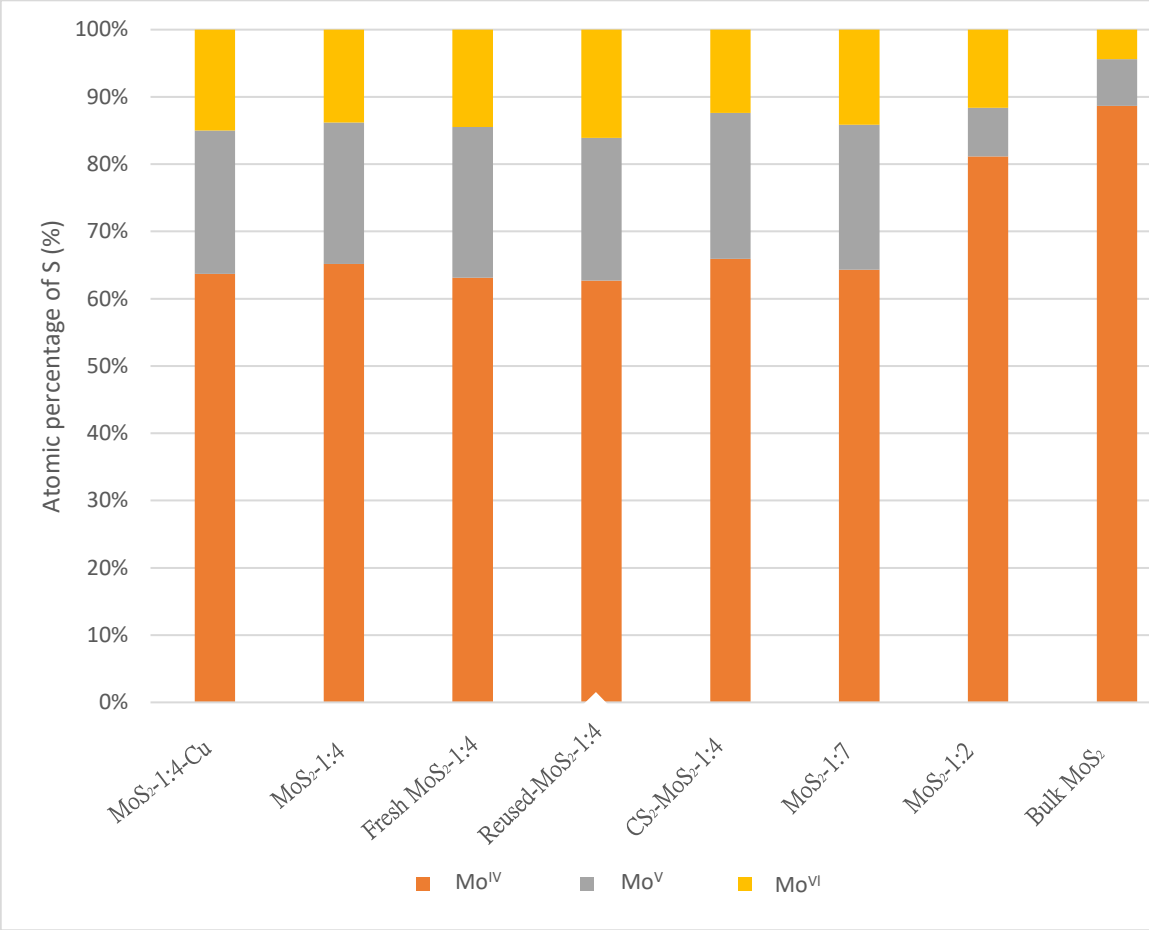

Figure 20 Chemical states of Mo in MoS_2-1:4-Cu, fresh MoS_2-1:4, MoS_2-1:4, MoS_2-1:2, reused MoS_2-1:4, CS_2-MoS_2-1:4, bulk-MoS_2 and MoS_2-1:7.

Table 13 Summary of XPS data on Mo of different MoS_2 samples				
Sample	Peak assignment	Position	FWHM[c]	Atomic concentration (%)
MoS_2-1:4-Cu	Mo^{IV} 3d5/2	228.55	1.18	43.85
	Mo^{IV} 3d3/2	231.60	1.11	19.82
	Mo^{V} 3d5/2	230.06	1.44	9.65
	Mo^{V} 3d3/2	232.94	1.62	11.67
	Mo^{VI} 3d5/2	232.06	1.22	6.50
	Mo^{VI} 3d3/2	235.23	3.02	8.51
MoS_2-1:4[a]	Mo^{IV} 3d5/2	228.46	1.01	40.03
	Mo^{IV} 3d3/2	231.61	1.16	25.12
	Mo^{V} 3d5/2	229.76	1.40	11.92
	Mo^{V} 3d3/2	232.96	1.42	9.13
	Mo^{VI} 3d5/2	231.98	1.33	6.52
	Mo^{VI} 3d3/2	234.72	2.94	7.27
Fresh MoS_2-1:4[b]	Mo^{IV} 3d5/2	228.47	1.11	41.99
	Mo^{IV} 3d3/2	231.58	0.97	21.11
	Mo^{V} 3d5/2	229.97	1.56	12.61
	Mo^{V} 3d3/2	232.70	1.36	9.79
	Mo^{VI} 3d5/2	232.12	1.25	5.68
	Mo^{VI} 3d3/2	234.415	2.80	8.81
MoS_2-1:2	Mo^{IV} 3d5/2	228.40	0.77	51.69
	Mo^{IV} 3d3/2	231.51	0.86	29.46
	Mo^{V} 3d5/2	229.45	0.88	3.51
	Mo^{V} 3d3/2	232.61	0.90	3.71
	Mo^{VI} 3d5/2	231.94	0.84	4.24
	Mo^{VI} 3d3/2	234.43	2.36	7.39
a: Stored for ~30 days b: Freshly prepared c: Full width at half maximum				

Table 13 (continued) Summary of XPS data on Mo of different MoS_2 samples				
Sample	Peak assignment	Position	FWHM[c]	Atomic concentration (%)
Reused MoS_2-1:4	Mo^{IV} 3d5/2	228.58	1.02	39.42
	Mo^{IV} 3d3/2	231.74	1.20	23.27
	Mo^{V} 3d5/2	229.83	1.31	11.87
	Mo^{V} 3d3/2	233.12	1.45	9.35
	Mo^{VI} 3d5/2	231.83	1.60	9.17
	Mo^{VI} 3d3/2	235.03	3.00	6.918
Bulk-MoS_2	Mo^{IV} 3d5/2	228.41	0.80	52.04
	Mo^{IV} 3d3/2	231.58	0.99	36.64
	Mo^{V} 3d5/2	229.53	0.81	2.38
	Mo^{V} 3d3/2	232.96	1.80	4.56
	Mo^{VI} 3d5/2	232.54	0.63	0.93
	Mo^{VI} 3d3/2	234.67	1.70	3.45
CS_2-MoS_2-1:4	Mo^{IV} 3d5/2	228.34	1.07	39.45
	Mo^{IV} 3d3/2	231.50	1.15	26.48
	Mo^{V} 3d5/2	229.51	1.78	14.18
	Mo^{V} 3d3/2	232.99	1.20	7.50
	Mo^{VI} 3d5/2	232.23	0.93	5.05
	Mo^{VI} 3d3/2	234.92	3.02	7.35
MoS_2-1:7	Mo^{IV} 3d5/2	228.58	0.90	37.77
	Mo^{IV} 3d3/2	231.80	1.32	26.52
	Mo^{V} 3d5/2	229.69	1.21	13.23
	Mo^{V} 3d3/2	233.20	1.54	8.32
	Mo^{VI} 3d5/2	231.88	1.62	6.62
	Mo^{VI} 3d3/2	234.90	3.89	7.54
a: Stored for ~30 days b: Freshly prepared c: Full width at half maximum				

4.3.6.2 High resolution S 2p XPS spectra

The deconvoluted XPS S 2p spectra (Figure 21) reveal that the S element in MoS_2 samples consisted of three chemical states: S^{2-}, S_2^{2-} and SO_x^-. The binding energy and assignment of peaks are summarized in Table 14 as follows: S^{2-}2p 1/2 at 162.34 – 163.10 eV, S^{2-} 2p 3/2 at 161.17 - 161.92 eV, S_2^{2-} 2p 1/2 at 162.35 – 163.1 eV, S_2^{2-} 2p 3/2 at 163.300 -164.11 eV and SO_x^- at 168.02 - 168.68 eV.[90, 92, 98-99] The presence of SO_x^- could be attributed to the oxidation of MoS_2 and the reaction residue of hydrothermal synthesis. The atomic concentrations of different S chemical states in each sample are visualized in Figure 22. Except for MoS_2-1:2 and bulk-MoS_2, the S atomic concentrations of the three chemical states in other MoS_2 samples were similar to one another. Compared with the other MoS_2 samples, MoS_2-1:2 and bulk-MoS_2 had higher atomic concentration of S^{2-} and significantly lower atomic concentration of S_2^{2-}. The S_2^{2-} groups are known to be the active sites for hydrogen evolution reaction (HER) which are located at the edges of MoS_2.[90, 92] Similar to the role of S_2^{2-} in HER, the S_2^{2-} groups present in the MoS_2 samples serve as active sites for Cu^{2+} adsorption. Therefore, the low atomic concentration of S_2^{2-} in MoS_2-1:2 and bulk-MoS_2 would lead to a lower adsorption capacity towards Cu^{2+}.

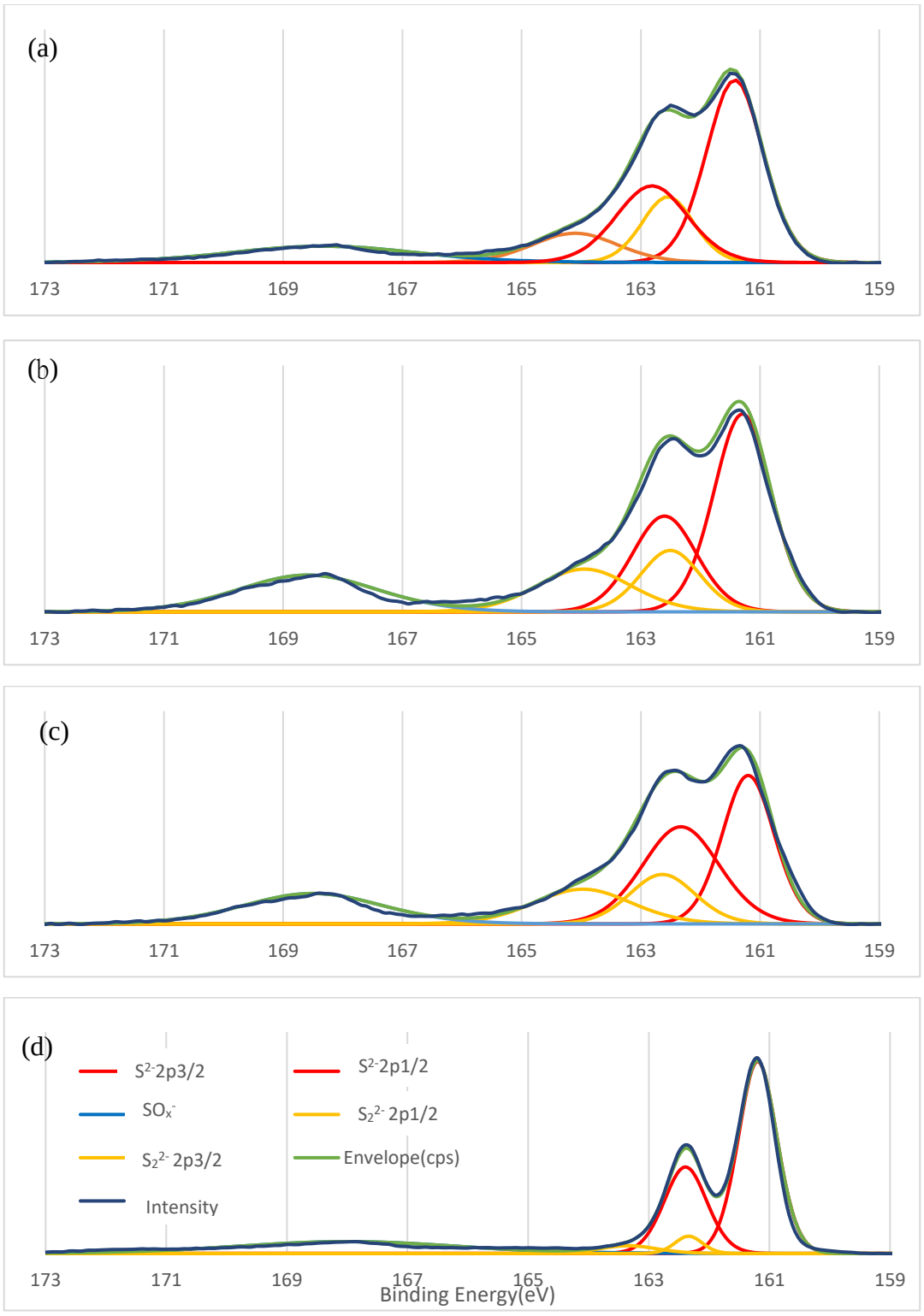

Figure 21 High resolution Mo 3d XPS spectra of (a) MoS_2-1:4-Cu, (b) MoS_2-1:4, (c) fresh MoS_2-1:4, (d) MoS_2-1:2, (e) reused MoS_2-1:4, (f) bulk-MoS_2, (g) CS_2-MoS_2-1:4 and (h) MoS_2-1:7.

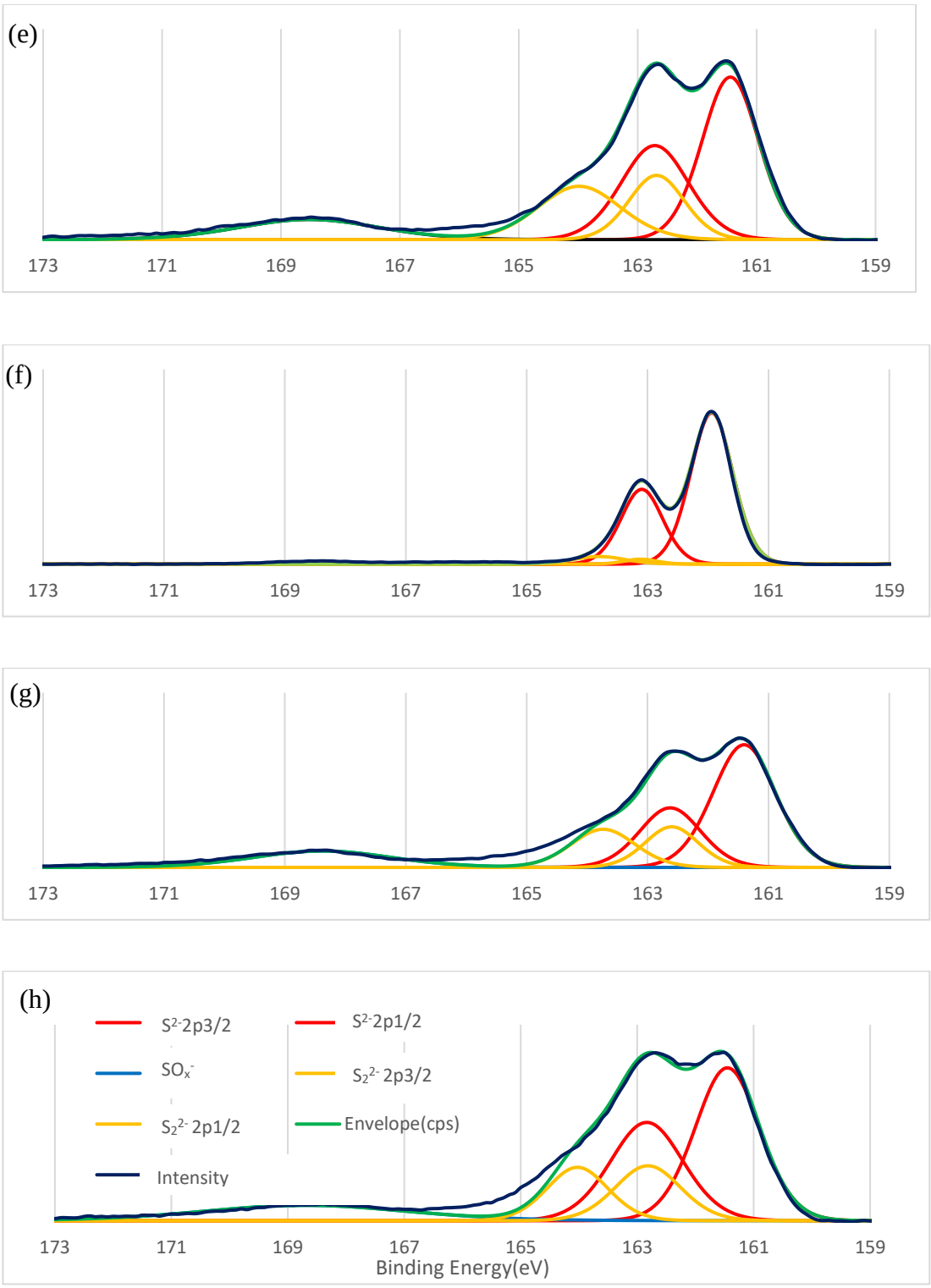

Figure 21 (continued) High resolution Mo 3d XPS spectra of (a) MoS_2-1:4-Cu, (b) MoS_2-1:4, (c) fresh MoS_2-1:4, (d) MoS_2-1:2, (e) reused MoS_2-1:4, (f) bulk-MoS_2, (g) CS_2-MoS_2-1:4 and (h) MoS_2-1:7.

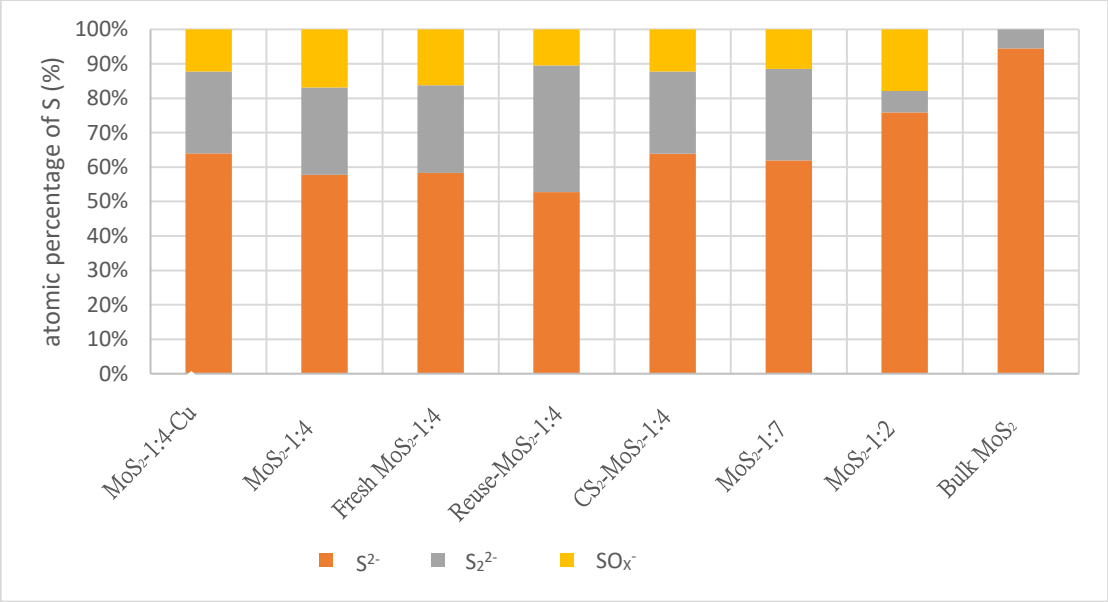

Figure 22 Chemical states of S in MoS_2-1:4-Cu, fresh MoS_2-1:4, MoS_2-1:4, MoS_2-1:2, reused MoS_2-1:4, CS_2-MoS_2-1:4, bulk-MoS_2 and MoS_2-1:7.

Table 14 Summary of XPS data on S of different MoS_2 samples				
Sample	Peak assignment	Position	FWHM[c]	Atomic concentration (%)
MoS_2-1:4-Cu	S^{2-} 2p3/2	161.41	1.11	41.88
	S^{2-} 2p1/2	162.80	1.40	22.13
	S_2^{2-} 2p3/2	164.11	1.66	10.08
	S_2^{2-} 2p1/2	162.55	1.01	13.7
	SO_x^-	168.33	3.62	12.21
MoS_2-1:4[a]	S^{2-} 2p3/2	161.32	1.12	37.45
	S^{2-} 2p1/2	162.60	1.26	20.28
	S_2^{2-} 2p3/2	163.94	1.85	13.28
	S_2^{2-} 2p1/2	162.49	1.17	12.09
	SO_x^-	168.57	2.73	16.9
Fresh MoS_2-1:4[b]	S^{2-} 2p3/2	161.18	1.01	29.66
	S^{2-} 2p1/2	162.34	1.50	28.63
	S_2^{2-} 2p3/2	164.00	1.90	13.01
	S_2^{2-} 2p1/2	162.64	1.28	12.45
	SO_x^-	168.52	2.71	16.25
MoS_2-1:2	S^{2-} 2p3/2	161.17	0.75	50.7
	S^{2-} 2p1/2	162.38	0.82	25.16
	S_2^{2-} 2p3/2	163.30	4.10	4.32
	S_2^{2-} 2p1/2	162.35	0.52	1.96
	SO_x^-	168.02	4.25	17.86
a: Stored for ~30 days b: Freshly prepared c: Full width at half maximum				

Table 14 (continued) Summary of XPS data on S of different MoS_2 samples				
Sample	Peak assignment	Position	FWHM[c]	Atomic concentration (%)
Reused MoS_2-1:4	S^{2-} 2p3/2	161.43	1.11	34.06
	S^{2-} 2p1/2	162.63	1.30	18.65
	S_2^{2-} 2p3/2	163.77	2.24	23.7
	S_2^{2-} 2p1/2	162.73	1.09	13.07
	SO_x^-	168.55	2.75	10.5
Bulk-MoS_2	S^{2-} 2p3/2	161.92	0.81	63.4
	S^{2-} 2p1/2	163.10	0.80	31.09
	S_2^{2-} 2p3/2	163.80	1.00	3.91
	S_2^{2-} 2p1/2	163.10	0.63	1.6
	SO_x^-	--	--	--
CS_2-MoS_2-1:4	S^{2-} 2p3/2	161.41	1.22	41.5
	S^{2-} 2p1/2	162.59	1.18	22.42
	S_2^{2-} 2p3/2	163.80	1.28	13.61
	S_2^{2-} 2p1/2	162.70	1.03	10.21
	SO_x^-	168.40	2.67	12.26
MoS_2-1:2	S^{2-} 2p3/2	161.46	1.29	36.06
	S^{2-} 2p1/2	162.76	1.45	25.86
	S_2^{2-} 2p3/2	164.04	1.38	13.48
	S_2^{2-} 2p1/2	162.82	1.31	13.08
	SO_x^-	168.68	4.11	11.52
a: Stored for ~30 days b: Freshly prepared c: Full width at half maximum				

4.3.6.3 High resolution Cu 2p XPS spectra

The deconvoluted XPS Cu 2p spectra (Figure 23) of MoS_2-1:4-Cu and reused MoS_2-1:4 reveal the presence of two kinds of chemical states of Cu (Cu^{2+} and Cu^{+}) on the surface of MoS_2. The binding energy and assignment of peaks are summarized in Table 15 as follows: one strong peak at binding energy of 932.22 – 932.30 eV corresponded to Cu^{+}/Cu^{2+} 2p3/2 in copper sulfide, [95, 100-102] while one weak peak at 933.70 – 934.38 eV was attributed to Cu^{2+} 2p3/2 in Cu^{2+} salts such as $CuSO_4$ and $Cu(NO_3)_2$.[103-104] The satellite peak at 939.70 eV was observed in the reused MoS_2-1:4, indicating that the paramagnetic state of Cu^{2+} existed in the reused MoS_2-1:4.

A reduction of the adsorbed Cu^{2+} to Cu^{+} or Cu was proposed in the Cu^{2+} adsorption on thiolpropy-functionalized MCM-41, based on the XPS results.[105] Thiols groups (RSH) undergo complex reaction with Cu^{2+} as displayed in the following reactions[106]:

$$Cu^{2+} + RSH \rightarrow Cu^{2+} - SR + H^{+}$$

$$Cu^{2+} - SR \rightarrow Cu^{+} + {}^{\cdot}SR$$

$$Cu^{+} + RSH \rightarrow Cu^{+} - SR + H^{+}$$

$$2\,{}^{\cdot}SR \rightarrow RSSR$$

$$Cu^{+} - SR + O_2 \rightarrow Cu^{2+} - SR + {}^{\cdot}O_2^{-}$$

Similar reactions might occur between the adsorbed Cu^{2+} and MoS_2-1:4. The reduction of Cu^{2+} to Cu^{+} would increase the adsorption affinity and capacity of MoS_2 towards copper. Cu^{+} was classified as a soft ion in HSAB theory, which had a stronger

affinity than Cu^{2+} towards MoS_2 materials. Additionally, the superoxide $\cdot O_2^-$ was formed from the reaction between Cu^+ and oxygen, which would further facilitate MoS_2 oxidation. This indicates that the MoS_2 may be oxidized faster in Cu^{2+} solutions.

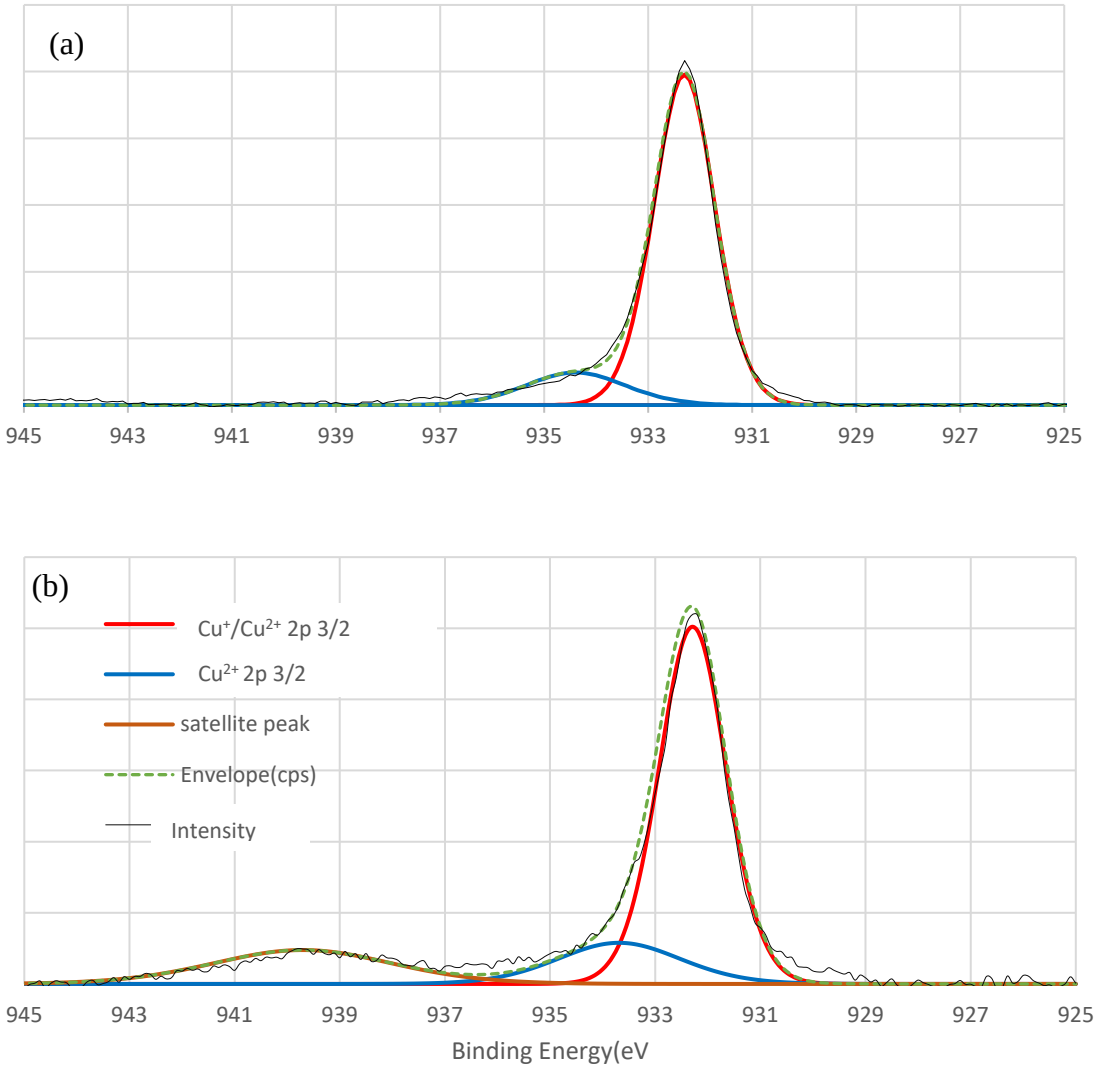

Figure 23 High resolution XPS spectra of Cu 2p for (a) MoS_2-1:4-Cu and (b) reused MoS_2-1:4

Table 15 Summary of XPS data on Cu of different MoS_2 samples				
Sample	Peak assignment	Position	FWHM[a]	Atomic concentration (%)
MoS_2-1:4-Cu	Cu^+/ Cu^{2+} 2p3/2	932.22	1.370	86.18
	Cu^{2+} 2p3/2	934.38	2.228	13.83
Reused MoS_2-1:4	Cu^+/ Cu^{2+} 2p3/2	932.30	1.488	68.33
	Cu^{2+} 2p3/2	933.70	2.734	14.43
	satellite	939.70	3.976	17.26
a: Full width at half maximum				

4.3.7 Dissolution test (pH and time)

The monolayered MoS_2 would undergo oxidization in air at room temperature and atmospheric pressure. This oxidation process was accelerated by moisture in the air and the oxidation usually began at the grain boundaries and edge sites. It was reported that about 34.8% of Mo in the monolayered MoS_2 was oxidized in the presence of moisture after one year.[107] The aqueous stability of the MoS_2 nanosheet was even lower than its air stability. The MoS_2 nanosheets would be oxidized by dissolved oxygen in aqueous solutions. The oxidization rate was higher in alkaline conditions and in the thinner MoS_2 nanosheet. Almost half of the Mo in MoS_2 nanosheet was oxidized after 100 days in air-saturated water.[84]

Figure 24 shows the weight loss of MoS_2-1:7 after being suspended in DDI water and adsorbing Cu^{2+}. The weight loss of MoS_2-1:7 in aqueous solutions should be attributed to the oxidation of MoS_2. The dissolution test revealed that 6% of Mo and 5.81% of S in MoS_2-1:7 were released as soluble species to water after contacted for 5 days, while 12.59 % of Mo and 9.74 % of S dissolved as soluble species during the Cu^{2+} adsorption. The Cu^{2+} adsorbed on MoS_2-1:7 would show catalytic effect on the oxidation of MoS_2-1:7, so the soluble species released during Cu^{2+} adsorption were almost two times more than MoS_2-1:7 suspended in water. The Cu^{2+}-induced oxidation could be minimized by removing Cu^{2+} once the adsorption equilibrium was reached.

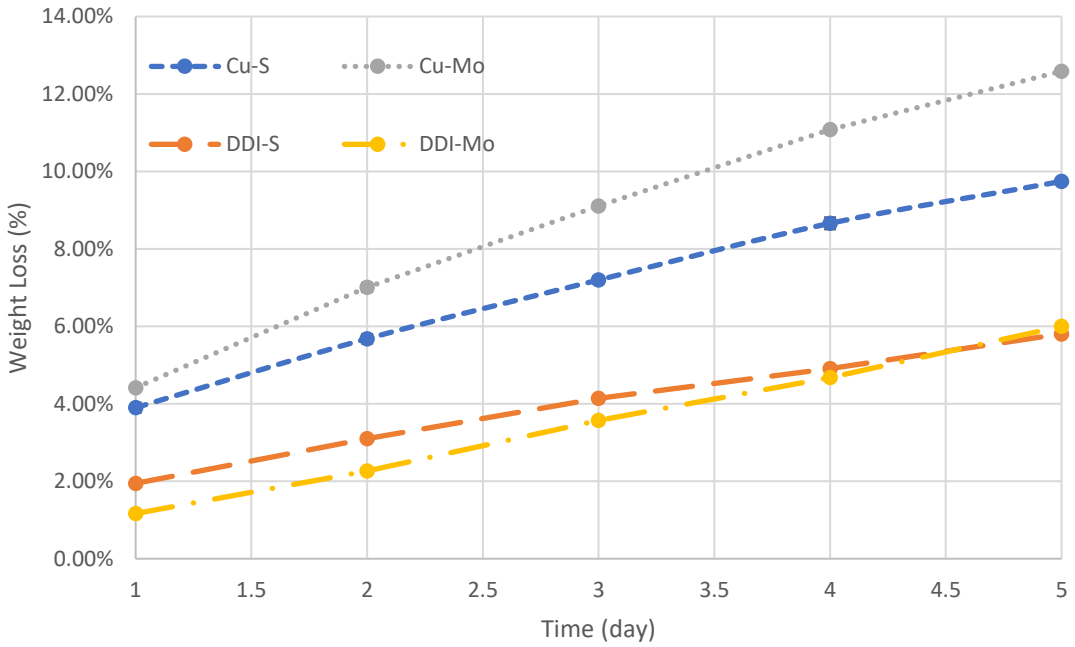

Figure 24 Dissolution of MoS_2-1:7 in DDI water and during Cu^{2+} adsorption. Cu-S and Cu-Mo represent the weigh loss of MoS_2 as S and Mo during the Cu^{2+} adsorption study, respectively. DDI-S and DDI-Mo represent the weight loss of MoS_2 as S and Mo after suspending in DDI water, respectively

4.4 Adsorption parameter of MoS_2

4.4.1 Effect of pH

The effect of pH on the amount of Cu^{2+} adsorbed on MoS_2-1:4 and MoS_2-1:7 was determined with 1 mM Cu^{2+} solution and 0.5 g/L of adsorbent dosage. The optimal pH range for Cu^{2+} removal was found to be 4 - 6 (Figure 25) and the Cu^{2+} adsorption capacities of MoS_2-1:4 and MoS_2-1:7 at optimal pH were 126.3 and 130.6 mg/g, respectively. However, it should be noted that the pH value became lower after Cu^{2+} adsorption. This was attributed to the acid production via oxidation of MoS_2. The adsorption capacities of MoS_2-1:4 and MoS_2-1:7 dropped to 34.6 and 17.1 mg/g respectively, when pH was 1.5, indicating that the adsorbent could be regenerated by acid treatment. The Cu^{2+} precipitation of $Cu(OH)_2$ occurred at pH >7.

To study the interaction between Cu^{2+} and the adsorbent surface, the zeta potentials of the adsorbent at different pH values were measured in 1 mM KCl solution. The effect of pH on the zeta potential of MoS_2-1:4 is shown in Figure 26. It indicates that the surface charge of MoS_2-1:4 exhibited negative charge when pH > 3. However, the surface charge of MoS_2-1:4 was positive at acidic pH < 3. The trend of zeta potential was similar to the studies reported in the literature.[19, 108] Therefore, the high Cu^{2+} adsorption capacity of MoS_2-1:4 at pH 4 - 6 was attributed to the coulombic attraction between the negatively-charged MoS_2 and positively-charged Cu^{2+}.

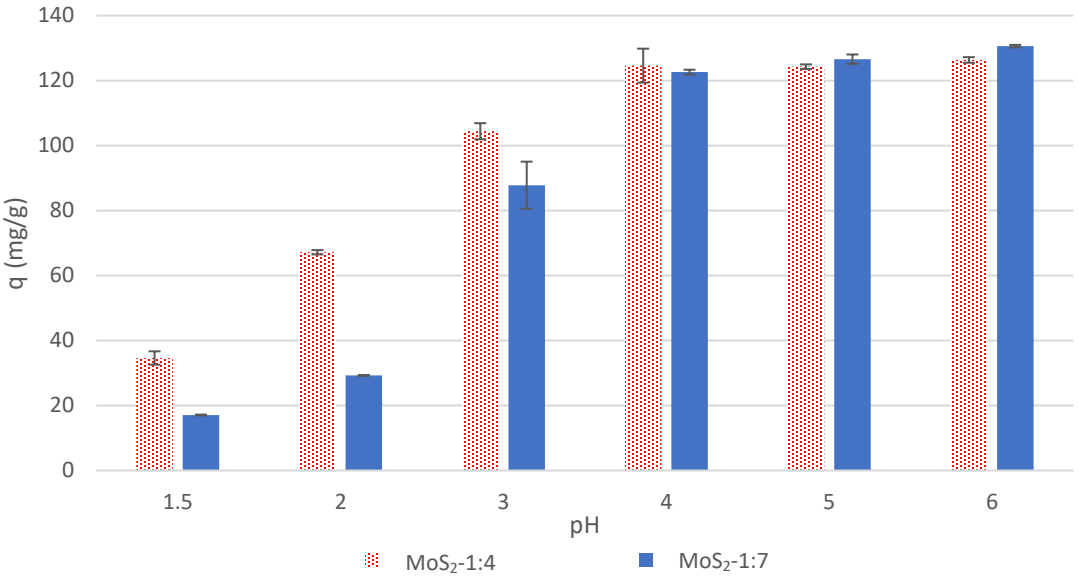

Figure 25 Cu^{2+} adsorption capacities of MoS_2-1:4 and MoS_2-1:7 at different pH. [Initial Cu^{2+} concentration 1 mM, dose 0.5 g/L, 250 rpm, 298 K, 24 hours.]

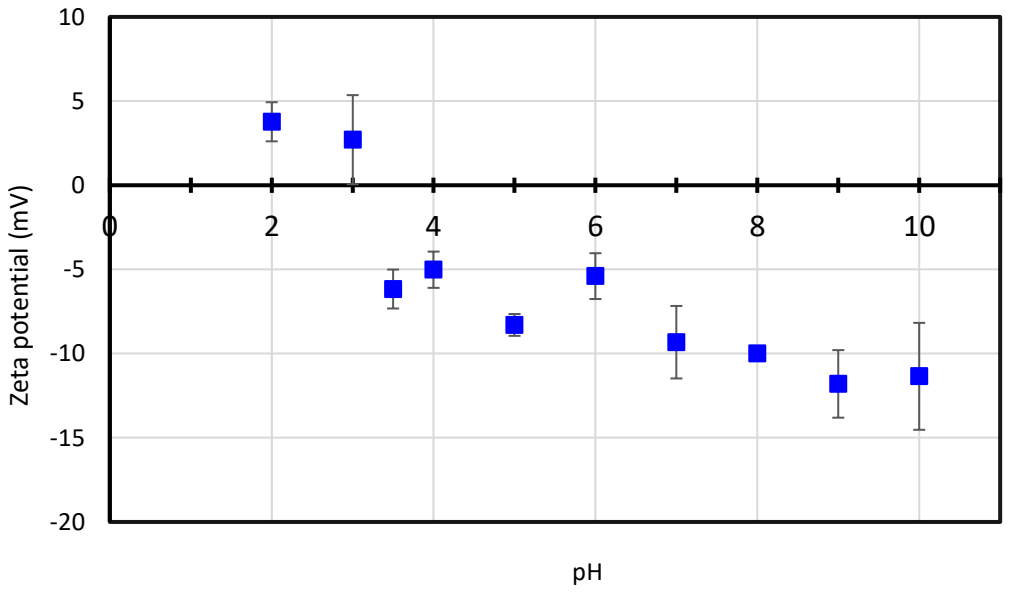

Figure 26 Zeta potential of MoS_2-1:4 at different pH.

4.4.2 Kinetic study

The Cu^{2+} adsorption kinetics of MoS_2-NN-MCF, MoS_2-1:4 and MoS_2-1:7 were determined under the following conditions: 0.5 g/L of the adsorbent was added to 1 mM of Cu^{2+}solution, and the mixture was agitated continuously for five to 1440 minutes (250 rpm) at pH 4 – 5 and 25 ^{o}C. As shown in Figure 27, the adsorption rate was very fast in the initial period (0 to 120 min) and reached 80% of the equilibrium adsorption capacity in the first 120 minutes. The equilibrium time for the Cu^{2+} adsorption on MoS_2-1:4 and MoS_2-1:7 at pH 5.0 was about 180 minutes, whereas that of MoS_2-1:4 and MoS_2-NN-MCF at pH 4.0 were 240 and 480 minutes, respectively. Except MoS_2-NN-MCF, ~99 % of the Cu^{2+} removal was achieved by MoS_2-1:4 and MoS_2-1:7, indicating the high affinity of MoS_2 towards Cu^{2+}. The adsorption of Cu^{2+} on MoS_2-1:4 at pH 5.0 was slightly faster than that at pH 4.0. Since MoS_2 became more negatively charged as the pH increased, the stronger coulombic force would enhance the adsorption rate of Cu^{2+}. The equilibrium adsorption capacities of MoS_2-1:4 and MoS_2-1:7 at different pH were about 130 mg/g, while that of MoS_2-NN-MCF was about 70 mg/g.

Pseudo-first-order, pseudo-second-order, Elovich and intra-particle diffusion kinetic models were used to simulate the Cu^{2+} adsorption kinetics of MoS_2-NN-MCF, MoS_2-1:4 and MoS_2-1:7. Figures 28 – 35 display the linear and non-linear modeling curves for the different MoS_2-based materials and the kinetic constants are summarized in Tables 16 – 17. The time points after reaching the adsorption equilibrium were ignored in the model simulation.[109]

In general, the nonlinear Elovich kinetic model was the best-fit model for simulating the adsorption kinetics of Cu^{2+} on MoS_2-1:4 and MoS_2-1:7 with the highest r^2 values (0.9917 – 0.9975) and the lowest RMSE values (2.33 – 5.15) as compared with other kinetic models. The nonlinear pseudo-second-order and linear and non-linear Elovich kinetics of Cu^{2+} on MoS_2-NN-MCF showed the highest r^2 values (0.9882 –0.9956) and the lowest RMSE values (2.0 –-2.15). The good fitting of the Elovich model suggested that the adsorption process was a chemisorption of the adsorbate onto the adsorbent with a heterogeneous surface.[110]

Table 16 Summary of kinetic parameters on Cu^{2+} adsorption by MoS_2-1:7 and MoS_2-NN-MCF

		MoS_2-NN-MCF pH 4		MoS_2-1:7 pH 5	
Model	Parameter	Linear	Nonlinear	Linear	Nonlinear
Pseudo-first-order kinetic	q_e (mg/g)	46.8014 ± 2.1421	68.3494 ± 1.9465	128.3158 ± 4.0397	131.3415 ± 6.6376
	k(min^{-1})	0.0080 ± 0.0008	0.0255 ± 0.0032	0.0264 ± 0.0014	0.0373 ± 0.0069
	r^2	0.9548 ± 0.02550	0.9679 ± 0.0095	0.9936 ± 0.0011	0.9605 ± 0.0070
	RMSE	27.4502 ± 2.2518	4.9973 ± 0.6350	15.0430 ± 3.4914	9.8609 ± 0.8486
Pseudo-second-order kinetic	q_e (mg/g)	75.5426 ± 0.1790	70.6425 ± 1.7392	146.5121 ± 0.3585	124.0957 ± 2.5232
	k (g/mg-min)	0.000500 ± 0.000003	0.0007 ± 0.0001	0.000500 ± 0.000002	0.0008 ± 0.0001
	r^2	0.9849 ± 0.0016	**0.9956 ± 0.0035**	0.9927 ± 0.0002	0.9135 ± 0.0267
	RMSE	2.3033 ± 0.4124	**2.1376 ± 0.1927**	9.0982 ± 0.3534	8.6594 ± 0.1516
Elovich kinetic	α (g/mg-min^2)	13.1073 ± 0.2292	7.3872 ± 1.3316	28.8341 ± 0.5749	14.4283 ± 2.7003
	β (mg/g-min)	0.0506 ± 0.0050	0.0735 ± 0.0039	0.0247 ± 0.0023	0.0310 ± 0.0023
	r^2	**0.9882 ± 0.0048**	**0.9899 ± 0.0041**	0.9851 ± 0.0008	**0.9917 ± 0.0019**
	RMSE	**2.0042 ± 0.4613**	**2.1517 ± 0.5501**	5.3736 ± 0.4969	**5.1471 ± 0.5004**
Intra-particle diffusion	k (mg/g-√min)	4.0815 ± 0.0022	4.0814 ± 0.2900	12.2000 ± 0.0127	12.2002 ± 0.6796
	r^2	0.7081 ± 0.0001	0.7081 ± 0.0001	0.9031 ± 0.0047	0.9031 ± 0.0047
	RMSE	13.1606 ± 0.14400	13.1606 ± 0.1440	15.1973 ± 0.2529	15.1973 ± 0.2529

Table 17 Summary of kinetic parameters on Cu^{2+} adsorption by MoS_2-1:4					
		MoS_2-1:4 pH 5		MoS_2-1:4 pH 4	
Model	Parameter	Linear	Nonlinear	Linear	Nonlinear
Pseudo-first-order kinetic	q_e (mg/g)	97.63 ± 6.03	126.94 ± 5.45	88.68 ± 1.07	120.71 ± 6.49
	k(min^{-1})	0.029 ± 0.002	0.0813 ± 0.0163	0.0177 ± 0.002	0.0611 ± 0.015
	r^2	0.9758 ± 0.018	0.9525 ± 0.0023	0.9730 ± 0.005	0.9070 ± 0.0265
	RMSE	42.54 ± 4.97	11.12 ± 0.019	47.45 ± 0.58	15.05 ± 1.61
Pseudo-second-order kinetic	q_e (mg/g)	140.38 ± 0.15	131.80 ± 2.00	136.57 ± 1.46	118.22 ± 4.99
	k (g/mg-min)	0.0010 ± 0.0001	0.0012 ± 0.0001	0.0006 ± 0.0001	0.0015 ± 0.0002
	r^2	0.9964 ± 0.0006	0.9676 ± 0.006	0.9948 ± 0.0018	0.8280 ± 0.0658
	RMSE	6.01 ± 0.30	7.11 ± 0.24	8.90 ± 1.54	11.38 ± 1.53
Elovich kinetic	α (g/mg-min^2)	0.0075 ± 0.024	0.0441 ± 0.0012	0.1286 ± 0.0016	0.0471 ± 0.00274
	β (mg/g-min)	26.06 ± 0.06	64.34 ± 10.62	20.77 ± 0.84	49.41 ± 11.54
	r^2	0.9810 ± 0.006	**0.9975 ± 0.0005**	**0.9810 ± 0.0046**	**0.9932 ± 0.0025**
	RMSE	9.51 ± 5.55	**2.33 ± 0.29**	**3.65 ± 0.63**	**4.18 ± 0.60**
Intra-particle diffusion	k (mg/g-√min)	12.88 ± 0.17	12.89 ± 1.19	10.71 ± 0.25	10.71 ± 0.91
	r^2	0.6733 ± 0.0359	0.6768 ± 0.0301	0.6661 ± 0.0092	0.6661 ± 0.0092
	RMSE	26.53 ± 1.46	26.5 ± 1.45	24.84 ± 1.05	24.83 ± 1.05

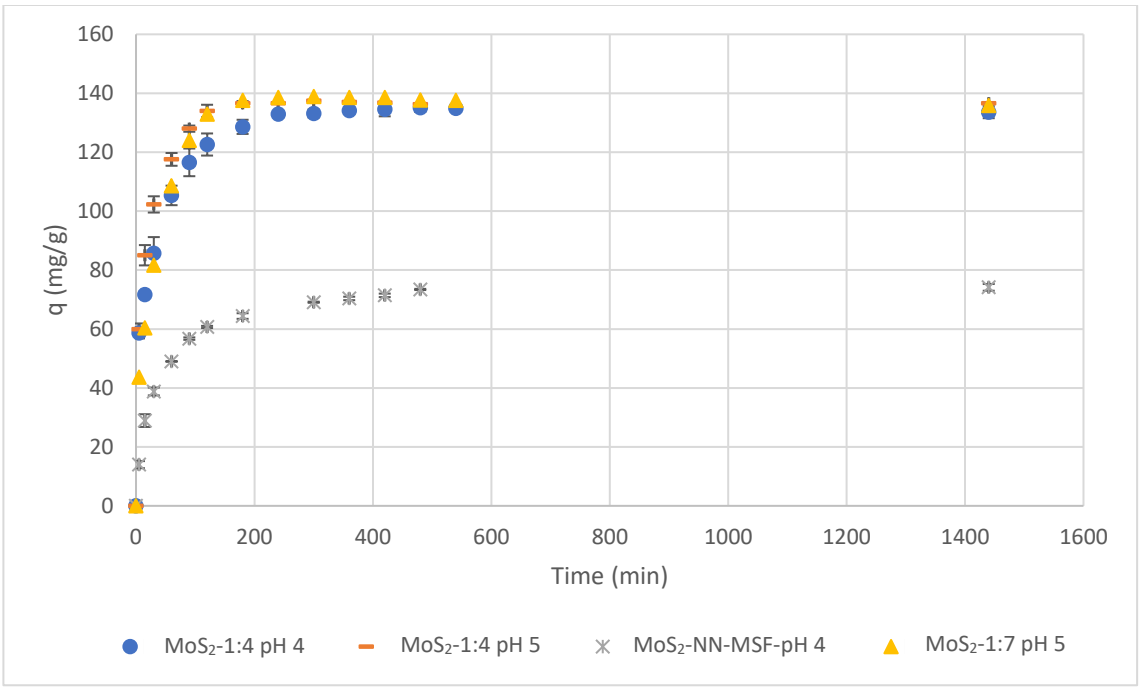

Figure 27 Effect of time on Cu^{2+} adsorption by MoS_2 based materials.

[Initial Cu^{2+} concentration 1 mM, dose 0.5 g/L, 250 rpm, 298 K]

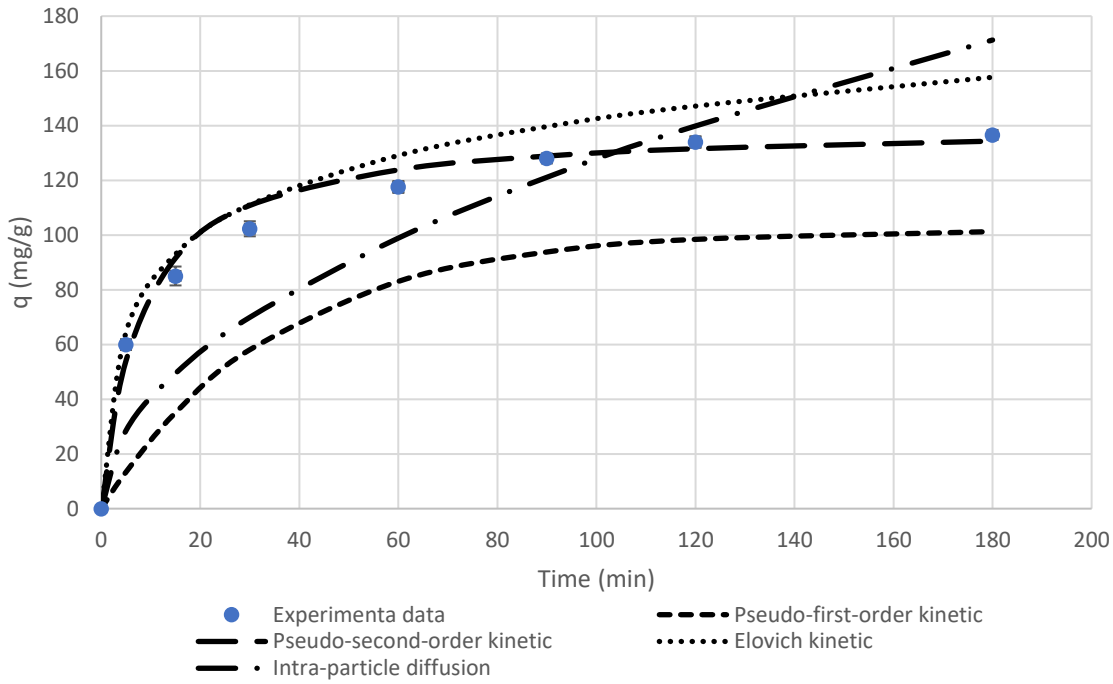

Figure 28 Linear modeling curves for Cu^{2+} adsorption by MoS_2-1:4 at pH 5.

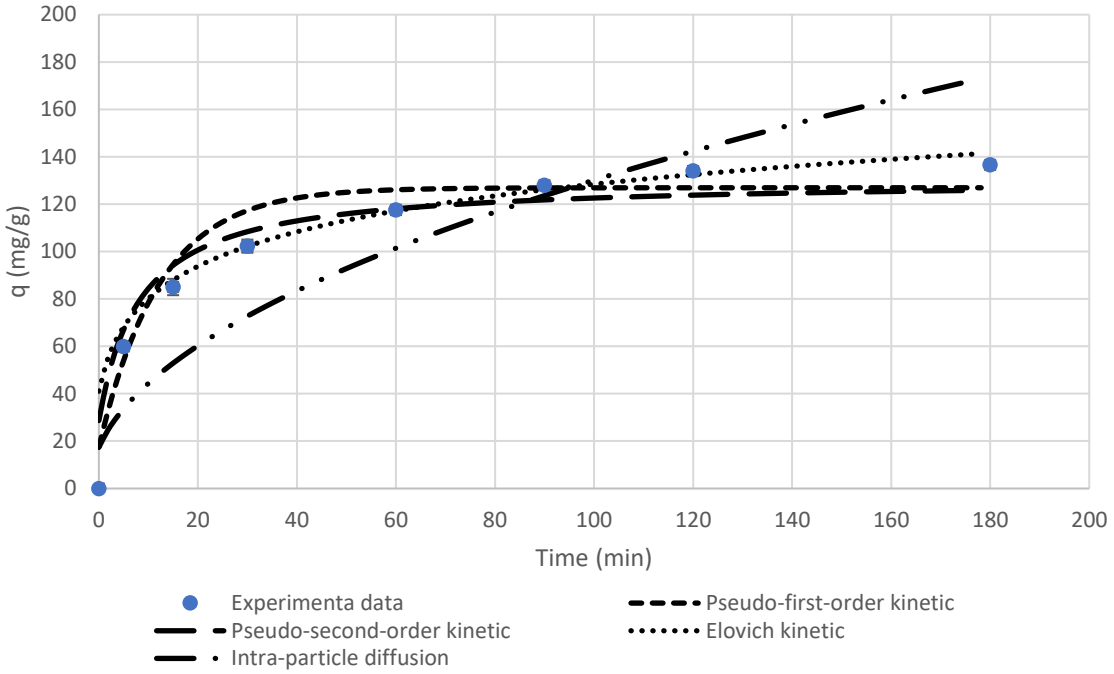

Figure 29 Nonlinear modeling curves for Cu^{2+} adsorption by MoS_2-1:4 at pH 5.

”

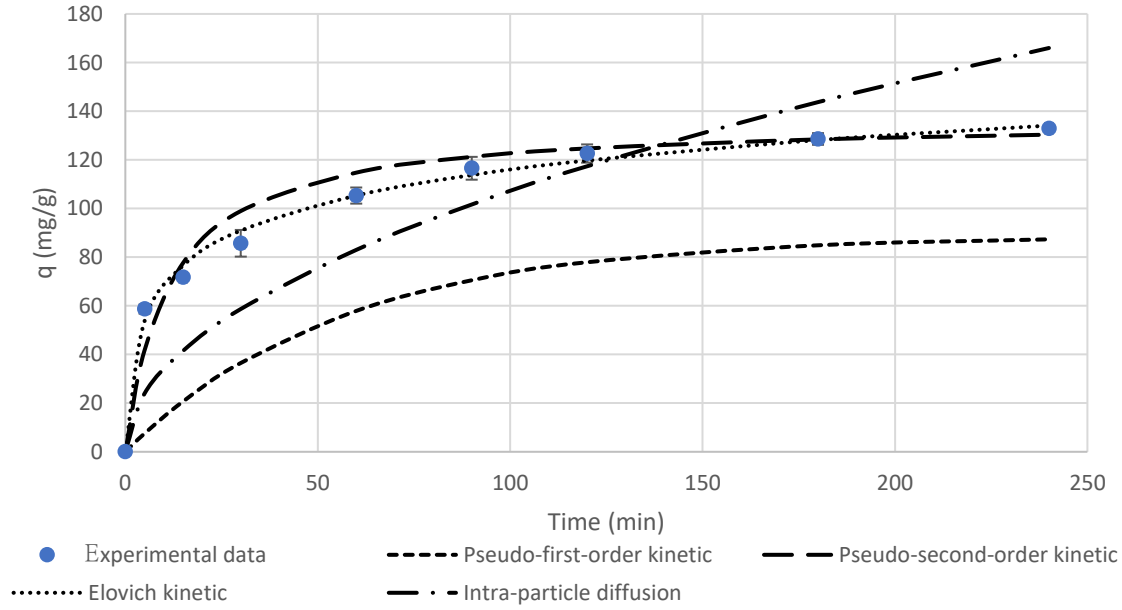

Figure 30 Linear modeling curves for Cu^{2+} adsorption by MoS_2-1:4 at pH 4.

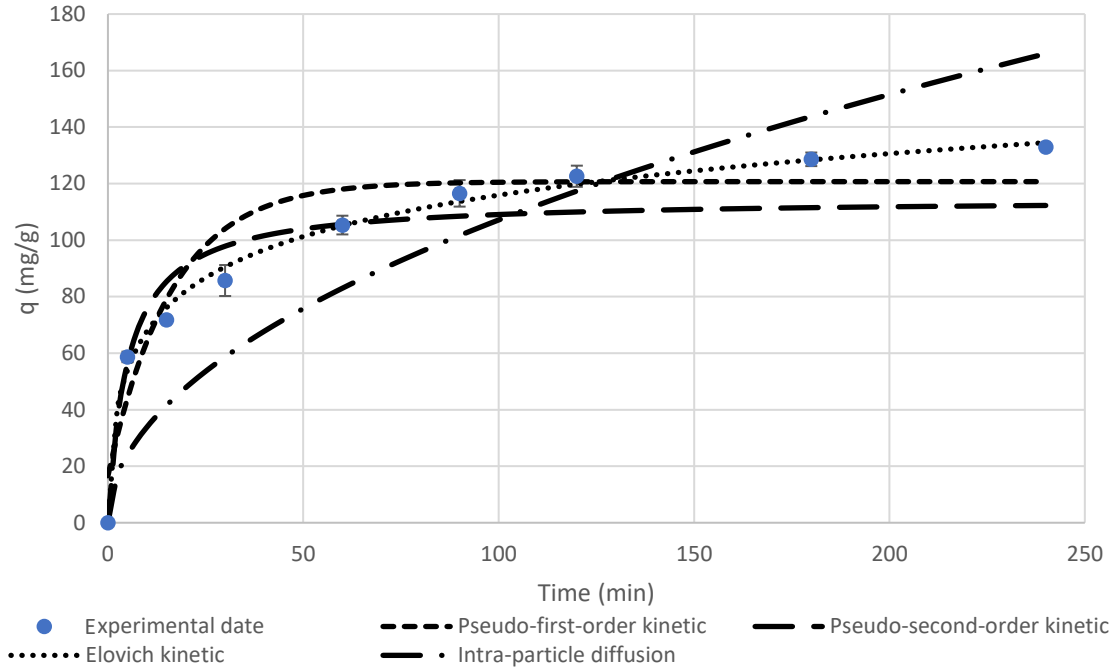

Figure 31 Nonlinear modeling curves for Cu^{2+} adsorption by MoS_2-1:4 at pH 4.

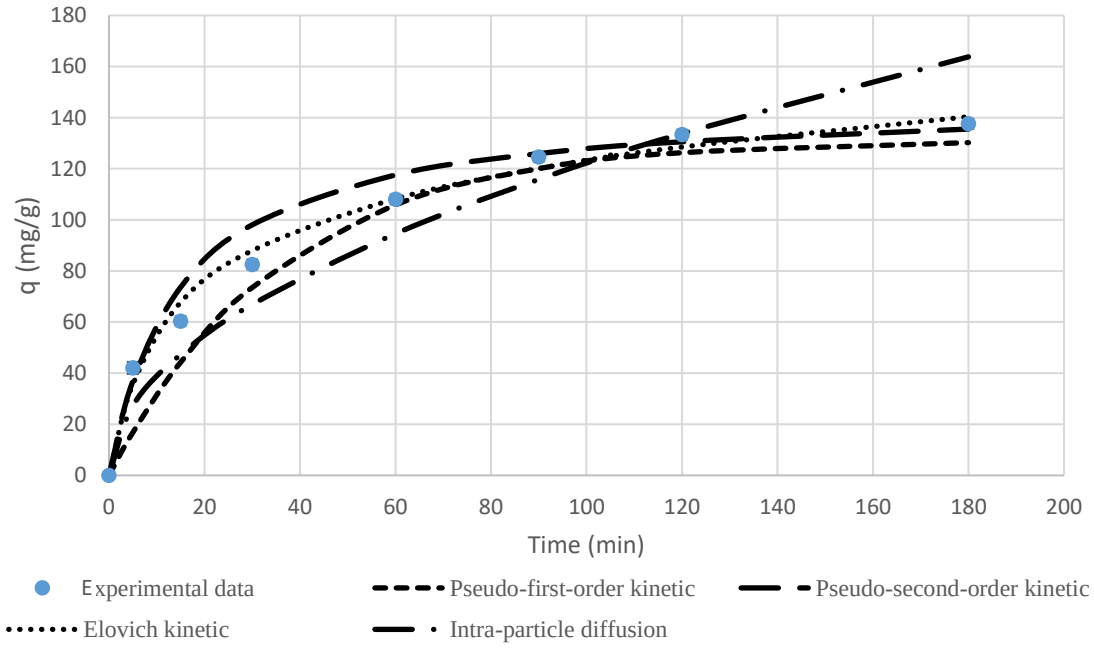

Figure 32 Linear modeling curves for Cu^{2+} adsorption by MoS_2-1:7 at pH 5.

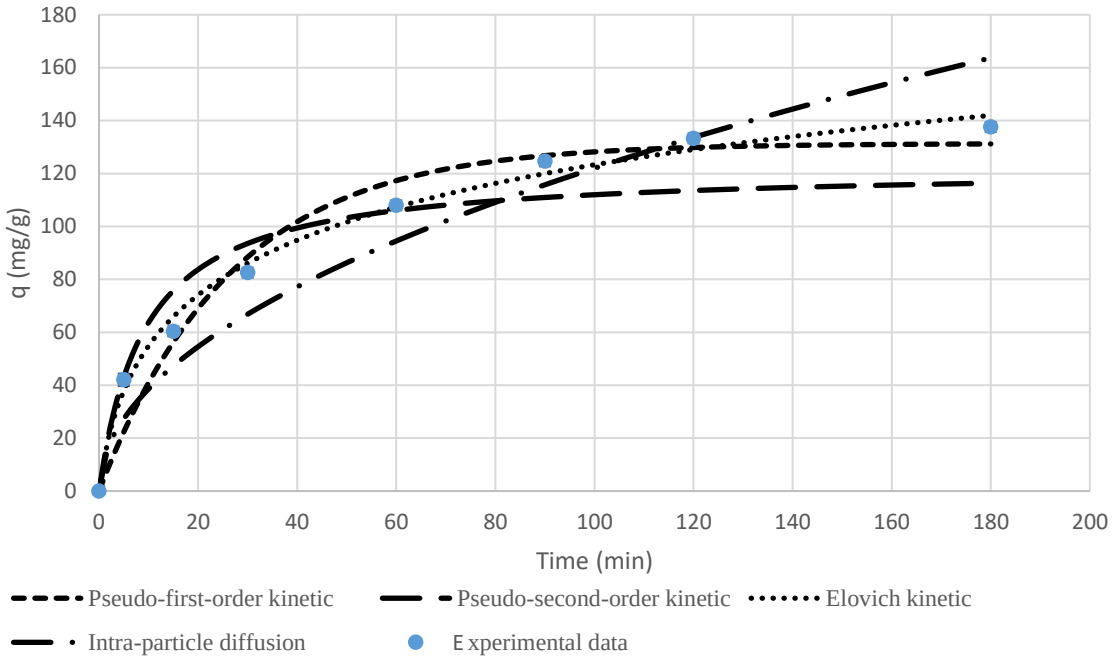

Figure 33 Nonlinear modeling curves for Cu^{2+} adsorption by MoS_2-1:7 at pH 5.

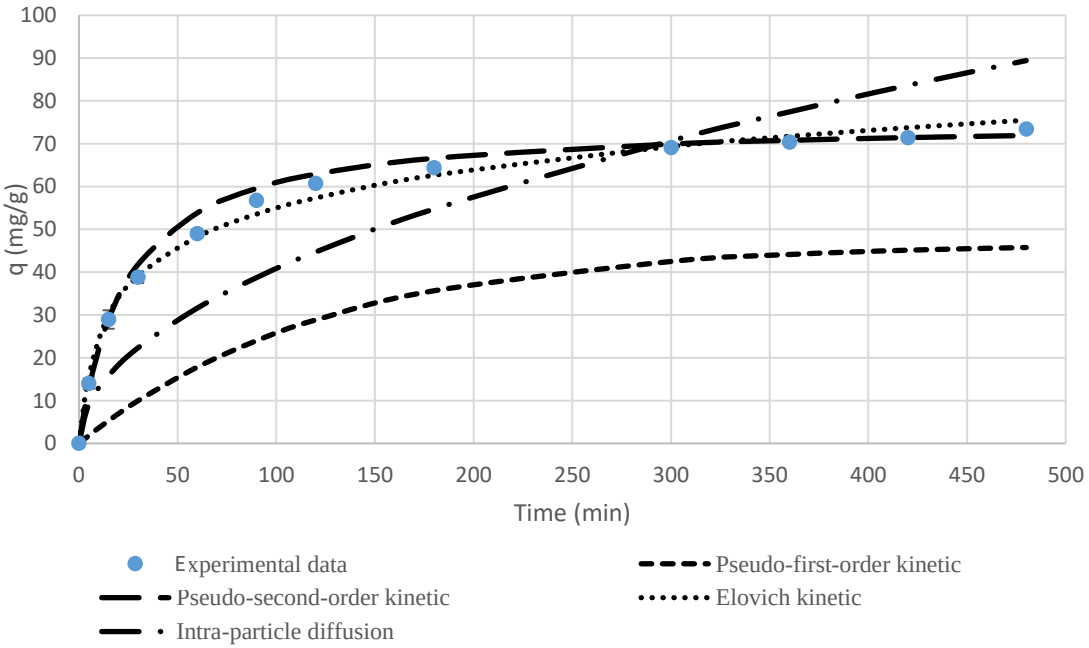

Figure 34 Linear modeling curves for Cu^{2+} adsorption by MoS_2-NN-MS at pH 4.

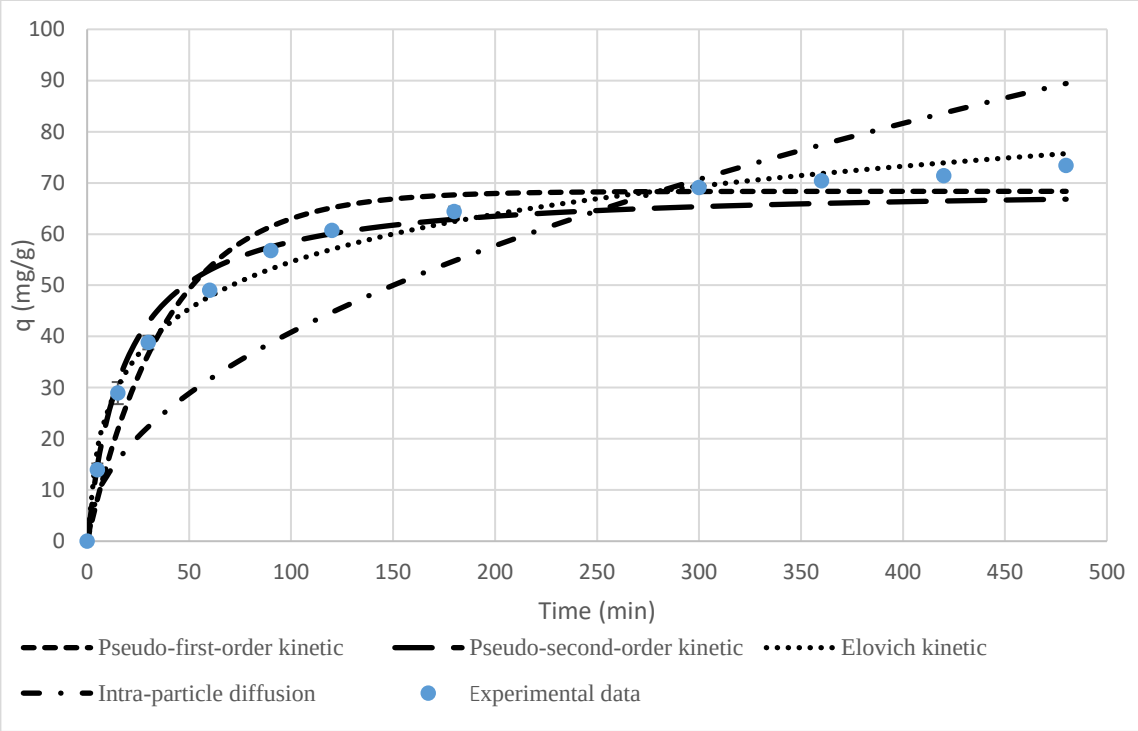

Figure 35 Nonlinear modeling curves for Cu^{2+} adsorption by MoS_2-NN-MCF at pH 4.

4.4.3 Adsorption isotherm

To investigate the effect of the initial concertation of Cu^{2+} on the adsorption capacities of MoS_2-1:4 and MoS_2-1:7, batch adsorption experiments were carried out with varying initial Cu^{2+} concentrations from 0.4 to 4 mM. Various isotherm models, including Langmuir, Freundlich, Temkin, Dubinin-Radushkevich (DR) and Sips isotherm models were used to simulate the adsorption isotherm data of MoS_2-1:4 and MoS_2-1:7. The linear and non-linear modeling curves are shown in Figures 36 – 39 , and the modeling parameters are listed in Tables 18 and 19. The Cu^{2+} adsorption capacities of both adsorbents increased sharply with an increase of Cu^{2+} equilibrium concentration until their adsorption capacities approached the maximum adsorption capacities.

For MoS_2-1:4, the non-linear DR and Sips isotherms were found to be the best-fit isotherm with the highest r^2 value of ~ 0.96 and the lowest RMSE value of ~17. For MoS_2-1:7, the best-fitted model is the non-linear Sips isotherm because of its highest r^2 of 0.969 and minimum RMSE of ~12.6. The good fitting of non-linear DR isotherm suggested high solute activities in the Cu^{2+} adsorption. Additionally, the Sips isotherm is a combination of Langmuir and Freundlich isotherms, and it can be reduced to Langmuir isotherm when the constant m is equal to 1.0. In the case of Cu^{2+} adsorption on MoS_2-1:4 and MoS_2-1:7, the constant m was 0.72 and 2.0 respectively, which deviated from 1.0, indicating that the Sips isotherm could not be reduced to Langmuir isotherm.

The adsorption capacities of MoS_2-1:7 and MoS_2-1:4 calculated from the Sips isotherm were 201.35 and 226.20 mg/g respectively, which were higher than those of

KMS-1[8] ,ion-exchange resin[111-113], grafted silica[114] , chitosan-based materials[115-116] and carbon-based materials[117-119].

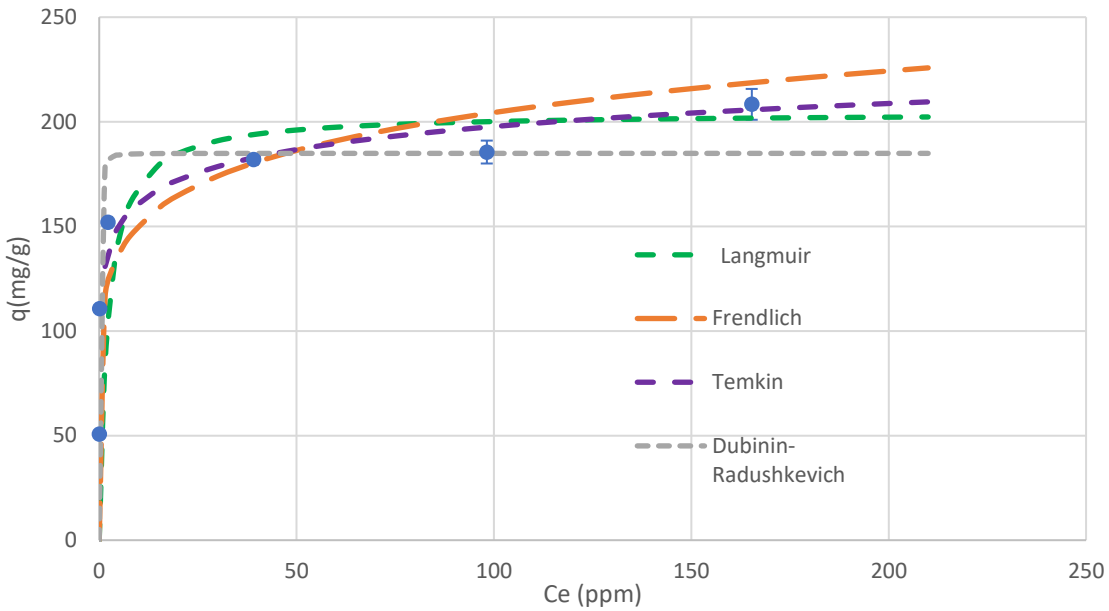

Figure 36 Linear isothem modeling curves of MoS_2-1:7 at pH 5.

[Initial Cu^{2+}concentrations 0.4 – 4.0 mM, dose 0.5 g/L, 250 rpm, 298 K]

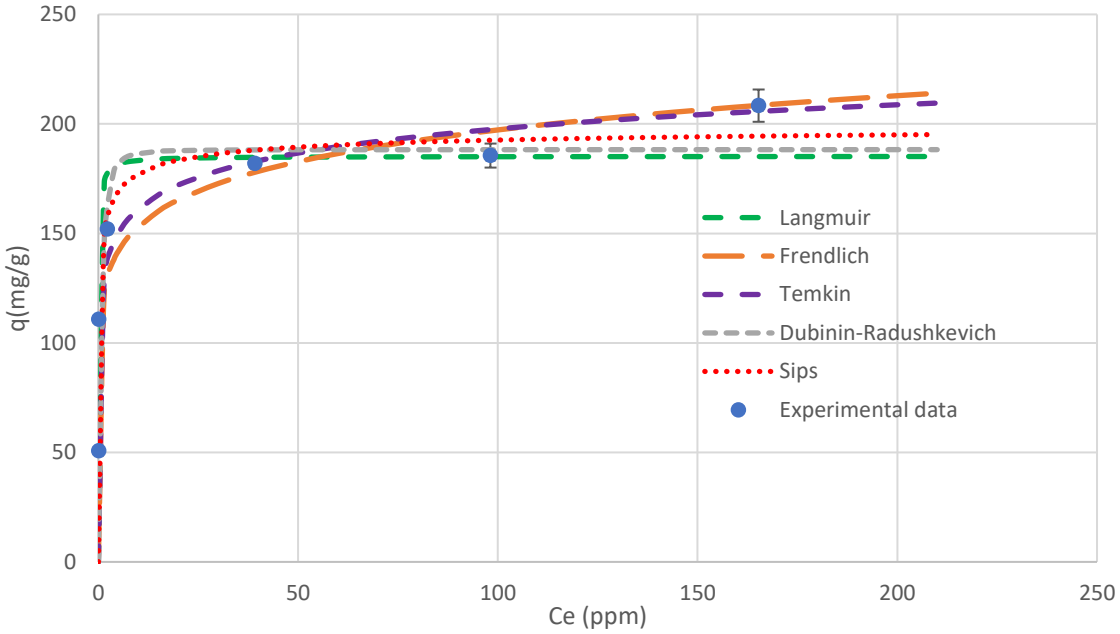

Figure 37 Non-linear isothem modeling curves of MoS_2-1:7 at pH 5.

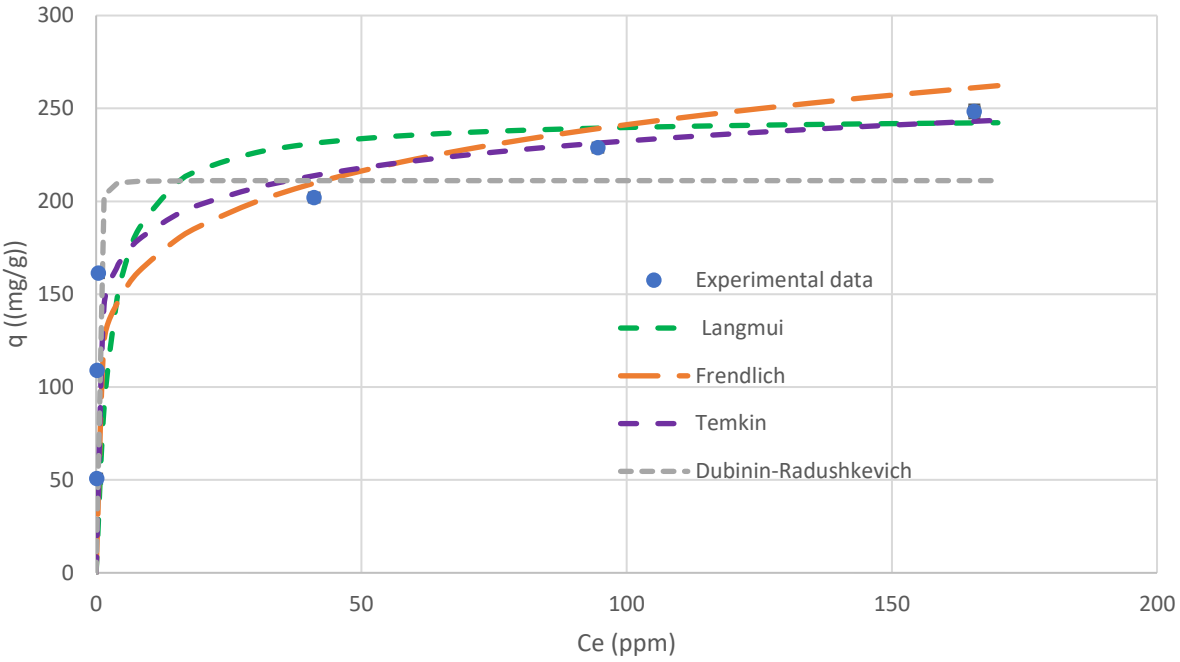

Figure 38 Linear isothem modeling curves of MoS_2-1:4 at pH 5.

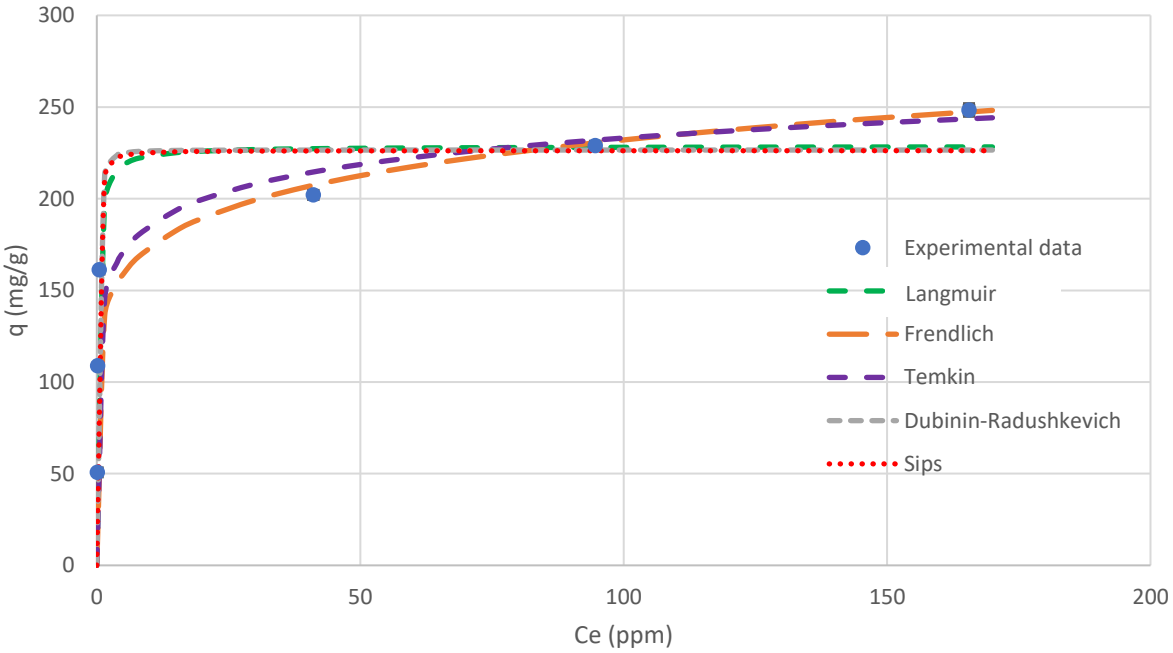

Figure 39 Non-linear isothem modeling curves of MoS_2-1:4 at pH 5.

Table 18 Summary of isotherm parameters in Cu^{2+} adsorption by MoS_2-1:7							
Langmuir isotherm							
Linear				Nonlinear			
q_m (mg/g)	b (L/mg)	r^2	RMSE	q_m (mg/g)	b (L/mg)	r^2	RMSE
204.3336 ± 7.1408	0.4805 ± 0.0674	0.9954 ± 0.0007	45.8178 ± 0.9408	185.2000 ± 3.6770	10.0070 ± 0.4568	0.9144 ± 0.0150	14.4481 ± 1.8616
Freundlich isotherm							
Linear				Non-linear			
n	K_f (L/mg)	r^2	RMSE	n	K_f(L/mg)	r^2	RMSE
7.4762 ± 0.2235	110.3694 ± 0.5980	0.7968 ± 0.0161	19.3038 ± 0.6720	8.8170 ± 0.4031	118.8500 ± 0.3536	0.8754 ± 0.0190	17.3792 ± 0.6032
Temkin isotherm							
Linear				Non-linear			
b (J/mol-K)	A (L/g)	r^2	RMSE	b (J/mol-K)	A (L/g)	r^2	RMSE
155.4955 ± 7.6351	2600.0110 ± 804.2589	0.9136 ± 0.0140	14.4676 ± 0.5770	155.5000 ± 7.6368	2600.0000 ± 804.6875	0.9136 ± 0.0140	14.4675 ± 0.5770
DR isotherm							
Linear				Non-linear			
k ($10^{-6}mol^2/kJ^2$)	q_e (mg/g)	r^2	RMSE	k ($10^{-6}mol^2/kJ^2$)	q_e(mg/g)	r^2	RMSE
0.0212 ± 0.0004	184.9063 ± 3.1109	0.9424 ± 0.0049	15.7897 ± 1.8863	0.1643 ± 0.2057	188.2500 ± 10.1116	0.7743 ± 0.2618	30.4806 ± 23.0887
Sips isotherm							
Non-linear							
q_m (mg/g)	b (L/mg)		m	r^2		RMSE	
201.35 ± 11.67	2.4765 ± 0.7333		2.0040 ± 0.3168	**0.9691 ± 0.0014**		**12.5877 ± 0.6405**	

Table 19 Summary of isotherm parameters in Cu^{2+} adsorption by MoS_2-1:4

Langmuir isotherm							
Linear				Nonlinear			
q_m (mg/g)	b (L/mg)	R^2	RMSE	q_m (mg/g)	b (L/mg)	R^2	RMSE
246.0861 ± 3.0255	0.3795 ± 0.0376	0.9961 ± 0.0010	62.8840 ± 1.2664	228.55 ± 1.061	4.3425 ± 0.0361	0.9577 ± 0.9541	18.1394 ± 0.6432
Freundlich isotherm							
Linear				Non-linear			
n	K_f (L/mg)	R^2	RMSE	n	K_f (L/mg)	R^2	RMSE
6.3533 ± 0.0210	116.8562 ± 0.2360	0.8619 ± 0.0023	27.6261 ± 0.1578	7.8955 ± 0.07849	129.5 ± 0	0.9161 ± 0.0014	25.0299 ± 0.0352
Temkin isotherm							
Linear				Non-Linear			
b (J/mol-K)	A (L/g)	r^2	RMSE	b (J/mol-K)	A (L/g)	r^2	RMSE
117.4143 ± 1.0427	632.5 ± 26.9	0.9621 ± 0.0009	23.3467 ± 0.0785	118.55 ± 1.2021	724.8 ± 39.2	0.8659 ± 0.0016	23.3152 ± 0.0801
DR isotherm							
Linear				Non-linear			
k ($10^{-6}mol^2/kJ^2$)	q_e (mg/g)	r^2	RMSE	k ($10^{-6}mol^2/kJ^2$)	q_e(mg/g)	r^2	RMSE
0.0237 ± 0.0001	211.1441 ± 0.6265	0.937 ± 0.0028	26.3344 ± 0.6993	0.0384 ± 0.002	226.55 ± 1.0607	**0.9614 ± 0.0030**	**16.9814 ± 0.7669**
Sips isotherm							
Non-linear							
q_m (mg/g)	b (L/mg)		m	R^2		RMSE	
226.20 ± 1.13	8.395 ± 0.3140		0.7205 ± 0.0086	**0.96155 ± 0.0030**		**16.9388 ± 0.7825**	

4.4.4 Effect of NaCl

The effect of NaCl on the Cu^{2+} adsorption (Figure 40) was investigated with MoS_2-1:4. The increase in the NaCl concentration obviously reduced the adsorption Cu^{2+} capacities by MoS_2-1:4. The presence of 100 mM and 500 mM NaCl led to a 23% and 50% reduction of the adsorption capacities respectively. The presence of 1 mM and 10 mM NaCl has no significant effect on adsorption capacity at p-value <0.05 by student's t-test. The effect of NaCl may suggest the formation of outer-sphere complex between Cu^{2+} and MoS_2-1:4. Outer-sphere and inner-sphere complex are common descriptions of the interaction between absorbent and adsorbate. In outer-sphere complex, the adsorbate is electrostatically attached by adsorbent while in inner-sphere complex, adsorbate form a chemical bonding with adsorbent.[120] In addition, the salt effect could also be attributed to the formation of $CuCl^+$ complex which had lower affinity to MoS_2.[121-122]

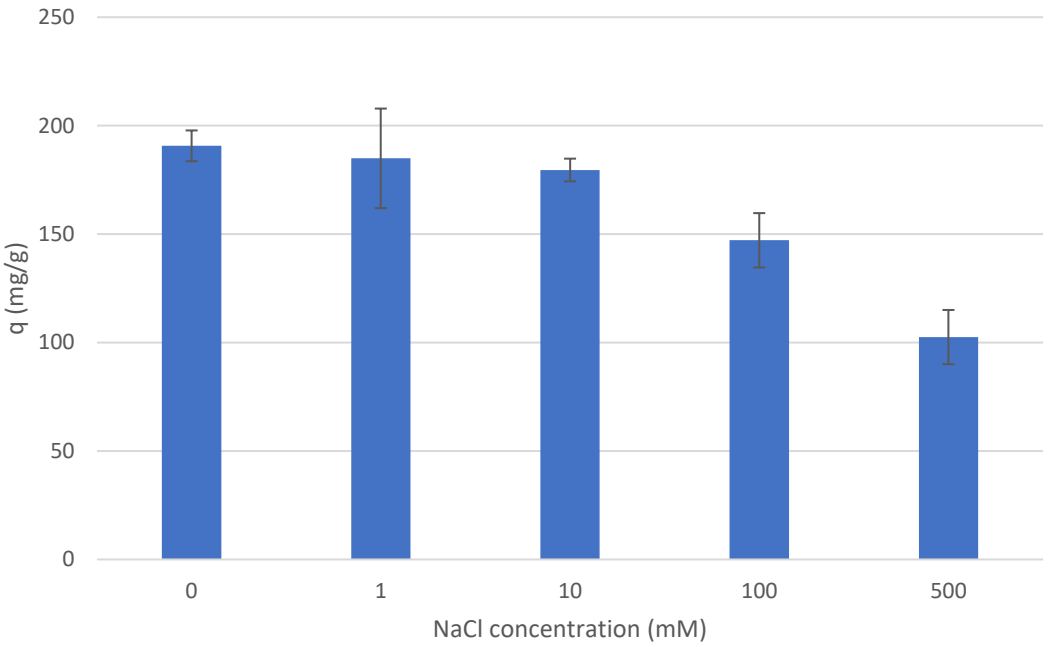

Figure 40 Effect of NaCl on Cu^{2+} adsorption by MoS_2-1:4.

[Initial Cu^{2+}concentration 2 mM, dose 0.5 g/L, pH 5.0, 250 rpm, 298 K, 24 hours]

4.5 Regeneration of MoS_2

Different desorption agents were tested for their ability to recover Cu^{2+}, and the results are summarized in Table 20. One molar HCl solution, which achieved ~93% Cu^{2+} removal, was found to be the best desorption agent. The percentage removal might be underestimated due to the washing step in the preparation of Cu^{2+}-loaded MoS_2-1:7. The combined use of HCl and disodium EDTA as desorption agent was unsuccessful as EDTA precipitated in acidic conditions.

The adsorption-desorption cycle operation was studied using 1 M HCl for MoS_2-1:7, and the results are summarized in Table 21. Three adsorption-desorption cycles were carried out, and 86% of the adsorption capacity remained in the third adsorption cycle. However, regeneration using 1 M HCl resulted in 9% weight loss of MoS_2 while the dispersion of MoS_2 into DDI water also caused 4.41% weight loss. The oxidation of MoS_2 by air contributed to the weight loss and hence reduced the adsorption capacity in the regeneration study.

Table 20 Desorption study of Cu^{2+} loaded MoS_2-1:7			
Desorption agent	% desorption	wt% S released to supernatant	wt% Mo released to supernatant
0.1 M HCl	38.76 %	2.57 %	2.39 %
1.0 M HCl	93.78 %	4.33 %	4.70 %
2.0 M HCl	93.65 %	3.54 %	3.95 %
4.0 M HCl	93.99 %	4.47 %	4.85 %
1.0 M HCl + 0.05 M EDTA	72.66 %	3.23 %	2.78 %
0.1 M HCl + 0.05 M EDTA	57.56 %	3.01 %	2.15 %
0.1 M thiourea + 0.1 M HCl	55.24 %	--	0.87 %
1 M NaCl	10.42 %	2.09 %	1.91 %
1 M Cysteine	0 %	--	0.17 %
0.1 M EDTA	67.21 %	1.86 %	1.93 %
1 M $CaCl_2$	13.18 %	1.92 %	1.79 %
DDI water	6.84 %	2.36 %	2.05 %
[Dose 4.4 g/L, 1 mL desorbing agents, 24 h, 250 rpm, 298 K]			

Table 21 Adsorption-desorption cycles for MoS_2-1:7 using 1 M HCl						
	Adsorption			Desorption		
	Adsorption (mg/g)	Mo loss	S loss	Desorption (mg/g)	Mo loss	S loss
1 cycle	129 ± 0.01	3.42 %	2.87 %	122.6 ± 5.5	4.06 %	3.09 %
2 cycle	126 ± 1.8	3.78 %	2.11 %	128.7 ± 5.5	2.48 %	1.37 %
3 cycle	112 ± 2.4	3.38 %	1.93 %	116.3 ± 14.4	2.08 %	1.24 %
Adsorption conditions: dose 0.5 g/L, pH 5.0, 1 mM Cu^{2+}, 10 mL, 24 h, 250 rpm, 298 K Desorption conditions: dose 4.4 g/L, 1 mL of 1.0 M HCl, 24 h, 250 rpm, 298 K						

4.6 Solubility test of $CuMoO_4$

MoO_4^{2-} and SO_4^{2-} have been reported to be the main oxidation products of MoS_2.[84] The low solubility of molybdate salts would lead to an overestimation of the Cu^{2+} adsorption capacity, and affect the adsorption affinity of Cu^{2+} to the MoS_2-based adsorbent. The solubility test of $CuMoO_4$ was conducted by mixing $CuNO_3$ and Na_2MoO_4 solutions in different concentrations. The results shown in Table 22 indicate that precipitation of $CuMoO_4$ would not occur and thus would not affect the results of the adsorption study when the concentrations of Mo and Cu were less than 100 and 132 ppm respectively. The results were consistent with the reported solubility of $CuMoO_4$ (0.038 g in 100 mL water at 25 ^oC, corresponding to 107.9 ppm Mo and 163 ppm Cu).

Table 22 Solubility test for $CuMoO_4$				
Mixture	Mo concentration in mixture (ppm)	Cu concentration in mixture (ppm)	measured Mo concentration (ppm)	measured Cu concentration (ppm)
A	100	12.7	106.596	13.95
B	100	25.4	107.795	27.65
C	100	38.1	106.811	40.26
D	100	95.25	105.706	97.30
E	100	63.5	105.238	64.00
F	100	127	109.113	132.22
Mixture prepared by mixing $Na_2MoO_4.2H_2O$ and $Cu(NO_3)_2.3H_2O$ solutions				

4.7 Proposed Cu^{2+} adsorption mechanism

The adsorption mechanism of Cu^{2+} on MoS_2-1:4 was proposed based on the results of XPS, SEM-EDX, XRD and the adsorption experiments. The adsorption performance of MoS_2-1:4 and MoS_2-1:7 towards Cu^{2+} was significantly higher than bulk-MoS_2 and MoS_2-1:2. The experimental results suggested that the chemical and structural differences in edge sites contributed to this observation.

The results of XRD and SEM revealed that MoS_2-1:4 and MoS_2-1:7 were an aggregation of thinner nanoflakes MoS_2 with maximum edge site exposure. In the XRD study, as shown in Figure 15, the intensity of the (002) diffraction peak in MoS_2-1:4 and MoS_2-1:7 was significantly weaker than bulk-MoS_2 and MoS_2-1:2, suggesting a few- or single-layered MoS_2 nanosheet structure.[90] Low crystallinity may also contribute to a (002) weak diffraction peak, but this would not be the case in this study. MoS_2-1:4 and MoS_2-1:7 were synthesized at 200 ^oC, which should be adequate for the growth of MoS_2 with high crystallinity. In the literature, a medium intensity of (002) diffraction peak was reported[93], even when the synthetic temperature was as low as 140 ^oC. The SEM images further revealed that MoS_2-1:4 and MoS_2-1:7 were composed of MoS_2 nanosheets which were much thinner than the bulk-MoS_2 and MoS_2-1:2. The thinner MoS_2 nanosheets would provide more edge site exposure, so the adsorption capacity should increase as the quantity of active sites increases.

The XPS study revealed furthermore that MoS_2-1:7 and MoS_2-1:4 had significantly higher atomic concentrations of S_2^{2-} than MoS_2-1:2 and bulk-MoS_2 (Figure 22). It has also been reported in the literature that the S_2^{2-} species were predominately located at the edge

of MoS_2 and generally considered to be the active sites for hydrogen evolution reaction.[90, 92, 123-124] The present XPS study indicated that the S_2^{2-} species were abundant at the edges of MoS_2-1:4 and MoS_2-1:7. The S_2^{2-} species can directly capture Cu^{2+} by soft-soft interaction between the sulfide group and Cu^{2+}. MoS_2-1:4 and MoS_2-1:7 have at least twenty times larger Cu^{2+} adsorption capacity than bulk-MoS_2 (Table 6). This tremendous difference in adsorption ability between MoS_2-1:4, MoS_2-1:7 and bulk MoS_2 can be attributed to the plenty of S_2^{2-} species at the edges of MoS_2-1:4 and MoS_2-1:7, which provides abundant active sites for the adsorption of Cu^{2+}. Ai *et al*.[12] studied the use of MoS_2 nanosheets with expanded layers to adsorb various heavy metal ions. Although their MoS_2 nanosheets showed excellent performance on Hg^{2+} adsorption (2,506 mg/g), their adsorbent could only achieve about 50% removal of Cu^{2+} in 10 ppm Cu^{2+} solutions with a dose of 0.1 g/L, corresponding to a Cu^{2+} adsorption capacity of 50 mg/g. They have also employed XPS to analyze their MoS_2 samples and discovered that the characteristic peaks of S^{2-} species dominated the resulting XPS spectra. The huge difference in adsorption ability between Cu^{2+} and Hg^{2+} can be attributed to the lack of S_2^{2-} species and predomination of S^{2-} species in their MoS_2 nanosheets[12]. Unlike the MoS_2 nanosheets studied, the MoS_2-1:4 and MoS_2-1:7 nanoflakes had plentiful S_2^{2-} species, offering a lot of active binding sites for Cu^{2+} ions.

Additionally, the S_2^{2-} species may be able to reduce Cu^{2+} to Cu^{+}. The reduction of Cu^{2+} to Cu^{+} can increase the adsorption affinity and capacity of MoS_2 towards copper. Cu^{+} is classified as a soft ion in HSAB theory, which may have a stronger affinity than Cu^{2+} towards MoS_2 materials. The S^{2-} located on the basal plane may thus be able to adsorb soft Cu^{+}. However, there is no direct evidence proving the formation of adsorbed Cu^{+} in MoS_2

samples. Further research work is needed to establish if reduction of Cu^{2+} to Cu^{+} has occurred in MoS_2-based adsorbents,

Chapter 5 Conclusion

In conclusion, various MoS_2 based absorbents were synthesized and characterized. MoS_2-1:4 and MoS_2-1:7 were found to be effective Cu^{2+} adsorbents with high adsorption capacity, high affinity, fast kinetic, and capability of regeneration. Bulk-MoS_2 and MoS_2-1:2 had very low adsorption capacity. This huge difference in adsorption performance was mainly attributed to chemical property and morphology. The SEM images showed that bulk-MoS_2 was composed of plate-like particles with a lateral size of 200 to 2,000 nm and a smooth surface, and MoS_2-1:2 consisted of nanosheet-assembled MoS_2 nanoflowers. High-magnification (~55,000x) SEM images revealed that MoS_2-1:4 and MoS_2-1:7 were wire-brush like and made of aggregated MoS_2 nanoflakes with edge site exposure. The unique morphology of MoS_2-1:4 and MoS_2-1:7 maximized adsorption site exposure resulting in good adsorption performance. The XPS study showed that MoS_2-1:4 and MoS_2-1:7 were abundant in S_2^{2-} species, while MoS_2-1:2 lacked S_2^{2-} species. Since S_2^{2-} species were believed to be active sites for Cu^{2+} capturing, the low atomic concentration of S_2^{2-} in MoS_2-1:2 and bulk-MoS_2 would lead to a lower Cu^{2+} adsorption capacity compared with MoS_2-1:4 and MoS_2-1:7. Two Cu^{2+} adsorption mechanism was proposed based on adsorption performance and XPS result. The first mechanism was direct adsorption between active site S_2^{2-} and Cu^{2+}. The second mechanism involves the reduction of Cu^{2+} to Cu^{+} by S_2^{2-} and then captured by the S^{2-} located on the basal plane.

The MoS_2-1:4 and MoS_2-1:7 have demonstrated great potential as a highly effective adsorbent for the removal of Cu^{2+} from wastewater and contaminated water. The role of

S_2^{2-} species in the adsorption of Cu^{2+} on the MoS_2 nanosheets was first reported in this study. This can offer an alternative strategy to the precise engineering of MoS_2 adsorbent in the future

Chapter 6 Further Studies

Further study mainly related to adsorption mechanism, real application, and detailed morphology studies.

Our study shows that S_2^{2-} species play a very important role in the adsorption of Cu^{2+}. Conducting Cu^{2+} adsorption studies on MoS_2 prepared by other methods, such as chemical exfoliation and ultrasonic exfoliation can strengthen the proposed role of S_2^{2-} species. Chemical exfoliation and ultrasonic exfoliation are well-established method for the preparation of MoS_2 nanosheets.[84] If MoS_2 prepared by different methods has abundant S_2^{2-} species and high Cu^{2+} adsorption capacity simultaneously, our proposed role about S_2^{2-} species is more persuasive.

A reduction-adsorption mechanism was proposed for copper adsorption on MoS_2. However, the existence of Cu^+ had not yet be confirmed in Cu-loaded MoS_2. It is believed that other spectroscopy such as X-ray absorption near edge structure (XANES) may be able to identify the oxidation of copper in Cu-loaded MoS_2. Besides direct observation of Cu^+, indirect methods may be able to investigate the oxidation state of copper. Cu^+ is a catalyst in many reactions, such as atom transfer radical polymerization.[125] If Cu-loaded MoS_2 can replace Cu^+ to catalyze the same reaction, this will indirectly indicate the existence of Cu^+ in Cu-loaded MoS_2.

A pure Cu^{2+} solution was used in our adsorption study. Real wastewater, especially electroplating wastewater often contains complexing agents. Cu^{2+} adsorption can be conducted with simulated wastewater spiked with complexing agents.

Our study shows that MoS_2 sample was slowly oxidized in regeneration and adsorption study. Regeneration and adsorption study can be conducted in an oxygen-free environment such as a glove box filled with N_2. This study can confirm the weight loss of MoS_2 during regeneration and adsorption is attributed to oxidation by oxygen rather than damage by regenerant or adsorbate. Also, regeneration of MoS_2 in the presence of antioxidants such as ascorbic acid may suppress the oxidation of MoS_2 based adsorbent during the desorption process.

Detailed morphologic study enables us to develop a better understanding of the relationship between activity and morphology. Thickness of nanosheets in MoS_2-1:7 and MoS_2-1:4 should be estimated by employing transmission electron microscopy (TEM), since the number of MoS_2 layers has a great effect in activity of HER. Also, the morphologic formation of wire-brush like MoS_2-1:7 and MoS_2-1:4 cam be investigated by time-dependent SEM study.

Chapter 7 References

1. Gaetke, L. M.; Chow, C. K., Copper toxicity, oxidative stress, and antioxidant nutrients. *Toxicology* **2003,** *189* (1-2), 147-163.
2. Mal, T. K.; Adorjan, P.; Corbett, A. L., Effect of copper on growth of an aquatic macrophyte, Elodea canadensis. *Environ Pollut* **2002,** *120* (2), 307-311.
3. Yuvaraja, G.; Subbaiah, M. V.; Krishnaiah, A., Caesalpinia bonducella leaf powder as biosorbent for Cu(II) removal from aqueous environment: Kinetics and isotherms. *Ind Eng Chem Res* **2012,** *51* (34), 11218-11225.
4. Electroplating and metal finishing pretreatment guidance. https://www.epa.gov/sites/production/files/2015-10/documents/electroplating-and-metal_finishing_pretreatment-guidance_feb-1984.pdf (accessed 17-8-2018).
5. Fu, F. L.; Wang, Q., Removal of heavy metal ions from wastewaters: A review. *J Environ Manage* **2011,** *92* (3), 407-418.
6. Pearson, R. G., Hard and soft acids and bases. In *Survey of progress in chemistry*, Scott, A. F., Ed. Academic Press,INC: New York, 1969; Vol. 5, pp 1-51.
7. Ma, S. L.; Chen, Q. M.; Li, H.; Wang, P. L.; Islam, S. M.; Gu, Q. Y.; Yang, X. J.; Kanatzidis, M. G., Highly selective and efficient heavy metal capture with polysulfide intercalated layered double hydroxides. *Journal of Materials Chemistry A* **2014,** *2* (26), 10280-10289.
8. Li, J. R.; Wang, X.; Yuan, B. L.; Fu, M. L., Layered chalcogenide for Cu^{2+} removal by ion-exchange from wastewater. *Journal of Molecular Liquids* **2014,** *200*, 205-212.
9. Manos, M. J.; Kanatzidis, M. G., Metal sulfide ion exchangers: superior sorbents for the capture of toxic and nuclear waste-related metal ions. *Chem Sci* **2016,** *7* (8), 4804-4824.
10. Ma, S. L.; Huang, L.; Ma, L. J.; Shim, Y.; Islam, S. M.; Wang, P. L.; Zhao, L. D.; Wang, S. C.; Sun, G. B.; Yang, X. J.; Kanatzidis, M. G., Efficient uranium capture by polysulfide/layered double hydroxide composites. *Journal of the American Chemical Society* **2015,** *137* (10), 3670-3677.
11. Ma, S. L.; Shim, Y.; Islam, S. M.; Subrahmanyam, K. S.; Wang, P. L.; Li, H.; Wang, S. C.; Yang, X. J.; Kanatzidis, M. G., Efficient Hg vapor capture with polysulfide intercalated layered double hydroxides. *Chem Mater* **2014,** *26* (17), 5004-5011.
12. Ai, K. L.; Ruan, C. P.; Shen, M. X.; Lu, L. H., MoS_2 nanosheets with widened interlayer spacing for high-efficiency removal of mercury in aquatic systems. *Advanced Functional Materials* **2016,** *26* (30), 5542-5549.
13. Liu, C.; Jia, F. F.; Wang, Q. M.; Yang, B. Q.; Song, S. X., Two-dimensional molybdenum disulfide as adsorbent for high-efficient Pb(II) removal from water. *Applied Materials Today* **2017,** *9*, 220-228.
14. Zhang, H., Ultrathin two-dimensional nanomaterials. *Acs Nano* **2015,** *9* (10), 9451-9469.

15. Fard, Z. H.; Malliakas, C. D.; Mertz, J. L.; Kanatzidis, M. G., Direct extraction of Ag^{+} and Hg^{2+} from cyanide complexes and mode of binding by the layered $K_2MgSn_2S_6$ (KMS-2). *Chem Mater* **2015,** *27* (6), 1925-1928.
16. Ma, L. J.; Wang, Q.; Islam, S. M.; Liu, Y. C.; Ma, S. L.; Kanatzidis, M. G., Highly selective and efficient removal of heavy metals by layered double hydroxide intercalated with the MoS_4^{2-} Ion. *Journal of the American Chemical Society* **2016,** *138* (8), 2858-2866.
17. Sarma, D.; Islam, S. M.; Subrahmanyam, K. S.; Kanatzidis, M. G., Efficient and selective heavy metal sequestration from water by using layered sulfide $K_{2x}Sn_{4-x}S_{8-x}$ (x=0.65-1; KTS-3). *Journal of Materials Chemistry A* **2016,** *4* (42), 16597-16605.
18. Ali, J.; Wang, H. B.; Ifthikar, J.; Khan, A.; Wang, T.; Zhan, K.; Shahzad, A.; Chen, Z. L.; Chen, Z. Q., Efficient, stable and selective adsorption of heavy metals by thio-functionalized layered double hydroxide in diverse types of water. *Chem Eng J* **2018,** *332*, 387-397.
19. Song, Y. H.; Lu, M. C.; Huang, B.; Wang, D. L.; Wang, G.; Zhou, L., Decoration of defective MoS_2 nanosheets with Fe_3O_4 nanoparticles as superior magnetic adsorbent for highly selective and efficient mercury ions (Hg^{2+}) removal. *Journal of Alloys and Compounds* **2018,** *737*, 113-121.
20. Manos, M. J.; Kanatzidis, M. G., Sequestration of heavy metals from water with layered metal sulfides. *Chemistry-a European Journal* **2009,** *15* (19), 4779-4784.
21. Manos, M. J.; Petkov, V. G.; Kanatzidis, M. G., $H_{2x}Mn_xSn_{3-x}S_6$ (x=0.11-0.25): A novel reusable sorbent for highly specific mercury capture under extreme pH conditions. *Advanced Functional Materials* **2009,** *19* (7), 1087-1092.
22. Chen, B.; Bi, H. C.; Ma, Q. L.; Tan, C. L.; Cheng, H. F.; Chen, Y.; He, X. Y.; Sun, L. T.; Lim, T. T.; Huang, L.; Zhang, H., Preparation of graphene-MoS_2 hybrid aerogels as multifunctional sorbents for water remediation. *Science China-Materials* **2017,** *60* (11), 1102-1108.
23. Gash, A. E.; Spain, A. L.; Dysleski, L. M.; Flaschenriem, C. J.; Kalaveshi, A.; Dorhout, P. K.; Strauss, S. H., Efficient recovery of elemental mercury from Hg(II)-contaminated aqueous media using a redox-recyclable ion-exchange material. *Environmental Science & Technology* **1998,** *32* (7), 1007-1012.
24. Zhi, L. H.; Zuo, W.; Chen, F. J.; Wang, B. D., 3D MoS_2 composition aerogels as chemosensors and adsorbents for colorimetric detection and high-capacity adsorption of Hg^{2+}. *Acs Sustain Chem Eng* **2016,** *4* (6), 3398-3408.
25. Jia, F. F.; Wang, Q. M.; Wu, J. S.; Li, Y. M.; Song, S. X., Two-dimensional molybdenum disulfide as a superb adsorbent for removing Hg^{2+} from water. *Acs Sustain Chem Eng* **2017,** *5* (8), 7410-7419.
26. Li, J. R.; Wang, X.; Yuan, B. L.; Fu, M. L.; Cui, H. J., Robust removal of heavy metals from water by intercalation chalcogenide $[CH_3NH_3]_{(2x)}Mn_xSn_{3-x}S_6.0.5H_2O$. *Appl Surf Sci* **2014,** *320*, 112-119.
27. Mertz, J. L.; Fard, Z. H.; Malliakas, C. D.; Manos, M. J.; Kanatzidis, M. G., Selective removal of Cs^{+}, Sr^{2+}, and Ni^{2+} by $K_{2x}Mg_xSn_{3-x}S_6$ (x=0.5-1) (KMS-2) relevant to nuclear waste remediation. *Chem Mater* **2013,** *25* (10), 2116-2127.
28. Sarma, D.; Malliakas, C. D.; Subrahmanyam, K. S.; Islama, S. M.; Kanatzidis, M. G., $K_{2x}Sn_{4-x}S_{8-x}$ (x=0.65-1): a new metal sulfide for rapid and selective removal of Cs^{+}, Sr^{2+} and UO_2^{2+} ions. *Chem Sci* **2016,** *7* (2), 1121-1132.

29. Qi, X. H.; Du, K. Z.; Feng, M. L.; Li, J. R.; Du, C. F.; Zhang, B.; Huang, X. Y., A two-dimensionally microporous thiostannate with superior Cs^{+} and Sr^{2+} ion-exchange property. *Journal of Materials Chemistry A* **2015,** *3* (10), 5665-5673.
30. Manos, M. J.; Ding, N.; Kanatzidis, M. G., Layered metal sulfides: Exceptionally selective agents for radioactive strontium removal. *Proceedings of the National Academy of Sciences of the United States of America* **2008,** *105* (10), 3696-3699.
31. Manos, M. J.; Kanatzidis, M. G., Layered metal sulfides capture uranium from seawater. *Journal of the American Chemical Society* **2012,** *134* (39), 16441-16446.
32. Ma, L. J.; Islam, S. M.; Xiao, C. L.; Zhao, J.; Liu, H. Y.; Yuan, M. W.; Sun, G. B.; Li, H. F.; Ma, S. L.; Kanatzidis, M. G., Rapid simultaneous removal of toxic anions $[HSeO_3]^{-}$, $[SeO_3]^{2-}$, and $[SeO_4]^{2-}$, and metals Hg^{2+}, Cu^{2+}, and Cd^{2+} by MoS_4^{2-} Intercalated layered double hydroxide. *Journal of the American Chemical Society* **2017,** *139* (36), 12745-12757.
33. Ma, L. J.; Islam, S. M.; Liu, H. Y.; Zhao, J.; Sun, G. B.; Li, H. F.; Ma, S. L.; Kanatzidis, M. G., Selective and efficient removal of toxic oxoanions of As(III), As(V), and Cr(VI) by layered double hydroxide intercalated with MoS_4^{2-}. *Chem Mater* **2017,** *29* (7), 3274-3284.
34. Wang, J.; Zhang, W. T.; Yue, X. Y.; Yang, Q. F.; Liu, F. B.; Wang, Y. R.; Zhang, D. H.; Li, Z. H.; Wang, J. L., One-pot synthesis of multifunctional magnetic ferrite-MoS_2-carbon dot nanohybrid adsorbent for efficient Pb(II) removal. *Journal of Materials Chemistry A* **2016,** *4* (10), 3893-3900.
35. Mondal, B.; Mahendranath, A.; Som, A.; Bose, S.; Ahuja, T.; Kumar, A. A.; Ghosh, J.; Pradeep, T., Rapid reaction of MoS_2 nanosheets with Pb^{2+} and Pb^{4+} ions in solution. *Nanoscale* **2018,** *10* (4), 1807-1814.
36. Li, W. J.; Shi, E. W.; Ko, J. M.; Chen, Z. Z.; Ogino, H.; Fukuda, T., Hydrothermal synthesis of MoS_2 nanowires. *Journal of Crystal Growth* **2003,** *250* (3-4), 418-422.
37. Afanasiev, P.; Geantet, C.; Llorens, I.; Proux, O., Biotemplated synthesis of highly divided MoS_2 catalysts. *Journal of Materials Chemistry* **2012,** *22* (19), 9731-9737.
38. Zhang, Z. Y.; Li, W. Y.; Yuen, M. F.; Ng, T. W.; Tang, Y. B.; Lee, C. S.; Chen, X. F.; Zhang, W. J., Hierarchical composite structure of few-layers MoS_2 nanosheets supported by vertical graphene on carbon cloth for high-performance hydrogen evolution reaction. *Nano Energy* **2015,** *18*, 196-204.
39. Huang, G. W.; Liu, H.; Wang, S. P.; Yang, X.; Liu, B. H.; Chen, H. Z.; Xu, M. S., Hierarchical architecture of WS_2 nanosheets on graphene frameworks with enhanced electrochemical properties for lithium storage and hydrogen evolution. *Journal of Materials Chemistry A* **2015,** *3* (47), 24128-24138.
40. Ratha, S.; Rout, C. S., Supercapacitor electrodes based on layered tungsten disulfide-reduced graphene oxide hybrids synthesized by a facile hydrothermal method. *Acs Applied Materials & Interfaces* **2013,** *5* (21), 11427-11433.
41. He, J. N.; Liang, Y. Q.; Mao, J.; Zhang, X. M.; Yang, X. J.; Cui, Z. D.; Zhu, S. L.; Li, Z. Y.; Li, B. B., 3D tungsten-doped MoS_2 nanostructure: A low-cost, facile prepared catalyst for hydrogen evolution reaction. *Journal of the Electrochemical Society* **2016,** *163* (5), H299-H304.

42. Bokhimi, X.; Toledo, J. A.; Navarrete, J.; Sun, X. C.; Portilla, M., Thermal evolution in air and argon of nanocrystalline MoS_2 synthesized under hydrothermal conditions. *International Journal of Hydrogen Energy* **2001,** *26* (12), 1271-1277.
43. Li, X. L.; Li, Y. D., MoS_2 nanostructures: Synthesis and electrochemical Mg^{2+} intercalation. *Journal of Physical Chemistry B* **2004,** *108* (37), 13893-13900.
44. Qiao, X. Q.; Hu, F. C.; Hou, D. F.; Li, D. S., PEG assisted hydrothermal synthesis of hierarchical MoS_2 microspheres with excellent adsorption behavior. *Materials Letters* **2016,** *169*, 241-245.
45. Tian, Y.; He, Y.; Zhu, Y. F., Hydrothermal synthesis of fine MoS_2 crystals from Na_2MoO_4 and KSCN. *Chemistry Letters* **2003,** *32* (8), 768-769.
46. Peng, Y. Y.; Meng, Z. Y.; Zhong, C.; Lu, J.; Yu, W. C.; Jia, Y. B.; Qian, Y. T., Hydrothermal synthesis and characterization of single-molecular-layer MoS_2 and $MoSe_2$. *Chemistry Letters* **2001,** (8), 772-773.
47. Chen, X. H.; Fan, R., Low-temperature hydrothermal synthesis of transition metal dichalcogenides. *Chem Mater* **2001,** *13* (3), 802-805.
48. Wang, Y.; Ni, Y. N., Molybdenum disulfide quantum dots as a photoluminescence sensing platform for 2,4,6-trinitrophenol detection. *Analytical Chemistry* **2014,** *86* (15), 7463-7470.
49. Park, S. K.; Yu, S. H.; Woo, S.; Ha, J.; Shin, J.; Sung, Y. E.; Piao, Y., A facile and green strategy for the synthesis of MoS_2 nanospheres with excellent Li-ion storage properties. *Crystengcomm* **2012,** *14* (24), 8323-8325.
50. Ma, L.; Zhou, X. P.; Xu, L. M.; Xu, X. Y.; Zhang, L. L.; Chen, W. X., Ultrathin few-layered molybdenum selenide/graphene hybrid with superior electrochemical Li-storage performance. *Journal of Power Sources* **2015,** *285*, 274-280.
51. Wu, Y. X.; Xu, M. Q.; Chen, X.; Yang, S. L.; Wu, H. S.; Pan, J.; Xiong, X., CTAB-assisted synthesis of novel ultrathin $MoSe_2$ nanosheets perpendicular to graphene for the adsorption and photodegradation of organic dyes under visible light. *Nanoscale* **2016,** *8* (1), 440-450.
52. Chen, D. Y.; Ji, G.; Ding, B.; Ma, Y.; Qu, B. H.; Chen, W. X.; Lee, J. Y., In situ nitrogenated graphene-few-layer WS_2 composites for fast and reversible Li^+ storage. *Nanoscale* **2013,** *5* (17), 7890-7896.
53. Yoosuk, B.; Kim, J. H.; Song, C.; Ngamcharussrivichai, C.; Prasassarakich, P., Highly active MoS_2, $CoMoS_2$ and $NiMoS_2$ unsupported catalysts prepared by hydrothermal synthesis for hydrodesulfurization of 4,6-dimethyldibenzothiophene. *Catalysis Today* **2008,** *130* (1), 14-23.
54. Li, N.; Chai, Y. M.; Li, Y. P.; Tang, Z.; Dong, B.; Liu, Y. Q.; Liu, C. G., Ionic liquid assisted hydrothermal synthesis of hollow vesicle-like MoS_2 microspheres. *Materials Letters* **2012,** *66* (1), 236-238.
55. Sen, U. K.; Mitra, S., High-rate and high-energy-density lithium-ion battery anode containing 2D MoS_2 nanowall and cellulose binder. *Acs Applied Materials & Interfaces* **2013,** *5* (4), 1240-1247.
56. Huang, Y. P.; Miao, Y. E.; Zhang, L. S.; Tjiu, W. W.; Pan, J. S.; Liu, T. X., Synthesis of few-layered MoS_2 nanosheet-coated electrospun SnO_2 nanotube heterostructures for enhanced hydrogen evolution reaction. *Nanoscale* **2014,** *6* (18), 10673-10679.

57. Yang, L. J.; Zhou, W. J.; Hou, D. M.; Zhou, K.; Li, G. Q.; Tang, Z. H.; Li, L. G.; Chen, S. W., Porous metallic MoO_2-supported MoS_2 nanosheets for enhanced electrocatalytic activity in the hydrogen evolution reaction. *Nanoscale* **2015,** *7* (12), 5203-5208.
58. Zhang, N.; Ma, W. G.; Wu, T. S.; Wang, H. Y.; Han, D. X.; Niu, L., Edge-rich MoS_2 naonosheets rooting into polyaniline nanofibers as effective catalyst for electrochemical hydrogen evolution. *Electrochimica Acta* **2015,** *180*, 155-163.
59. Shang, Y. Z.; Xia, J. B.; Xu, Z. D.; Chen, W. X., Hydrothermal synthesis and characterization of quasi-1-D tungsten disulfide nanocrystal. *Journal of Dispersion Science and Technology* **2005,** *26* (5), 635-639.
60. Qu, B.; Yu, X. B.; Chen, Y. J.; Zhu, C. L.; Li, C. Y.; Yin, Z. X.; Zhang, X. T., Ultrathin $MoSe_2$ nanosheets decorated on carbon fiber cloth as binder-free and high-performance electrocatalyst for hydrogen evolution. *Acs Applied Materials & Interfaces* **2015,** *7* (26), 14170-14175.
61. Zhang, X. Y.; Zhang, S. F.; Chen, B. H.; Wang, H.; Wu, K.; Chen, Y.; Fan, J. T.; Qi, S.; Cui, X. L.; Zhang, L.; Wang, J., Direct synthesis of large-scale hierarchical MoS_2 films nanostructured with orthogonally oriented vertically and horizontally aligned layers. *Nanoscale* **2016,** *8* (1), 431-439.
62. Luo, H.; Xu, C.; Zou, D. B.; Wang, L.; Ying, T. K., Hydrothermal synthesis of hollow MoS_2 microspheres in ionic liquids/water binary emulsions. *Materials Letters* **2008,** *62* (20), 3558-3560.
63. Du, H.; Liu, D.; Li, M.; Al Otaibi, R. L.; Lv, R. Q.; Zhang, Y. D., Solvothermal synthesis of MoS_2 nanospheres in DMF-water mixed solvents and their catalytic activity in hydrocracking of diphenylmethane. *Rsc Advances* **2015,** *5* (97), 79724-79728.
64. Zhang, N.; Gan, S. Y.; Wu, T. S.; Ma, W. G.; Han, D. X.; Niu, L., Growth control of MoS_2 nanosheets on carbon cloth for maximum active edges exposed: An excellent hydrogen evolution 3D cathode. *Acs Applied Materials & Interfaces* **2015,** *7* (22), 12193-12202.
65. Gao, M. R.; Chan, M. K. Y.; Sun, Y. G., Edge-terminated molybdenum disulfide with a 9.4-angstrom interlayer spacing for electrochemical hydrogen production. *Nature Communications* **2015,** *6*.
66. Dunne, P. W.; Munn, A. S.; Starkey, C. L.; Lester, E. H., The sequential continuous-flow hydrothermal synthesis of molybdenum disulphide. *Chemical Communications* **2015,** *51* (19), 4048-4050.
67. Wang, H. Y.; Wang, B. Y.; Wang, D.; Lu, L.; Wang, J. G.; Jiang, Q. C., Facile synthesis of hierarchical worm-like MoS_2 structures assembled with nanosheets as anode for lithium ion batteries. *Rsc Advances* **2015,** *5* (71), 58084-58090.
68. Erickson, B. E.; Helz, G. R., Molybdenum(VI) speciation in sulfidic waters: Stability and lability of thiomolybdates. *Geochimica Et Cosmochimica Acta* **2000,** *64* (7), 1149-1158.
69. Tian, Y.; He, Y.; Zhu, Y. F., Low temperature synthesis and characterization of molybdenum disulfide nanotubes and nanorods. *Materials Chemistry and Physics* **2004,** *87* (1), 87-90.
70. Sun, P. L.; Zhang, W. X.; Hu, X. L.; Yuan, L. X.; Huang, Y. H., Synthesis of hierarchical MoS_2 and its electrochemical performance as an anode material for lithium-ion batteries. *Journal of Materials Chemistry A* **2014,** *2* (10), 3498-3504.

71. Cao, S. X.; Liu, T. M.; Hussain, S.; Zeng, W.; Peng, X. H.; Pan, F. S., Hydrothermal synthesis of variety low dimensional WS_2 nanostructures. *Materials Letters* **2014,** *129*, 205-208.
72. Huang, Y. P.; Miao, Y. E.; Fu, J.; Mo, S. Y.; Wei, C.; Liu, T. X., Perpendicularly oriented few-layer $MoSe_2$ on SnO_2 nanotubes for efficient hydrogen evolution reaction. *Journal of Materials Chemistry A* **2015,** *3* (31), 16263-16271.
73. Li, Y. G.; Wang, H. L.; Xie, L. M.; Liang, Y. Y.; Hong, G. S.; Dai, H. J., MoS_2 nanoparticles grown on graphene: An advanced catalyst for the hydrogen evolution reaction. *Journal of the American Chemical Society* **2011,** *133* (19), 7296-7299.
74. Tang, G. G.; Tang, H.; Li, C. S.; Li, W. J.; Ji, X. R., Surfactant-assisted hydrothermal synthesis and characterization of WS_2 nanorods. *Materials Letters* **2011,** *65* (23-24), 3457-3460.
75. Tang, G. G.; Sun, J. R.; Wei, C.; Wu, K. Q.; Ji, X. R.; Liu, S. S.; Tang, H.; Li, C. S., Synthesis and characterization of flowerlike MoS_2 nanostructures through CTAB-assisted hydrothermal process. *Materials Letters* **2012,** *86*, 9-12.
76. Zhang, S. P.; Chowdari, B. V. R.; Wen, Z. Y.; Jin, J.; Yang, J. H., Constructing highly oriented configuration by few-layer MoS_2: Toward high-performance lithium-ion batteries and hydrogen evolution reactions. *Acs Nano* **2015,** *9* (12), 12464-12472.
77. Li, Q.; Wu, Z. X.; Feng, D.; Tu, B.; Zhao, D. Y., Hydrothermal stability of mesostructured cellular silica foams. *Journal of Physical Chemistry C* **2010,** *114* (11), 5012-5019.
78. Schmidt-Winkel, P.; Lukens, W. W.; Zhao, D. Y.; Yang, P. D.; Chmelka, B. F.; Stucky, G. D., Mesocellular siliceous foams with uniformly sized cells and windows. *Journal of the American Chemical Society* **1999,** *121* (1), 254-255.
79. Young, C. G., Oxomolybdenum chemistry - an experiment. *J Chem Educ* **1995,** *72* (8), 751-753.
80. Qiu, H.; Lv, L.; Pan, B. C.; Zhang, Q. J.; Zhang, W. M.; Zhang, Q. X., Critical review in adsorption kinetic models. *J Zhejiang Univ-Sc A* **2009,** *10* (5), 716-724.
81. Limousin, G.; Gaudet, J. P.; Charlet, L.; Szenknect, S.; Barthes, V.; Krimissa, M., Sorption isotherms: A review on physical bases, modeling and measurement. *Appl Geochem* **2007,** *22* (2), 249-275.
82. Foo, K. Y.; Hameed, B. H., Insights into the modeling of adsorption isotherm systems. *Chem Eng J* **2010,** *156* (1), 2-10.
83. Yang, Y.; Liu, T.; Cheng, L.; Song, G. S.; Liu, Z.; Chen, M. W., MoS_2-based nanoprobes for detection of silver ions in aqueous solutions and bacteria. *Acs Applied Materials & Interfaces* **2015,** *7* (14), 7526-7533.
84. Wang, Z. Y.; von dem Bussche, A.; Qiu, Y.; Valentin, T. M.; Gion, K.; Kane, A. B.; Hurt, R. H., Chemical dissolution pathways of MoS_2 nanosheets in biological and environmental media. *Environmental Science & Technology* **2016,** *50* (13), 7208-7217.
85. Lide, D. R.; Bruno, T. J.; Haynes, W. M., *CRC handbook of chemistry and physics : a ready-reference book of chemical and physical data*. 94 th ed.; CRC Press: Florida, 2013.
86. Perry, D. L., *Handbook of inorganic compounds*. 2nd ed.; Taylor & Francis: Boca Raton, 2011; p xxvii, 553 p.

87. Zhao, H. T.; Yang, G.; Gao, X.; Pang, C. H.; Kingman, S. W.; Wu, T., Hg^0 capture over CoMoS/gamma-Al_2O_3 with MoS_2 nanosheets at low temperatures. *Environmental Science & Technology* **2016,** *50* (2), 1056-1064.
88. Jianwei Miao, F.-X. X., Hong Bin Yang, Si Yun Khoo, Jiazang Chen, Zhanxi Fan, Ying-Ya Hsu, Hao Ming Che, Hua Zhang,and Bin Liu, Hierarchical Ni-Mo-S nanosheets on carbon fiber cloth: A flexible electrode for efficient hydrogen generation in neutral electrolyte. *Science Advances* **2015,** *1* (7).
89. Moritz, M.; Geszke-Moritz, M., Aminopropyl-modified mesoporous molecular sieves as efficient adsorbents for removal of auxins. *Appl Surf Sci* **2015,** *331*, 415-426.
90. Seo, B.; Jung, G. Y.; Sa, Y. J.; Jeong, H. Y.; Cheon, J. Y.; Lee, J. H.; Kim, H. Y.; Kim, J. C.; Shin, H. S.; Kwak, S. K.; Joo, S. H., Monolayer-precision synthesis of molybdenum sulfide nanoparticles and their nanoscale size effects in the hydrogen evolution reaction. *Acs Nano* **2015,** *9* (4), 3728-3739.
91. Xie, J. F.; Zhang, J. J.; Li, S.; Grote, F.; Zhang, X. D.; Zhang, H.; Wang, R. X.; Lei, Y.; Pan, B. C.; Xie, Y., Controllable disorder engineering in oxygen-incorporated MoS_2 ultrathin nanosheets for efficient hydrogen evolution. *Journal of the American Chemical Society* **2013,** *135* (47), 17881-17888.
92. Huang, H. L.; Chen, L. Q.; Liu, C. H.; Liu, X. S.; Fang, S. X.; Liu, W. P.; Liu, Y. J., Hierarchically nanostructured MoS_2 with rich in-plane edges as a high-performance electrocatalyst for the hydrogen evolution reaction. *Journal of Materials Chemistry A* **2016,** *4* (38), 14577-14585.
93. Xie, J. F.; Zhang, J. J.; Li, S.; Grote, F.; Zhang, X. D.; Zhang, H.; Wang, R. X.; Lei, Y.; Pan, B. C.; Xie, Y., Controllable disorder engineering in oxygen-incorporated MoS_2 ultrathin nanosheets for efficient hydrogen evolution. *Journal of the American Chemical Society* **2014,** *136* (4), 1680-1680.
94. Lukowski, M. A.; Daniel, A. S.; Meng, F.; Forticaux, A.; Li, L. S.; Jin, S., Enhanced hydrogen evolution catalysis from chemically exfoliated metallic MoS_2 nanosheets. *Journal of the American Chemical Society* **2013,** *135* (28), 10274-10277.
95. Li, S.; Ge, Z. H.; Zhang, B. P.; Yao, Y.; Wang, H. C.; Yang, J.; Li, Y.; Gao, C.; Lin, Y. H., Mechanochemically synthesized sub-5 nm sized CuS quantum dots with high visible-light-driven photocatalytic activity. *Appl Surf Sci* **2016,** *384*, 272-278.
96. Lee, C.; Yan, H.; Brus, L. E.; Heinz, T. F.; Hone, J.; Ryu, S., Anomalous lattice vibrations of single- and few-layer MoS_2. *Acs Nano* **2010,** *4* (5), 2695-2700.
97. Li, H.; Xie, F.; Li, W.; Fahlman, B. D.; Chen, M. F.; Li, W. J., Preparation and adsorption capacity of porous MoS_2 nanosheets. *Rsc Advances* **2016,** *6* (107), 105222-105230.
98. Kibsgaard, J.; Chen, Z. B.; Reinecke, B. N.; Jaramillo, T. F., Engineering the surface structure of MoS_2 to preferentially expose active edge sites for electrocatalysis. *Nat Mater* **2012,** *11* (11), 963-969.
99. Vrubel, H.; Hu, X. L., Growth and activation of an amorphous molybdenum sulfide hydrogen evolving catalyst. *Acs Catalysis* **2013,** *3* (9), 2002-2011.
100. Ludwig, J.; An, L.; Pattengale, B.; Kong, Q. Y.; Zhang, X. Y.; Xi, P. X.; Huang, J. E., Ultrafast hole trapping and relaxation dynamics in p-type CuS nanodisks. *J Phys Chem Lett* **2015,** *6* (14), 2671-2675.
101. Silvester, E. J.; Grieser, F.; Sexton, B. A.; Healy, T. W., Spectroscopic studies on copper sulfide sols. *Langmuir* **1991,** *7* (12), 2917-2922.

102. Saldanha, P. L.; Brescia, R.; Prato, M.; Li, H. B.; Povia, M.; Manna, L.; Lesnyak, V., Generalized one-pot synthesis of copper sulfide, selenide-sulfide, and telluride-sulfide nanoparticles. *Chem Mater* **2014,** *26* (3), 1442-1449.
103. Moulder, J. F.; Stickle, W. F.; 'Sobol, P. E.; Bomben, K. D., *Handbook of X-ray photoelectron spectroscopy*. Perkin-Elmer Corporation: USA, 1992.
104. Krylova, V.; Andrulevicius, M., Optical, XPS and XRD studies of semiconducting copper sulfide layers on a polyamide film. *Int J Photoenergy* **2009**.
105. Lam, K. F.; Yeung, K. L.; McKay, G., A rational approach in the design of selective mesoporous adsorbents. *Langmuir* **2006,** *22* (23), 9632-9641.
106. Smith, R. C.; Reed, V. D.; Hill, W. E., Oxidation of thiols by copper(II). *Phosphorus Sulfur* **1994,** *90* (1-4), 147-154.
107. Gao, J.; Li, B. C.; Tan, J. W.; Chow, P.; Lu, T. M.; Koratkar, N., Aging of transition metal dichalcogenide monolayers. *Acs Nano* **2016,** *10* (2), 2628-2635.
108. Aghagoli, M. J.; Beyki, M. H.; Shemirani, F., Application of dahlia-like molybdenum disulfide nanosheets for solid phase extraction of Co(II) in vegetable and water samples. *Food Chemistry* **2017,** *223*, 8-15.
109. Wu, F. C.; Tseng, R. L.; Juang, R. S., Characteristics of Elovich equation used for the analysis of adsorption kinetics in dye-chitosan systems. *Chem Eng J* **2009,** *150* (2-3), 366-373.
110. Cheung, C. W.; Porter, J. F.; McKay, G., Sorption kinetic analysis for the removal of cadmium ions from effluents using bone char. *Water Res* **2001,** *35* (3), 605-612.
111. Rengaraj, S.; Yeon, J. W.; Kim, Y.; Jung, Y.; Ha, Y. K.; Kim, W. H., Adsorption characteristics of Cu(II) onto ion exchange resins 252H and 1500H: Kinetics, isotherms and error analysis. *Journal of Hazardous Materials* **2007,** *143* (1-2), 469-477.
112. Demirbas, A.; Pehlivan, E.; Gode, F.; Altun, T.; Arslan, G., Adsorption of Cu(II), Zn(II), Ni(II), Pb(II), and Cd(II) from aqueous solution on amberlite IR-120 synthetic resin. *Journal of Colloid and Interface Science* **2005,** *282* (1), 20-25.
113. Chen, J. P.; Hong, L. A.; Wu, S. N.; Wang, L., Elucidation of interactions between metal ions and Ca alginate-based ion-exchange resin by spectroscopic analysis and modeling simulation. *Langmuir* **2002,** *18* (24), 9413-9421.
114. Chiron, N.; Guilet, R.; Deydier, E., Adsorption of Cu(II) and Pb(II) onto a grafted silica: isotherms and kinetic models. *Water Res* **2003,** *37* (13), 3079-3086.
115. Ngah, W. S. W.; Fatinathan, S., Adsorption characterization of Pb(II) and Cu(II) ions onto chitosan-tripolyphosphate beads: Kinetic, equilibrium and thermodynamic studies. *J Environ Manage* **2010,** *91* (4), 958-969.
116. Zhou, L. M.; Wang, Y. P.; Liu, Z. R.; Huang, Q. W., Characteristics of equilibrium, kinetics studies for adsorption of Hg(II), Cu(II), and Ni(II) ions by thiourea-modified magnetic chitosan microspheres. *Journal of Hazardous Materials* **2009,** *161* (2-3), 995-1002.
117. Gupta, V. K.; Agarwal, S.; Bharti, A. K.; Sadegh, H., Adsorption mechanism of functionalized multi-walled carbon nanotubes for advanced Cu (II) removal. *Journal of Molecular Liquids* **2017,** *230*, 667-673.
118. Zhang, X. Y.; Huang, Q.; Liu, M. Y.; Tian, J. W.; Zeng, G. J.; Li, Z.; Wang, K.; Zhang, Q. S.; Wan, Q.; Deng, F. J.; Wei, Y., Preparation of amine functionalized carbon nanotubes via a bioinspired strategy and their application in Cu^{2+} removal. *Appl Surf Sci* **2015,** *343*, 19-27.

119. Kadirvelu, K.; Faur-Brasquet, C.; Le Cloirec, P., Removal of Cu(II), Pb(II), and Ni(II) by adsorption onto activated carbon cloths. *Langmuir* **2000,** *16* (22), 8404-8409.
120. T.E. Payne; V. Brendler; M. Ochs; B. Baeyens; P.L. Brown; J.A. Davis; C. Ekberg; D.A. Kulik; J. Lutzenkirchen; T. Missana; Y. Tachi; L.R. Van Loon; S. Altmann, Guidelines for thermodynamic sorption modelling in the context of radioactive waste disposal. *Environmental Modelling & Software* **2013,** *42*, 143-156.
121. Villaescusa, I.; Fiol, N.; Martinez, M.; Miralles, N.; Poch, J.; Serarols, J., Removal of copper and nickel ions from aqueous solutions by grape stalks wastes. *Water Res* **2004,** *38* (4), 992-1002.
122. Ramette, R. W., Copper(II) complexes with chloride-ion. *Inorg Chem* **1986,** *25* (14), 2481-2482.
123. Kibsgaard, J.; Jaramillo, T. F.; Besenbacher, F., Building an appropriate active-site motif into a hydrogen-evolution catalyst with thiomolybdate $[Mo_3S_{13}]^{2-}$ clusters. *Nature Chemistry* **2014,** *6* (3), 248-253.
124. Tran, P. D.; Tran, T. V.; Orio, M.; Torelli, S.; Truong, Q. D.; Nayuki, K.; Sasaki, Y.; Chiam, S. Y.; Yi, R.; Honma, I.; Barber, J.; Artero, V., Coordination polymer structure and revisited hydrogen evolution catalytic mechanism for amorphous molybdenum sulfide. *Nat Mater* **2016,** *15* (6), 640-+.
125. Matyjaszewski, K., Advanced materials by atom transfer radical polymerization. *Adcanced Materials* **2018,** *30*, 1706441.